博士論文

Electronic Structure and Dynamics of Molecules on Oxide Surfaces

（酸化物表面における分子の電子構造とダイナミクス）

武安 光太郎

With a heartful gratitude for my wife, Shoko and my son, Kantaro

Abstract

Molecules (atoms) meet solids at their surfaces and interact with each other. The interaction mixes the electronic states of molecules as isolated systems and solids as condensed systems, which leads to adsorption of molecules on surfaces.

Metal oxides have characteristic electronic properties such as wide band gaps and electron correlation. On oxides, point defects such as oxygen vacancies are important structures, which affect the surface electronic structures and promote the interaction with molecules. Molecular adsorption, furthermore, significantly affects the surface electronic structure. Therefore, studies on adsorbed states of molecules are important on defective surfaces as well as on stoichiometric surfaces.

Metal oxide surfaces often reveal imhomogeneity. The power-law relation observed in the pressure decay in a vacuum chamber has been attributed to distribution of the adsorption energy of molecules on complex oxide surfaces, which remains to be solved.

In this dissertation, we firstly focus on the electronic structure of $SrTiO_3$(001) surfaces, and their interaction with hydrogen. Hydrogen has an amphoteric character and is expected to reveal either positively and negatively charged state.

On $SrTiO_3$, oxygen vacancies are readily formed. We have studied the effects of electron irradiation and subsequent oxygen adsorption on the electronic and atomic structure of the $SrTiO_3$(001) surface with ultraviolet photoemission spectroscopy (UPS) and low energy electron diffraction (LEED). While electron irradiation induces an in-gap state due to electron stimulated desorption of oxygen on the topmost surface, the vacancy-free surface is restored by molecular oxygen dosage. Electron irradiation also induces downward band bending, which seems to result in the formation of a conductive layer in the surface. This allows us to control the area density of the oxygen vacancies at the surface, thereby enabling us to switch the surface between semiconducting and metallic regimes.

On the $SrTiO_3$(001) surface, we have studied the hydrogen-adsorption effects on the surface electronic structure. On a nearly-vacancy-free (NVF) $SrTiO_3$(001) surface, atomic-hydrogen exposure induced in-gap states at 1.3 eV below the Fermi level, which is observed by UPS. The hydrogen coverage was quantitatively evaluated to be $3.1 \pm 0.8 \times 10^{14}$ cm^{-2} with H-specific ^{1}H(^{15}N,$\alpha\gamma$)^{12}C nuclear reaction analysis (NRA). Upon molecular hydrogen exposure to an oxygen-deficient (OD) $SrTiO_3$(001) having in-gap states due to oxygen vacancies, on the other hand, the in-gap state intensity was reduced with a hydrogen coverage of $0.9 \pm 0.7 \times 10^{14}$ cm^{-2}. We argue that H is positively charged on the NVF surface by being coordinated to the O atom, whereas H is negatively charged on the OD surface by occupying the oxygen vacancy site.

In addition, we have studied the rotational-state transition in the scattering of molecular hydrogen on the $SrTiO_3$(001) surfaces without and with oxygen vacancies. Molecular hydrogen exists in two nuclear-spin isomers, ortho-H_2 ($I = 1$) and para-H_2 ($I = 0$), and the transition between ortho-H_2 and para-H_2 is sensitive to the surface spin density. For the scattering exper-

iments, we have constructed a molecular-hydrogen beam with a flux of 3×10^{15} $cm^{-2}s^{-1}$. The H_2 beam was incident to $SrTiO_3(001)$ with and without oxygen vacancies, and scattered H_2 was state-selectively detected by (2 + 1) REMPI via E,F $^1\Sigma_g^+$. The probability of the ortho-para conversion in the scattering process were estimated to be 0.15 ± 0.05 and 0.28 ± 0.05 for the surface without and with oxygen vacancies, respectively. The magnetic properties on the surface with oxygen vacancies are discussed on the basis of the change in the rotational distribution.

Next, in order to analyze the adsorption energy of molecules on inhomogeneous oxide surfaces, we derived an analytical formula that directly transforms the pressure change into the distribution of adsorption energy (the adsorption density of states: ADOS). This method shows that the power-law behavior is equivalent to the situation in which the chamber surface has a constant-or exponential-type adsorption density of states for particles under a quasi-static condition.

On the basis of this formula, we analyzed the pumping-down curves reported in literatures to obtain ADOS of water molecules. The ADOS was dependent on the initial exposure pressure of water. The origin of the pressure dependence is discussed.

In order to further discuss the ADOS, temperature dependence of hydrogen depth distribution in a stainless steel surface was investigated by NRA. The activation energy for desorption of hydrogen was analyzed from the temperature dependence of NRA profiles. The activation energy was found to be distributed from 0.8 eV to 2.4 eV, which is consistent with the form of ADOS analyzed from the pressure decay curves.

Acknowledgment

I would like to show my gratitude to my advisor, Prof. Katsuyuki Fukutani. I have much to be thankful for him, which are daily advises on research contents and techniques, discussions, and doing all-night experiments and playing soccer together. He is a parent of me as a researcher and I am proud of doing research with him.

I really appreciate Prof. Masuaki Matsumoto, who had been a staff in our research group. I first joined Fukutani loboratory taking a class to participate in a laboratory and have an experience with a research eight year ago. He taught me how to shut franges, take LEED patterns, and analyze them. This experience was a trigger for me to have an interest on experimental physics. I am also grateful for his advices and supports to date.

I would like to express my appreciation to Dr. Shohei Ogura. Many research techniques used in the present study such as how to design and develop instruments, sample preparations, and computational calculations were taught by him first. In addition, his advices and comments based on acute visions have improved my researches and me. The other important thing that he gave me is a better basketball shooting form.

I am also deeply grateful to the staff in and around Fukutani group for overall supports. Prof. Wilde Markus and Mr. Taizo Kawauchi gave me fundamental skills for experiments as well as fruitful comments from different perspectives. I have been encouraged by Emeritus Prof. Yoshitada Murata's word, "That's interesting." in research seminars. I have also learned not only experimental now-how but also the importance of finding and studying interesting phenomena from him. I have been impressed by Prof. Tatsuo Okano's ideas on researches such as the electron interference in field electron emission and making a mirror-scattering surface for catching a tail of Maxwell's demon. It goes without saying that comments by Emeritus Prof. Yuh Fukai, Emeritus Prof. Akira Kinbara, and Prof. Takaaki Kawamura who are specialists of hydrogen in metals, thin films, and electron scattering, gave me wider perspectives. Hearing about their experiences in Ohio, Grenoble, and England also encouraged me to do researches in foreign countries. And, without Ms. Tomoka Nakamura's supports on managements of research funds and parties, I would not have finished my PhD course.

My research was directly supported by former members in our laboratory. Discussions with Dr. Toshiki Sugimoto let me started to consider the relation between evacuation curves and adsorbed states of molecules. Encouragements by and continuous discussions with him formed Sects 4.1 and 4.2 in this dissertation. Mr. Keisuke Fukada taught me good tips on using UPS. Discussions with him also cultivated contents in Sect. 3.2.

Let me thank to Mr. Satoshi Harashima at Hwang laboratory, which was in Univ. Tokyo and now is in Stanford Univ. When I started electron stimulated desorption on $SrTiO_3$, his advices and experiences on surface-conductivity measurements on Ar-sputtered $KTaO_3$ gave me a guideline of the work. Again, I cannot forget to thank him not just as a researcher, but also as a wonderful friend. I am also deeply grateful to Prof. Harold Y. Hwang, Dr. Yasuyuki Hikita, Dr. Chris Bell, Ms. Makiko Tanaka, Dr. Yusuke Kozuka, Dr. Takeaki Yajima, Dr. Takuya

Higuchi, Dr. Minu Kim, and the other current and former members in Hwang laboratory for comments on my researches and continuous interactions as well as coaching and advises when I was a bachelor student.

Thank you to the staff in the trial-production factory in Inst. Industrial Sci., Univ. Tokyo and Kyowa Shinku company. Owing to them, I could have developed instruments.

I thank the other former and current members in and around Fukutani group, with whom I have shared precious time for research activities, playing soccer, and the five-times winning in long-distance relay races. In particular, I have spent four and five years in the laboratory with Dr. Akihiko Ikeda and Mr. Satoshi Oono, respectively. I believe that long-time chatting and discussions with Dr. Ikeda did not disturb but promoted researches. And, as a matter of fact, Satoshi Oono was also my class mate in our high school. I have been stimulated by him for more than ten years totally. He is another Satoshi with whom I would like to keep the connection for my entire life.

I am grateful to the examination committee, Prof. Shinji Tsuneyuki, Prof. Yukio Hasegawa, Prof. Iwao Matsuda, and Prof. Kyoko Ishizaka for their constructive comments during the defenses. The productive defenses let me reaffirm the fascination to join the scientific community.

I have to say thank you to Mr. Naoki Saga, Ms. Kumiko Saito, Ms. Haruko Yamada, and the other staff in the office of Department of Applied Physics and Inst. Industrial Sci., Univ. of Tokyo. Their kindness has leaded me to the current stage.

Personally, the practice of track and field refreshed me and gave me a driving force to do researches. In addition, several ideas used in my researches happened when I was running or jumping. Thank you, Mr. Yasuyuki Fujita and the other members at the track and field club in Univ. of Tokyo.

I would like to thank my family and friends. In particular, for example, making a miniature gondola, a motor car, and a robot made of paper boxes with my mother Yukiko, my father Hiromitsu, and my grandmother Noriko, respectively, was a starting point for me to do researches. My grandfather, Yutaka Tuzi took me to hardware stores more than twenty years ago. Though, at that time, I never imagined that I would talk about researches with him and refer his works. And, without supports by my parents-in-law, Kazunari and Keiko Akimoto, my sister- and brother-in-law, Yoko and Kimitoshi Higashino, I would not also finish this dissertation. Finally, Shoko and Kantaro, you are like axioms for me.

Contents

Chapter 1

Introduction

1.1 Interaction of molecules with solid surfaces

Solid surfaces are fields where molecules (atoms) as isolated systems and solids as condensed system interact with each other. In isolated molecules, electronic and vibrational states are localized with discrete energy levels. Energy and angular momentum are conserved in the molecules. On the other hand, the electronic and vibrational states of condensed matter are spatially extended forming continuous energy bands. When a molecule approaches a solid, their states interact with each other through electromagnetic interactions and exchange the energy and angular momentum.

The interaction is firstly seen in the change in the electronic structure in a molecule. Figure 1.1 (a) shows a schematic of the electronic structure of a molecule with an unpaired electron in the vicinity of a surface. When the molecule is enough far from the surface, the discrete energy level of the unoccupied state is at U above that of the occupied state. U corresponds to the repulsion energy between the electron in the occupied state and an additional electron which fill the occupied state. As the surface-molecule distance decreases, the energy difference between the occupied state and the unoccupied state U_{eff} is reduced by an image charge on the surface and the transfer integral t between the surface and the molecule. The energy levels of the molecule is also broadened by t. As the broadening overcomes U_{eff}, the electronic structure of the molecule mixes with and finally accords with that of the surface depolarizing the spin in the molecule.

The change in the electronic structure also shifts the energy of the molecule and the surface. One calculates the each total electronic energy fixing the position of the nuclei at a certain point in the range of the Born-Oppenheimer approximation. Figure 1.1 (b) shows the energy curve as a function of the surface-molecule distance, which is called an adiabatic potential curve. When the molecule is enough far from the surface, the gas state is the eigenstate. The adsorbed state of the molecule, on the other hand, is the eigenstate in the near distance from the surface. In the adsorbed state, molecular electronic states mix with electronic states of the solids, which lowers the total energy. The energy gain is the adsorption energy. The adsorption energy depends on the local electronic structure of the adsorption site. Therefore, the adsorption energy is strongly influenced by the local atomic structure, which governs the local electronic structure.

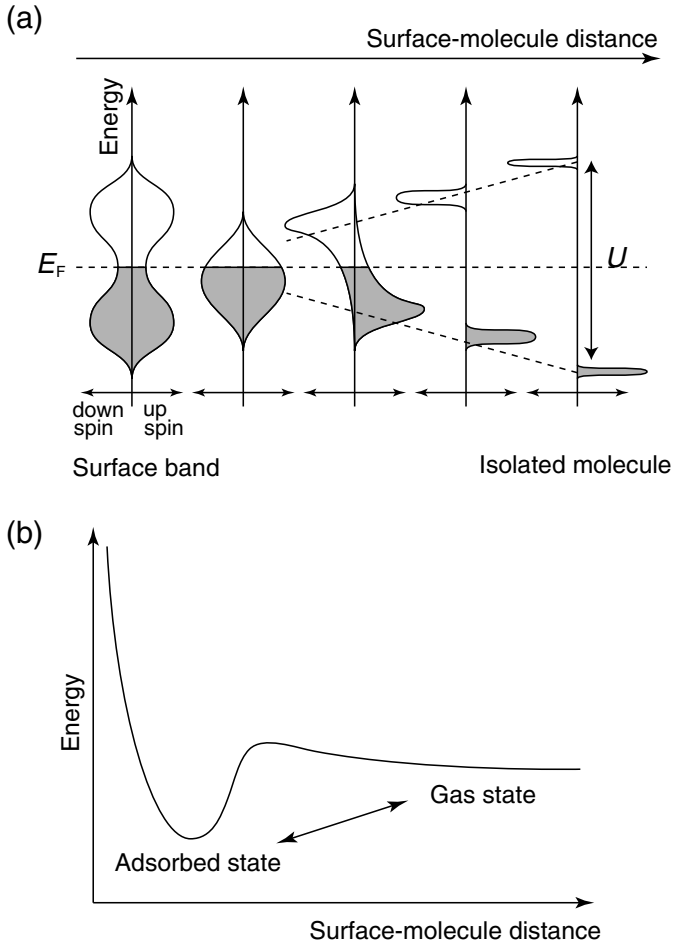

Figure 1.1: (a) A schematic of the electronic structure of a molecule with an unpaired electron in the vicinity of a surface. E_F and U denote the Fermi level and the difference of the energy between the highest occupied state and the lowest unoccupied state of the molecule in an isolated state. (b) A schematic of an adiabatic potential curve for adsorption and desorption of molecules.

1.2 Dynamics of molecules at surfaces

Adsorption is the transition, in which the molecule approaches the surface and falls in the adsorbed state. As shown in Fig. 1.1 (a), the initial state is a continuum state in gas phase, and the final state us a bound state in the adsorption well. Desorption is the reverse process of the adsorption.

Such transitions are accompanied by the exchange of phonon, electrons, and spins between molecules and surfaces. Examples of transitions caused by the molecule-surface interaction are described in the following.

The energy transfer effectively occurs in adsorption. Adsorption of molecules is an exother-

mic process, in which the adsorption energy has to be dissipated. In the case of chemisorption[1] on metals, the adsorption energy is about $0.5 \sim 3$ eV [1, 2, 3, 4]. The adsorption is dissipated as the excitation of electron-hole pairs in metal surfaces [5, 6, 7]. Chemisorption of electronegative molecules on surfaces with low workfunctions such as alkali metals transfers electrons in a surface to the affinity level of the molecules. Deexcitation of the transferred electrons emits light or the Auger process emits electrons [8]. On the other hand, a physisorption[2] process on a metal dissipates the adsorption energy into the substrate phonons [9, 10, 11]. Transitions involving the modification of chemical bonds of molecules also require energy transfer between the molecules and surfaces. For example, the reaction of $H + H \rightarrow H_2$ releases the energy of 4.5 eV [12]. The transition rarely occurs in two-body collision of hydrogen atoms, because the energy cannot be dissipated by radiation [13, 14]. On the other hand, the transition is effectively induced on solid surfaces [15, 16]. Although the detailed mechanism is yet to be elucidated, the released energy in the transition is also considered to be transferred into electron or lattice systems in solids.

Other important processes are the transitions triggered by electronic transitions. When a metal is irradiated with light or electrons, electrons around the Fermi level are excited. The excited electrons move into unoccupied levels of adsorbed molecules. Deexcitation of the electrons involves vibrational excitation or desorption of the molecules [17, 18, 19, 20, 21, 22]. The irradiation of electrons of tens of eV on metal oxides desorbs light molecules such as oxygen and hydrogen atoms via an interatomic Auger process [23, 24]. Photocatalyzed reaction is also a transition induced by electronic transitions in solids. When a matter with a band gap of a few eV such as oxides is irradiated with light with the energy of longer than the band gap, electrons and holes are excited to the conduction band and the valence band, respectively [25]. The excited electrons (holes) diffuse into adsorbed molecules with positive (negative) charges [26] and the neutralized molecules desorb as products [27].

The moelcule-surface interaction also exchanges the spins as realized in the nuclear spin conversion of physisorbed hydrogen molecules. Molecular hydrogen exists in two nuclear-spin isomers, ortho-hydrogen and para-hydrogen. Due to the symmetry of the total wave function with respect to the permutation of the two nuclei, ortho-hydrogen having the total nuclear spin $I = 1$ is in the rotational state with odd rotational quantum number J, while para-hydrogen of $I = 0$ has even J. The conversion between the ortho and para states is so slow in the gas phase with a conversion time of the order of $\sim 10^{20}$ s [28]. On the other hand, the ortho-para conversion can be promoted on surfaces. The main mechanisms of the promotion within the first-order perturbation are the interaction of the nuclear spin with the magnetic moment on a surface, spins of electrons distributed around the nuclear (Fermi contact interaction), and the effective magnetic field induced by the motion of electrons [14]. Theoretical works suggest the ortho-para conversion is promoted also by the second-order perturbation [29, 30, 31, 32, 33, 34]. In the second-order perturbation, coulomb interactions mix the ground state of molecular hydrogen

[1] Adsorption of molecules with making chemical bonds.
[2] Adsorption of molecules with a van der Waals force.

$X^1\Sigma_g^+$, electrons in the surface, and an excited state of molecular hydrogen $b^3\Sigma_u^+$. The $b^3\Sigma_u^+$ state is deexcited to the $X^1\Sigma_g^+$ state by the Fermi contact interaction, which induces the ortho-para conversion as in the case of the first-order perturbation. Experiments have confirmed that the second-order perturbation is the dominant factor in the conversion on Cu and Ag surfaces [35, 36].

1.3 Approach to understanding molecule-surface interaction

To understand the molecule-surface interaction, the first step is characterization of the initial and the final states, which include configurations of nuclei and electronic structures on bare surfaces and molecule-adsorbed surfaces. Detecting internal states and the translational energy of desorbed and scattered molecules also notices the final states.

1.4 Interaction of molecules with oxide surfaces

Metal oxides have particular characters such as wide band gaps of more than 3 eV and strong electron correlation. Owing to the wide band gap, interesting photocatalytic reactions are realized [37, 27], which are the specific transitions on oxide surfaces. The desorption of molecules via an interatomic Auger process is also a phenomenon observed on oxide surfaces. In addition, the lifetime of excited electrons and holes depends on the band gap [38]. Therefore, the mechanism of chemisorption, and vibrational excitation and desorption of molecules by light irradiation, which include excitation of electrons in surfaces, might be different from that on other materials.

1.4.1 Atomic structures of oxide surfaces

Two main characteristics of atomic structures of oxide surfaces are the variety of surface reconstructions and the existence of point defects [39].

Surface reconstructions are associated with changes in the stoichiometry of surfaces. The variation of the stoichiometry is because of near-degenerate energies for various structures. The structures are accordingly changed by the balance of the chemical potentials of atoms such as oxygen in oxides and gas phase. This balance is determined by the temperature and the pressure of the gas molecules. When the chemical potential goes beyond the chemical potential of oxygen in the gas phase, the oxygen atoms desorbs to the gas phase. The decrease of oxygen atoms in the oxide brings about surface reconstructions. A typical example is seen on an $Al_2O_3(0001)$ surface. The surface shows the (1×1) structure under 1000 °C [40]. Annealing the surface in vacuum at 1200, 1300, and 1400 °C reconstructs the surface into (2×2), $(3\sqrt{3}\times3\sqrt{3})$−R30°, and $(\sqrt{31}\times\sqrt{31})$−R±9°, respectively [41]. In the reconstructed surfaces, the ratio of oxygen atoms is lower than that in the (1×1) surface.

On the other hand, point defects are quasi-stable structures usually produced in non-equilibrium conditions such as the irradiation of ions and molecules. Point defects on oxide surfaces include oxygen vacancies, adatoms, cation vacancies, and interstitial atoms. Adatoms are essentially same as the adsorbed molecules, which will be explained below. Among the defects, oxygen vacancies are important structures observed in various kinds of oxides [39, 42, 43, 44]. This is because oxygen vacancies not only influence the electronic properties [45, 46, 47] but also promote interactions with molecules [48, 49, 50]. Oxygen vacancies dope $0 \sim 2$ electrons depending on matter and the position of the Fermi level [51, 52, 53]. In the case of $SrTiO_3$, an oxygen vacancy supply two electrons [54]. Oxygen vacancies are often produced by ion sputtering, which changes the surface composition [55] and makes the surface disordered [56, 57]. Therefore, the atomic structure of oxygen vacancies had remained to be elucidated [58]. Recently, the structure of oxygen vacancies on TiO_2 induced by electron stimulated desorption has been reported [59]. The oxygen vacancies form rows by the selective desorption of oxygen atoms [59].

1.4.2 Molecular adsorption on oxides

As metal oxides are widely used in gas sensors, the electronic structures are strongly affected by the adsorption of molecules [60, 61, 62, 63, 64, 65, 66, 67]. In particular, the influence of the adsorption of hydrogen is large as well as oxygen compared with other molecules. This is because the large adsorption energy of a few eV [4], which means the mixing of electronic structures in hydrogen and surfaces is large.

When atomic hydrogen adsorbs on ZnO surfaces with the stoichiometric composition at room temperature, hydrogen donates electrons on the surfaces. The amount of the donation depends on Miller index as $(10\bar{1}0)$>$(000\bar{1})$>(0001). The former two surfaces are metalized by the hydrogen and show metallic bands [68]. On the $(10\bar{1}0)$ surface, excess hydrogen adsorbs at 200 K. The hydrogen receives electrons and removes the surface metallicity [69]. The adsorption of atomic hydrogen on oxygen atoms on an n-type semoconducting $SrTiO_3$(001) surface similarly dopes electrons and metalize the surface [70, 71, 72]. The adsorption also increases an electronic state in the band gap. The state spread throughout the band gap and the center is about 1.2 eV below the Fermi level.

On the other hand, the adsorption of hydrogen on oxygen vacancy sites are reported on MgO surfaces [73, 74]. An interesting point in the case is that the adsorbed hydrogen exists as the hydride anion [73, 74, 75]. The presence of the hydride anion on an oxygen vacancy on the other oxide has not been reported, though it has been reported in bulk oxides such as $12CaO{\cdot}7Al_2O_3$,[76], $BaTiO_3$ [77, 78], ZnO [75, 79], and TiO_2 [80].

In order to discuss the molecule-surface interaction on oxide surfaces, the knowledge of molecular-adsorbed states on defective surfaces as well as on stoichiometric surfaces are necessary. There are much fewer works for molecular-adsorbed states on oxide surfaces than on metal surfaces [39, 81]. Furthermore, the interaction of defective surfaces, whose structure is

specified, with molecules has just started to be studied in the present date [82, 83].

1.5 Effects of inhomogeneity on oxide surfaces

Molecular-adsorbed states on inhomogeneous oxide surfaces have been suggested not to be understood by the sum of the states on single crystal surfaces. One suggestion is the pressure change in an evacuation process of a vacuum chamber made of stainless steel, whose surface is covered by the complex of oxides.

If the desorption of molecules is assumed to be negligible, the time change in pressure P by evacuation is given by

$$\frac{dP}{dt} = -PS, \tag{1.1}$$

where S is the evacuation speed of a pump. The solution of Eq. (1.1) is

$$P = P_0 \exp(-S\,t), \tag{1.2}$$

where P_0 is the pressure decided by the initial condition. Equation (1.2) insists that the pressure exponentially decreases as a function of time. In the next step, one type of molecules are assumed to desorb from the wall of the vacuum chamber covered by an oxide single srystal. We let the surface sojourn time of the molecules τ, which is defined by

$$\tau = \tau_0 \exp(E_\mathrm{d}/k_\mathrm{B}T). \tag{1.3}$$

τ_0 and E_d denote a constant and the activation energy of desorption, respectively. When τ is enough longer than the flying time of the molecules from a wall to the other wall, the pressure change is given by

$$P \propto \exp\left(-\frac{t}{\tau(1 + c(s^{-1} - 1))}\right), \tag{1.4}$$

where c is the sticking coefficient of the molecule, s is a constant proportional to the evacuation speed of the pump [84]. Equation (1.4) means that the decrease of the pressure forms a exponential characterized by τ, c, and s. In the case that the surface is a α-Cr_2O_3(0001) surface, τ_0, E_d, and τ are 1.4×10^{-13} s, 0.92 eV, and 3.9×10^{2} s, respectively [85]. If we increase the number of kinds of single crystal surfaces, the pressure change is approximately presented as the sum of exponentials in the right-hand side of Eq. (1.4). The candidates of the surface includes a FeO(111) surface, where τ_0, E_d, and τ for the monomer of a water molecule are 3.0×10^{-15} s, 0.54 eV, and 1.0×10^{-7} s, respectively [86].

However, the pressure change in a evacuation process shows a power-law decay in real systems [87]. The inconsistency suggests that the molecular behaviors on inhomogeneous oxide surfaces are not reduced to the behaviors on single crystal surfaces.

Power-law statistics is frequently found in various phenomena such as excited-electron decays [88, 89, 90], charge decays in capacitors [91], protein structures [92], dewetting silicone

layers [93] and momentum distribution functions in the Tomonaga-Luttinger liquid [94]. The power-law behavior is known to reflect the intrinsic interaction of the system. In the case of the evacuation process, the power-law has been discussed to originate from the distribution of the adsorption energy of molecules [95, 96], as explained in Sect. 4.1. Despite much effort, however, a method to specify the distribution of the adsorption energy from measured pressure changes is yet to be constructed.

1.6 Purpose of the present study

Based on the above backgrounds, the present study treats $SrTiO_3$(001) surfaces and inhomogeneous oxide surfaces.

We have induced surface oxygen vacancies by using electron stimulated desorption and studied the effect of the oxygen vacancies on the electronic structure (Sect. 3.1). On the oxygen-vacancy-controlled surface, the change in the surface electronic structure by adsorption of hydrogen and the charged states of the hydrogen has been studied (Sect. 3.2). We also have developed an atomic and molecular hydrogen beam source and a state-selective measurement system for scattered hydrogen (Sect. 2.2). With the apparatus, we have measured the rotational and the nuclear spin state of molecular hydrogen scattered from the $SrTiO_3$(001) surfaces with and without oxygen vacancies. The magnetic properties on the surface with oxygen vacancies are discussed on the basis of the change in the rotational distribution (Sect. 3.3).

Focusing on inhomogeneous oxide surfaces, we have deduced an analytical formula for calculating the distribution of the adsorption energy on chamber surfaces from measured pressure change (Sect. 4.1). The distribution of the adsorption energy of water adsorbed on the surface of a stainless steel chamber was analyzed with the formula (Sect. 4.2). In order to confirm the analyzed distribution of the adsorption energy, thermal stability of hydrogen atoms has been measured (Sect. 4.3).

Chapter 2

Experimental

2.1 Principle

2.1.1 Low energy electron diffraction

Low-energy electron diffraction (LEED) measures electron diffraction from a solid surface. Analysis of the diffraction gives the information of the atomic structure of the surface. The wavelength λ (Å) of an electron with an energy of E (eV) is given by

$$\lambda = \sqrt{\frac{h^2}{2m_0 E}} = \sqrt{\frac{150.4}{E}}, \tag{2.1}$$

where h is Planck's constant and m_0 is the mass of an electron. In LEED measurements, an electron with energies of 50 ~ 300 eV irradiates a sample. The wavelength of the incident electron is ~1 Å following Eq. (2.1), which is similar to the interatomic spacing in solids. This causes the diffraction of the electron reflecting atomic arrangements. In addition, the low incident energy of an electron lets LEED be a surface sensitive measurement.

Surface sensitivity of LEED is firstly explained in the sense of the mean free path of electrons. Figure 2.1 shows the mean free path of electrons in solids as a function of the electron energy [97, 98]. The mean free path is relatively independent of materials. The curve is accordingly called the universal curve. The universal curve shows that the mean free path of electrons with energies of 50 ~ 300 eV is less than 10 Å. This means that the diffracted electron is emitted from only the region whose depth is less than 10 Å from the surface.

Electron diffraction is an elastic scattering of electrons by Coulomb potential in a matter. The wavefunction of incident electrons $\psi_{\text{in}}(\boldsymbol{r})$ satisfies the Schrödinger equation in a free space,

$$-\frac{\hbar^2}{2m}\nabla^2\psi_{\text{in}}(\boldsymbol{r}) = E\psi_{\text{in}}(\boldsymbol{r}). \tag{2.2}$$

The energy of incident electrons E is determined by the accelerated voltage of the electrons. One of the solution of Eq. (2.2) is a plane wave, which specifies the incident electrons, given by

$$\psi_{\text{in}}(\boldsymbol{r}) = \exp(i\boldsymbol{K_0}\cdot\boldsymbol{r}), \tag{2.3}$$

where $\boldsymbol{K}_0$ is the wave number of the wavefunction of the incident electrons. If we consider only

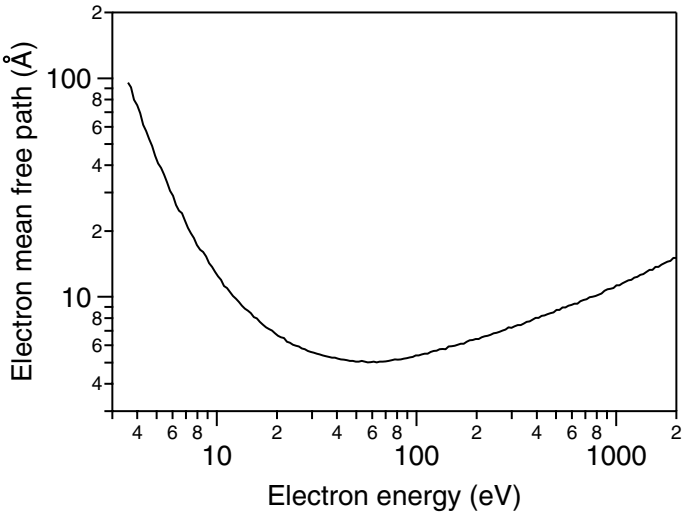

Figure 2.1: The universal curve of the electron mean free path as a function of the electron kinetic energy, as fit to experiment data for many metallic surfaces [97, 98].

the elastic scattering of the electrons in a matter, the potential in the matter is replaced with an electrostatic potential $V(\boldsymbol{r})$. The wavefunction of the electrons under $V(\boldsymbol{r})$ is given by

$$\left[-\frac{\hbar^2}{2m}\nabla^2 + eV(\boldsymbol{r})\right]\psi(\boldsymbol{r}) = E\psi(\boldsymbol{r}), \tag{2.4}$$

where $\psi(\boldsymbol{r})$ is the total wavefunction for the incident and scattered electrons. The solution of Eq. (2.4) is mathematically given by

$$\psi(\boldsymbol{r}) = \exp(i\boldsymbol{K_0}\cdot\boldsymbol{r}) + \frac{m_0 e}{2\pi\hbar^2}\int \frac{\exp(iK_0|\boldsymbol{r}-\boldsymbol{r'}|)}{|\boldsymbol{r}-\boldsymbol{r'}|}V(\boldsymbol{r'})\psi(\boldsymbol{r'})d\boldsymbol{r'}. \tag{2.5}$$

We consider Eq. (2.5) when $|\boldsymbol{r}| >> |\boldsymbol{r'}|$. In the condition, $K_0|\boldsymbol{r}-\boldsymbol{r'}| \sim K_0|\boldsymbol{r}| - \boldsymbol{K}_0\cdot\boldsymbol{r'}$. In the first order Born approximation, $\psi(\boldsymbol{r'})$ is replaced with $\psi_{\rm in}(\boldsymbol{r'})$. Then Eq. (2.5) is transformed into

$$\psi(\boldsymbol{r}) = \exp(i\boldsymbol{K_0}\cdot\boldsymbol{r}) + \frac{m_0 e}{2\pi\hbar^2}\frac{\exp(iKr)}{r}\int V(\boldsymbol{r'})\exp[-i(\boldsymbol{K}-\boldsymbol{K}_0)\cdot\boldsymbol{r'}]d\boldsymbol{r'}, \tag{2.6}$$

where $\boldsymbol{K}$ is the wave number of the scattered wave. The second term of the right-hand side of Eq. (2.6) means that the wavefunction of the scattered electrons $\psi_{\rm sc}(\boldsymbol{r})$ is rearranged as

$$\psi_{\rm sc}(\boldsymbol{r}) = \frac{1}{r}\exp(iKr)\Phi^{\rm e}(\boldsymbol{K}-\boldsymbol{K}_0), \tag{2.7}$$

$$\Phi^{\rm e}(\boldsymbol{K}-\boldsymbol{K}_0) \equiv \frac{m_0 e}{2\pi\hbar^2}\int V(\boldsymbol{r'})\exp[-i(\boldsymbol{K}-\boldsymbol{K}_0)\cdot\boldsymbol{r'}]d\boldsymbol{r'}. \tag{2.8}$$

In a crystal, $V(\boldsymbol{r'})$ in Eq. (2.8) is the sum of the contribution from atoms in the crystal. An electrostatic potential at $\boldsymbol{r'}$ produced by k th atom is defined as $V_k(\boldsymbol{r}$"), where $\boldsymbol{r''} = \boldsymbol{r'} - \boldsymbol{r}_k$ and

$\boldsymbol{r}_k$ is the position of the k th atom. $V(\boldsymbol{r}')$ is accordingly given by

$$V(\boldsymbol{r}') = \sum_k V_k(\boldsymbol{r}''). \tag{2.9}$$

Substituting Eq. (2.9) into Eq. (2.8) yields

$$\Phi^{\mathrm{e}}(\boldsymbol{K} - \boldsymbol{K}_0) = \sum_k f_k^{\mathrm{e}} \exp[-i(\boldsymbol{K} - \boldsymbol{K}_0) \cdot \boldsymbol{r}_k], \tag{2.10}$$

$$f_k^{\mathrm{e}} = \frac{m_0 e}{2\pi\hbar^2} \sum_k \left\{ \int V_k(\boldsymbol{r}'') \exp[-i(\boldsymbol{K} - \boldsymbol{K}_0) \cdot \boldsymbol{r}''] d\boldsymbol{r}'' \right\}, \tag{2.11}$$

where f_k^{e} is the atomic scattering factor for the k th atom. The position of the unit cell which includes the k th atom $\boldsymbol{R}_n$ is given by

$$\boldsymbol{R}_n = n_1 \boldsymbol{a}_1 + n_2 \boldsymbol{a}_2 + n_3 \boldsymbol{a}_3, \tag{2.12}$$

where n_i's are integers and $\boldsymbol{a}_i$'s are unit lattice vectors. The position of the k th atom in the unit cell is defined as $\boldsymbol{r}_j$. With $\boldsymbol{R}_n$ and $\boldsymbol{r}_j$, Eq. (2.10) is written as

$$\Phi^{\mathrm{e}}(\boldsymbol{K} - \boldsymbol{K}_0) = F(\boldsymbol{K} - \boldsymbol{K}_0) S(\boldsymbol{K} - \boldsymbol{K}_0), \tag{2.13}$$

$$F(\boldsymbol{K} - \boldsymbol{K}_0) = \sum_j f_j^{\mathrm{e}} \exp[-i(\boldsymbol{K} - \boldsymbol{K}_0) \cdot \boldsymbol{r}_j], \tag{2.14}$$

$$S(\boldsymbol{K} - \boldsymbol{K}_0) = \sum_n \exp[-i(\boldsymbol{K} - \boldsymbol{K}_0) \cdot \boldsymbol{R}_n], \tag{2.15}$$

where $F(\boldsymbol{K} - \boldsymbol{K}_0)$ is the crystal structural scattering factor. The intensity of diffracted electrons is given by

$$I \propto I_0 |F|^2 |S|^2, \tag{2.16}$$

where I_0 is the intensity of incident electrons. $|G|^2$ is written as Laue function,

$$|S|^2 = \frac{\sin^2[\pi N_1 (\boldsymbol{K} - \boldsymbol{K}_0) \cdot \boldsymbol{a}_1]}{\sin^2[\pi (\boldsymbol{K} - \boldsymbol{K}_0) \cdot \boldsymbol{a}_1]} \frac{\sin^2[\pi N_2 (\boldsymbol{K} - \boldsymbol{K}_0) \cdot \boldsymbol{a}_2]}{\sin^2[\pi (\boldsymbol{K} - \boldsymbol{K}_0) \cdot \boldsymbol{a}_2]} \frac{\sin^2[\pi N_3 (\boldsymbol{K} - \boldsymbol{K}_0) \cdot \boldsymbol{a}_3]}{\sin^2[\pi (\boldsymbol{K} - \boldsymbol{K}_0) \cdot \boldsymbol{a}_3]}, \tag{2.17}$$

where N_i denotes the number of atoms aligned in $\boldsymbol{a}_1$ direction in the crystal. In LEED, N_3 is generally at least smaller than 10 because incident electrons probe a few atomic layers from the surface. Equation (2.17) has therefore maxima when

$$(\boldsymbol{K} - \boldsymbol{K}_0) \cdot \boldsymbol{a}_i = h_i \quad (i = 1, 2), \tag{2.18}$$

where h_i's are integers. Equation (2.18) is satisfied only when $(\boldsymbol{K} - \boldsymbol{K}_0)$ accord with the two dimensional reciprocal lattice vector $\boldsymbol{G}$ parallel to the surface, which is given by

$$\boldsymbol{G} = l_1 \boldsymbol{g}_1 + l_2 \boldsymbol{g}_2, \tag{2.19}$$

where l_i's are integers and $\boldsymbol{g}_i$'s are unit reciprocal lattice vector defined as

$$\boldsymbol{g}_1 = 2\pi \frac{\boldsymbol{a}_2 \times \boldsymbol{n}}{\boldsymbol{a}_1 \cdot (\boldsymbol{a}_2 \times \boldsymbol{n})}, \tag{2.20}$$

$$\boldsymbol{g}_2 = 2\pi \frac{\boldsymbol{n} \times \boldsymbol{a}_1}{\boldsymbol{a}_1 \cdot (\boldsymbol{a}_2 \times \boldsymbol{n})}, \tag{2.21}$$

where $\boldsymbol{n}$ is the unit vector normal to and pointing out of the surface. Thus, diffracted patterns of LEED represent two dimensional reciprocal lattice patterns of a surface.

2.1.2 Photoemission spectroscopy

Photoemission spectroscopy (PES) is a method to investigate the electronic structure of matter. In a PES measurement, a matter is irradiated with light. Electrons in the matter firstly absorb the light and excited to an excited state. Then the excited electrons diffuse to the surface of the matter and are emitted out of the matter. The kinetic energy of the emitted photoelectrons E_{kin} is measured to know the original energy level of the emitted electron in matter.

PES includes X-ray photoemission spectroscopy (XPS) and ultraviolet photoemission spectroscopy (UPS), which use X-ray and ultraviolet as incident light, respectively. XPS is mainly used to measure the core level of electrons in matter and UPS is used to measure shallow levels, in particular, the valence band in the case of solids. In addition to this, synchrotron radiation is an effective light source, which varies the wavelength continuously.

PES is basically a surface sensitive measurement due to the short diffusive distance of excited electrons in matter, which is also described by the universal curve shown in Fig. 2.1 (a).

Photoionization probability dominantly depends on the excitation probability of electrons irradiated with light in matter. When an electron is in the radiation field, the Hamiltonian of the electron is given by

$$\begin{aligned} H &= H_0 + H', \\ H' &= -\frac{e}{2m}(\boldsymbol{A} \cdot \boldsymbol{P} + \boldsymbol{P} \cdot \boldsymbol{A}) - e\Phi + \frac{e^2}{2m}|A|^2, \end{aligned} \tag{2.22}$$

where H_0 is the original Hamiltonian of the electron, e is the elementary charge, m is the mass of the electron, $\boldsymbol{P}$ is the momentum operator, and $\boldsymbol{A}$ and Φ are the vector and the scalar potential of the incident light field, respectively. If multi-photon processes are negligible and the direct transition from an initial state i with the wavefunction ψ_i to a final state f with the wavefunction ψ_f is dominant, the transition probability per unit time $\mathrm{d}\omega/\mathrm{d}t$ is given by Fermi's golden rule:

$$\frac{d\omega}{dt} = \frac{2\pi}{\hbar} | < \psi_f | H' | \psi_i > |^2 \delta(E_f - E_i - \hbar\omega), \tag{2.23}$$

where ω is the frequency of the light and E_f and E_i are the energy eigenvalues of the final and initial states, respectively. Substituting Eq. (2.22) into Eq. (2.23) gives the differential

photoionization cross-section $\mathrm{d}\sigma/\mathrm{d}\Omega$, which is proportional to $\mathrm{d}\omega/\mathrm{d}t$,

$$\frac{d\sigma}{d\Omega} \propto |<\psi_f|\boldsymbol{A}\cdot\boldsymbol{P}+\boldsymbol{P}\cdot\boldsymbol{A}|\psi_i>|^2\delta(E_f-E_i-\hbar\omega). \tag{2.24}$$

In Eq. (2.24), a guage where $\Phi = 0$ is chosen and the small diamagnetic term $|A|^2$ derived from a two-photon process is ignored. The commutator $[\boldsymbol{P}, \boldsymbol{A}] = -i\hbar\nabla\cdot\boldsymbol{A}$ changes Eq. (2.24) into

$$\frac{d\sigma}{d\Omega} \propto |<\psi_f|2\boldsymbol{A}\cdot\boldsymbol{P}-i\hbar\nabla\cdot\boldsymbol{A}|\psi_i>|^2\delta(E_f-E_i-\hbar\omega). \tag{2.25}$$

The term $\nabla\cdot\boldsymbol{A}$ is negligible in a uniform medium, though it may not be small compared to $\boldsymbol{A}\cdot\boldsymbol{P}$ at a surface. Here, we assume that $\nabla\cdot\boldsymbol{A}$ is small and $\boldsymbol{A}$ is written as a plane wave in free space,

$$\boldsymbol{A}(r,t) = \boldsymbol{A}_0\exp(-i\omega t + i\boldsymbol{q}\cdot\boldsymbol{r}), \tag{2.26}$$

where $\boldsymbol{q}$ is the momentum of the light. $\boldsymbol{q}$ is negligible compared to $\boldsymbol{P}$ at a photon energy below ~10 keV and $\boldsymbol{A}$ is regarded as a constant $\boldsymbol{A}_0$. Then Eq. (2.25) becomes

$$\frac{d\sigma}{d\Omega} \propto |<\psi_f|\boldsymbol{P}|\psi_i>\cdot\boldsymbol{A}_0|^2\delta(E_f-E_i-\hbar\omega). \tag{2.27}$$

Commutation relations of H_0 with $\boldsymbol{P}$ and $\boldsymbol{r}$ converts Eq. (2.27) into

$$\frac{d\sigma}{d\Omega} \propto |<\psi_f|\boldsymbol{r}|\psi_i>\cdot\boldsymbol{A}_0|^2\delta(E_f-E_i-\hbar\omega). \tag{2.28}$$

Equation (2.28) represents the photoionization cross-section when ψ_f and ψ_i are independent of the photoionization process itself. More precisely, we have to use the multi-particle picture. The wave function of a ground state of N particles is given by

$$\psi_0^N = \phi_i\Psi_i^{N-1}, \tag{2.29}$$

where ϕ_i is the single-particle wave function of the electron to be removed and Ψ_i^{N-1} is the properly antisymmetrized determinant of the remaining $N-1$ electrons. In the same way, the final state in the excitation process is written as

$$\psi_\mathrm{f} = u_k\Phi_{i,j}(N-1), \tag{2.30}$$

where u_k is a constant and $\Phi_{i,j}$ is the wave function of ions in which an electron in i th orbital is removed. j denotes all excited states of the ion with a hole in the i th orbital. Then the photoionization cross-section is given by

$$\frac{d\sigma}{d\Omega} \propto |<u_k|\boldsymbol{A}\cdot\boldsymbol{P}|\phi_i><\Phi_{i,j}|\psi_i>|^2. \tag{2.31}$$

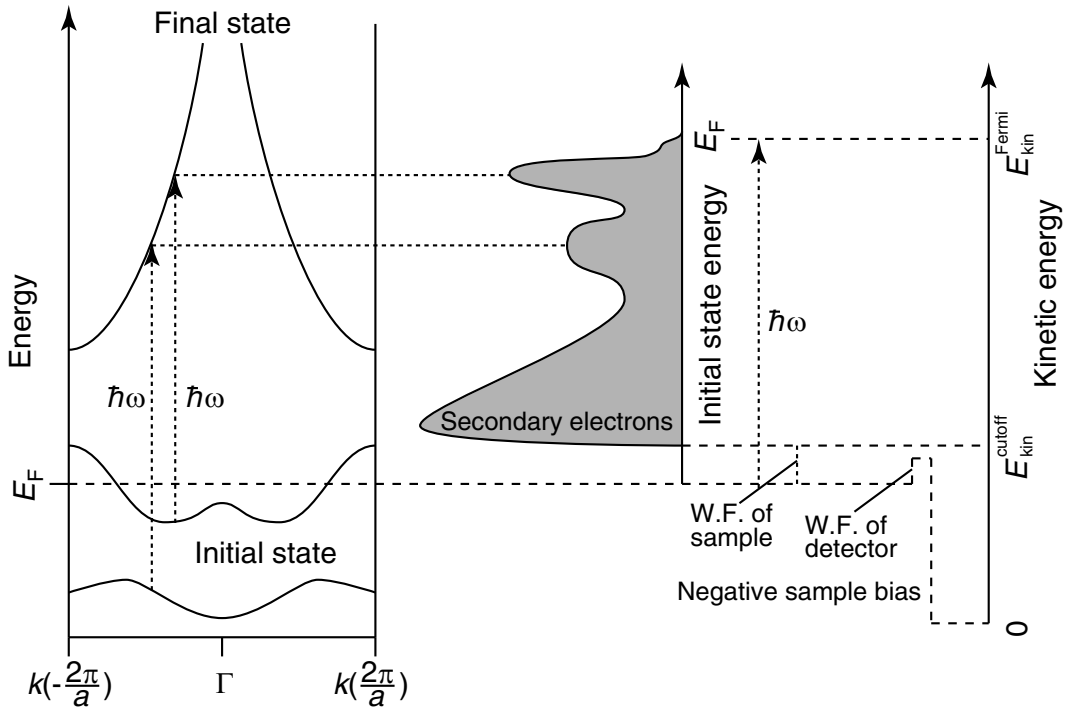

Figure 2.2: A schematic of the photoemission from a solid.

Next, we consider the conservation of energy in the photoioniaztion process:

$$\hbar\omega + E_0^N = E^{N-1}(i) + E_{\mathrm{kin}}(i), \tag{2.32}$$

where E_0^N is the total energy of the neutral particle system in the ground state, $E^{N-1}(i)$ is the total energy of the $N-1$ ionic system in the i th state, and $E_{\mathrm{kin}}(i)$ is the kinetic energy of the peak in the photoelectron spectrum corresponding to the i th state of the ion. The binding energy $E_{\mathrm{B}}(i)$ is defined as the characteristic of the state i and independent of the photon energy, as follows,

$$\begin{aligned} E_{\mathrm{B}}(i) + \mathrm{W.F.} &= \hbar\omega - E_{\mathrm{kin}}(i), \\ E_{\mathrm{B}}(i) &= E^{N-1}(i) - E_0^N, \end{aligned} \tag{2.33}$$

where W.F. denotes the workfunction of matter.

Figure 2.2 shows a schematic of the photoemission from a solid. Incident light excites electrons from initial states to final states. Then the excited electrons are emitted to vacuum conserving the distribution of the initial state energy. It should be noted that the workfunction of the sample is determined from the cutoff energy of secondary electrons. In practice, negative bias is applied to the sample to extract the secondary electrons. The cutoff of the kinetic energy of the secondary electrons $E_{\mathrm{kin}}^{\mathrm{cutoff}}$ and the kinetic energy of the electrons emitted from the Fermi

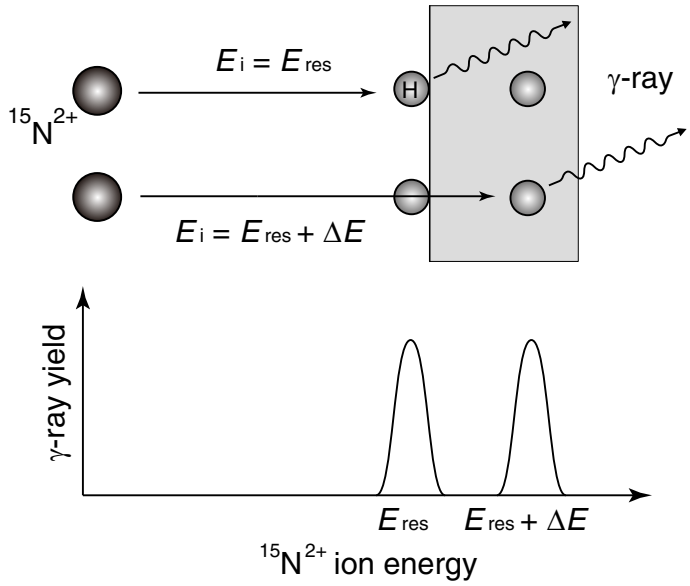

Figure 2.3: A schematic of NRA measurement for hydrogen on solide surfaces.

level $E_{\mathrm{kin}}^{\mathrm{Fermi}}$ gives the workfunction of the sample W.F.$_{\mathrm{sample}}$ as follows,

$$E_{\mathrm{kin}}^{\mathrm{Fermi}} - E_{\mathrm{kin}}^{\mathrm{cutoff}} = \hbar\omega - \mathrm{W.F.}_{\mathrm{sample}}. \tag{2.34}$$

$E_{\mathrm{kin}}^{\mathrm{cutoff}}$ is usually determined by the Fermi edge of metals such as gold.

2.1.3 Nuclear reaction analysis

Nuclear reaction analysis (NRA) via ^{1}H(^{15}N,$\alpha\gamma$)^{12}C enables us to know the depth profile of hydrogen in solids. Figure 2.3 shows a schematic of the NRA measurement. In NRA, accelerated $^{15}N^{2+}$ with an energy of around 6.385 MeV collides with hydrogen in a solid and induces a resonant nuclear reaction,

$$^{15}\mathrm{N} +^{1} \mathrm{H} \rightarrow^{12} \mathrm{C} +^{4} \mathrm{He} + \gamma. \tag{2.35}$$

The 4.43 MeV γ-ray emitted in the reaction at the narrow 6.385 MeV energy resonance E_{res} provides the signal proportional to the H concentration. H depth profiles are obtained by recording the γ-ray yield as a function of the incident $^{15}N^{2+}$ ion energy E_{i}. E_{i} and the stopping power dE/dz define the probing depth z as

$$z = \frac{E_{\mathrm{i}} - E_{\mathrm{res}}}{\left(\frac{dE}{dz}\right)}. \tag{2.36}$$

The depth resolution is mainly limited by the width of the Doppler-broadened energy resonance peak at $E_i = E_{res}$ and typically amounts to a few nanometers [99].

The γ yield I is quantitatively replaced with the H density by calibration of the γ-detection efficiency with a sample of known hydrogen concentration I_{ref}. We define a proportional constant

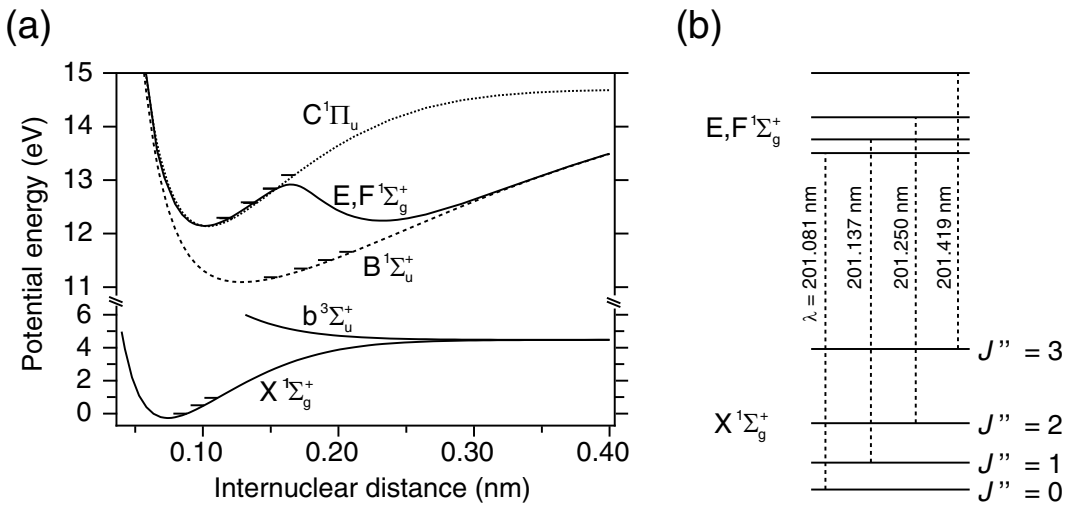

Figure 2.4: (a) The adiabatic potential of hydrogen molecules [100, 101, 102, 103, 104]. (b) A schematic of the $X^1\Sigma_g^+(v" = 0, J") \rightarrow E,F^1\Sigma_g^+(v' = 0, J' = J")$ transition.

α which makes the connection between γ yield and hydrogen volume density in a sample,

$$\alpha = \frac{dE}{dz}_{\text{ref}} \frac{I_{\text{ref}}}{C_{\text{ref}}}, \tag{2.37}$$

where dE/dz_{ref} is the stopping power of a reference, I_{ref} is the γ yield from the reference, and C_{ref} is the hydrogen concentration of the reference. Then, the hydrogen volume density of a sample C is given by

$$C = \frac{dE}{dz} \frac{I}{\alpha}. \tag{2.38}$$

2.1.4 Resonance enhanced multi-photon ionization

Resonance enhanced multi-photon ionization (REMPI) is a laser spectroscopy method for atoms and molecules. $(n+m)$-REMPI denotes a process where n photons resonantly excite an atom or a molecule and m photons ionize the excited particle. Our study uses the two-photon excitation of Q-branch between the $X^1\Sigma_g^+(v" = 0, J")$ and $E,F^1\Sigma_g^+(v' = 0, J' = J")$ states of hydrogen molecules.

The two-photon resonant transition probability from the $X^1\Sigma_g^+$ state to the $E,F^1\Sigma_g^+$ state M_{fi} is given by the second order perturbation of an electric dipole transition,

$$M_{fi} \propto \sum_n \frac{< \psi_f | \boldsymbol{A}_0 \cdot \boldsymbol{r} | \psi_n >< \psi_n | \boldsymbol{A}_0 \cdot \boldsymbol{r} | \psi_i >}{E_n - E_i - \hbar\omega}, \tag{2.39}$$

where ψ_f, ψ_n, and ψ_i are the wavefunctions of a final state, an intermediate state, and an initial state, respectively, and E_n and E_i are the energy of the intermediate state, and the initial state respectively. Finite $< \psi_f | \boldsymbol{A}_0 \cdot \boldsymbol{r} | \psi_n >$ and $< \psi_n | \boldsymbol{A}_0 \cdot \boldsymbol{r} | \psi_i >$ require the change of the parity

Table 2.1: Correction coefficients for (2+1)E,F$^1\Sigma_g^+ \leftarrow$ X$^1\Sigma_g^+$ REMPI of hydrogen molecules [105, 106].

J"	Experimental	Theoretical
0	1.12 ± 0.06 1.034	
1	···	1.031
2	1.04 ± 0.07	1.026
3	0.90 ± 0.06	1.019
4	0.88 ± 0.06	1.010
5	···	0.999
6	1.03 ± 0.04	0.987
7	0.94 ± 0.04	0.975
8	0.99 ± 0.11	0.958
9	0.90 ± 0.12	0.942
10	0.95 ± 0.12	0.927
11	1.04 ± 0.11	0.911
12	1.62 ± 0.32	0.977
13	1.44 ± 0.272	0.867
14	02.61 ± 0.67	1.076
15	1.72 ± 0.36	0.812

of the wavefunctions because $\boldsymbol{A}_0 \cdot \boldsymbol{r}$ has an odd parity. As a result, the parity of ψ_f and ψ_i is required to be the same. In addition, the electron spin and nuclear spin states remain unchanged during the transition with negligible spin-orbit interactions and hyper-fine interactions in the wavefunctions, because $\boldsymbol{A}_0 \cdot \boldsymbol{r}$ does not include spin operators. On the other hand, the change in the rotational quantum number ΔJ in the ψ_i-ψ_n and ψ_n-ψ_f transitions are ±1. This lets ΔJ in the transition between the initial and final states be ±2 or 0. The transition lines of $\Delta J = -2$, 0, and +2 are called O-branch, Q-branch, and S-branch, respectively.

Figure 2.4 (a) shows the adiabatic potential of hydrogen molecules [100, 101, 102, 103, 104]. The rotational energy of hydrogen molecules in the X$^1\Sigma_g^+$ and in the E,F$^1\Sigma_g^+$ is given by $E_{\rm rot} = B_{\rm X}J"(J"+1)$ ($B_{\rm X} \sim 7.5$ meV) and $E_{\rm rot} = B_{\rm E,F}J"(J"+1)$ ($B_{\rm E,F} \sim 4.1$ meV), respectively. Therefore, hydrogen molecules with different rotational quantum numbers are selectively measured by tuning the laser wavelength as shown in Fig. 2.4 (b).

Photoionization probability generally depends on $J"$. Correction coefficients for (2+1)E,F$^1\Sigma_g^+$ $\leftarrow$ X$^1\Sigma_g^+$ REMPI of hydrogen molecules are shown in Table 2.1. The correction coefficients for $J" = 0 \sim 3$ states obtained by experiments are almost in accordance with those by theory, which are around 1 independent of $J"$.

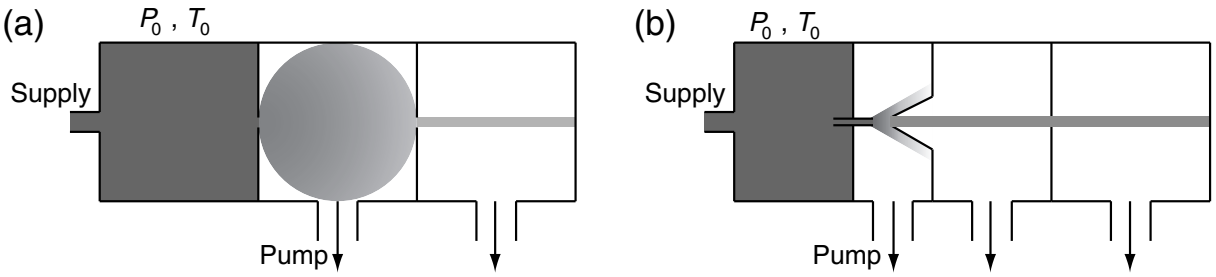

Figure 2.5: A schematic of (a) a thermal equilibrium molecular beam and (b) a supersonic molecular beam.

2.1.5 Molecular beam

A molecular beam is a linear flux of neutral particles such as atoms and molecules. The beam is categorized into two types depending on the balance between the mean free path of molecules and the size of the exit of the molecular beam.

One is the thermal equilibrium molecular beam, in which molecules with a mean free path of longer than the diameter of the exit is effused from the exit to a vacuum. As shown in Fig. 2.5 (a), the effused molecules pass through the apertures, and the shape becomes linear. The translational, vibrational, and rotational temperatures of the molecules follow the Boltzmann distribution defined by the initial temperature of the molecules [107, 108].

The other is the supersonic molecular beam, whose schematic is shown in Fig. 2.5 (b). In the beam, the mean free path of molecules at the exit is shorter than the diameter of the exit. The effused molecules adiabatically expand and the center of the flux is extracted by a skimmer. The adiabatic expansion narrows the distribution of the translational velocity and decreases the rotational temperature [107, 108].

Figure 2.6 shows a schematic of the adiabatic expansion of the supersonic molecular beam at the exit. Adiabatic expansion requires the condition for the pressure in the nozzle P_0 and the background pressure in the vacuum region P_b,

$$\frac{P_0}{P_\mathrm{b}} > \left(\frac{\gamma+1}{2}\right)^{\frac{\gamma}{\gamma+1}}, \tag{2.40}$$

where γ is the ratio of the specific heat, $C_\mathrm{p}/C_\mathrm{v}$ [109, 107]. C_p and C_v are the molar constant pressure specific heat and the molar constant volume specific heat, respectively. The right-hand side in Eq. (2.40) is smaller than 2.1 [107]. In the nozzle, molecules form a viscous flow, which is in equilibrium with the nozzle temperature of T_0. As a result, also at the exit of the nozzle, molecules collide with each other frequently. The collision transfers the thermal energy of the molecules into the translational energy toward the exit. As a result, the temperature of the molecules decreases and their Mach number, which is defined by the molecular velocity v divided by the acoustic velocity a, reaches 1. Then, the effused molecules migrate downstream as a molecular flow with an increased Mach number in the region called the zone of silence.

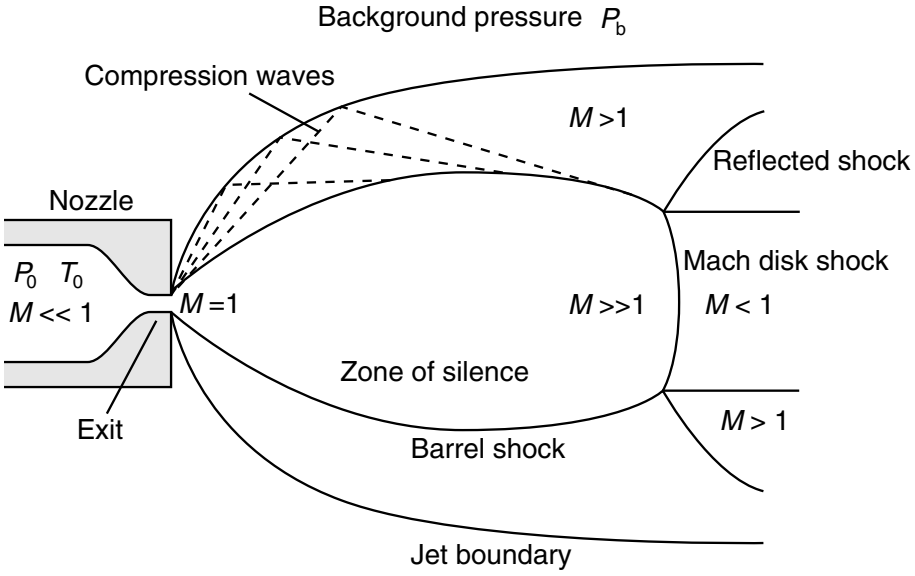

Figure 2.6: A schematic of adiabatic expansion of supersonic molecular beam at an exit [107].

Around the zone of silence, collisions of molecules form shock waves called barrel shoch and Mach disk. The position of the Mach disk x_{M} is empirically given by

$$\frac{x_{\mathrm{M}}}{d} = 0.67\left(\frac{P_0}{P_{\mathrm{b}}}\right)^{\frac{1}{2}}, \tag{2.41}$$

where d is the diameter of the nozzle exit [110, 109, 107]. At the Mach disk, the molecular flow from the zone of silence disappears because of the collisions of molecules. Therefore, the skimmer set at the upstream of the Mach disk extracts the molecular flow with the Mach number of above 1 and forms a supersonic molecular beam. The Mach number near the nozzle exit is given by

$$M \sim A\left(\frac{x}{d}\right)^{\gamma-1}, \tag{2.42}$$

where x is the position from the nozzle exit and A is a constant defined by γ [107]. A is 3.26 and 3.65 for monatomic and diatomic gas, respectively. Then, lack of collisions in the zone of silence lets the Mach number converge into M_{c}, whose value is empirically given by

$$M_{\mathrm{c}} = 2.05\left(\frac{\lambda_0}{d\epsilon}\right), \tag{2.43}$$

where λ_0 is a mean free path of molecules in the nozzle and ϵ is the collisional efficiency [107]. For example, ϵ for Ar and He is 0.25 and 0.1~0.5, respectively [107].

The Mach number defines the temperature and the velocity of the supersonic molecular beam

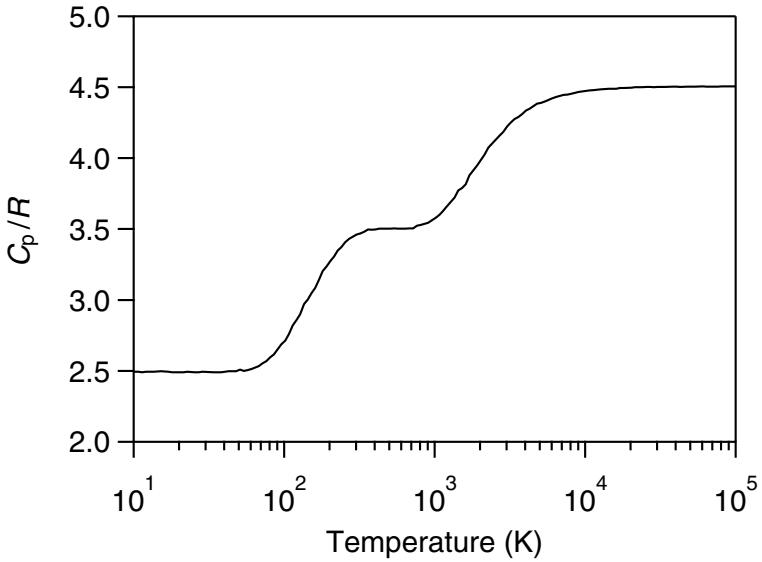

Figure 2.7: The specific heat capacity (C_p) of H_2 divided by the gas constant (R) as a function of temperature [111, 112].

as discussed below. The acoustic velocity is given by

$$a = \sqrt{\frac{\gamma RT}{W}}, \tag{2.44}$$

where R is the gas constant, T is the temperature of the molecules, and W is the molar weight of molecules [109, 107]. M is accordingly written as

$$M = \frac{v}{a} = v\sqrt{\frac{W}{\gamma RT}}. \tag{2.45}$$

For the supersonic molecular flow, the translational energy and the thermal energy of the molecules are treated independently. If C_p is assumed to be constant, the energy-conservation law is represented as

$$\frac{1}{2}Wv^2 = \int_T^{T_0} C_p dT, \tag{2.46}$$

where C_p is molar constant pressure specific heat. C_p generally depends on temperature, as shown in Fig. 2.7. In a first approximation, C_p is assumed to be constant. Rearrangement of Eq. (2.46) yields

$$\begin{aligned} v &= \sqrt{\frac{2C_p}{W}(T_0 - T)}, \\ &= \sqrt{\frac{2R}{W}\left(\frac{\gamma}{\gamma - 1}\right)(T_0 - T)}, \end{aligned} \tag{2.47}$$

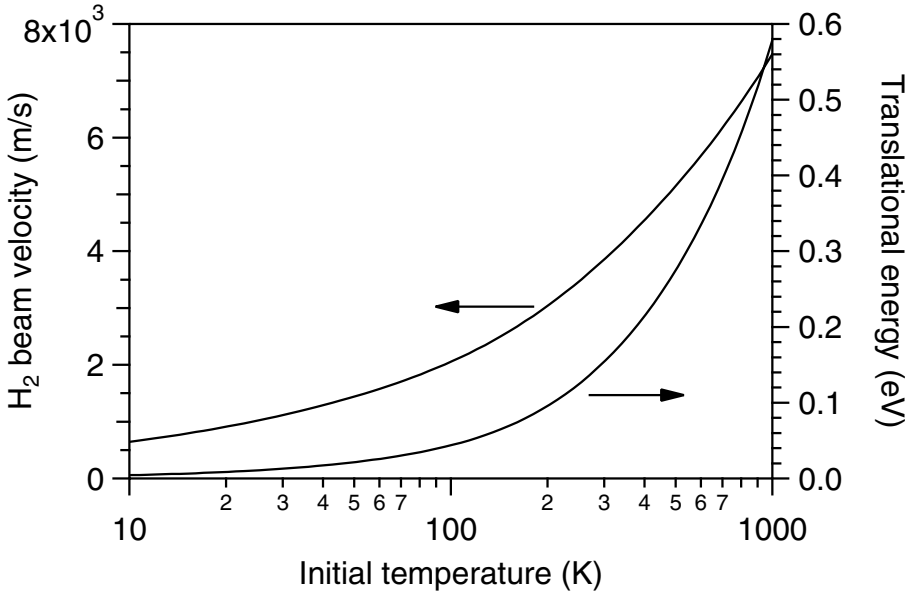

Figure 2.8: The calculated translational velocity of molecular hydrogen as a function of initial temperature.

where the relation $C_p = (R\gamma)/(\gamma - 1)$ is used. By combining Eq. (2.45) and Eq. (2.47), T and v are expressed as functions of M and γ,

$$\frac{T}{T_0} = \left(1 + \frac{\gamma - 1}{2} M^2\right)^{-1}, \tag{2.48}$$

$$v = M\sqrt{\frac{\gamma R T_0}{W}}\left(1 + \frac{\gamma - 1}{2} M^2\right)^{-\frac{1}{2}}. \tag{2.49}$$

Substituting Eq. (2.42) into Eqs. (2.48) and (2.49) gives T and v as a function of x.

For the molecular hydrogen case, however, C_p strongly depends on the temperature as shown in Fig. 2.7 [111, 112]. v of molecular hydrogen is directly calculated by Eq. (2.46) and the value of C_p in Fig. 2.7 with assumption that $T \sim 0$. Figure 2.8 shows the calculated v and the translational energy of the molecular hydrogen beam as a function of the initial temperature. At an initial temperature of 300 K, v and the translational energy were calculated to be 3850 m/s and 154 meV, respectively. As shown in Fig. 2.8, v and the translational energy can be modulated by the initial temperature, which is equivalent to the nozzle temperature. The velocity distribution of a supersonic beam is known to be given by a Shifted-Maxwell-Boltzmann distribution with the drift velocity v,

$$f(u)du \propto u^2 \exp\left(-\frac{m(u - v)^2}{2k_B T}\right) du. \tag{2.50}$$

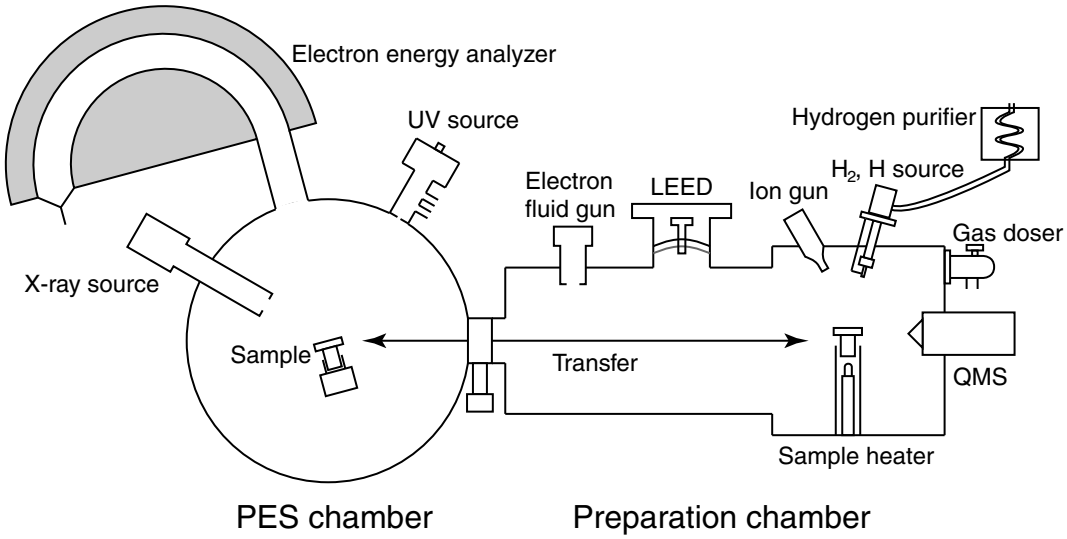

Figure 2.9: A schematic of an apparatus for photoemission spectroscopy.

2.2 Apparatus

2.2.1 Apparatus for PES

Photoemission spectroscopy was performed in the apparatus shown in Fig. 2.9. The apparatus consists of two UHV chambers for photoemission spectroscopy and sample preparation.

Samples were prepared in the preparation chamber with a base pressure of 3×10^{-7} Pa. For electron irradiation experiments, an electron gun (Kimball Physics, 3H-1399) and the controller (Kimball Physics, EGPS-3H X) were used. The beam energy range, beam current, and spot size of the electron beam are 0 to 1500 eV, 0.2 to 10 mA, and 20 to 50 mm, respectively. The electron flux was measured as a function of the electron energy with a Faraday cup set at 150 mm from the electron gun, as shown in Fig. 2.10. The electron flux is approximately proportional to the square of the distance between the electron gun and a target d. Then, a fitting to the measured values gives the electron flux F_e ($\mathrm{cm^{-2}s^{-1}}$) at a distance of d (mm) with an electron energy of E_e (V),

$$F_\mathrm{e} = \left[-7.89 \times 10^{14} + \frac{6.91 \times 10^{15}}{1 + \exp\left(\frac{442 - E_\mathrm{e}}{202}\right)} \right] \left(\frac{150^2}{d^2} \right). \tag{2.51}$$

Molecular hydrogen to which samples were exposed was purified by a palladium-diffusion hydrogen purifier (Power+Energy Inc., model 3001). Atomic hydrogen was prepared by a hot tungsten tube heated at 1900 K, on which introduced molecular hydrogen thermally dissociates.

After preparation, the samples were transferred to the chamber for photoemission spectroscopy, which is equipped with an electron energy analyzer, an ultraviolet (UV) source, and an X-ray source (VG cienta, ESCA-lab II). The typical base pressure of the chamber was 1×10^{-8} Pa. The UV source emits the He I line ($h\nu$ = 21.22 eV) and He II line ($h\nu$ = 23.1 eV) by

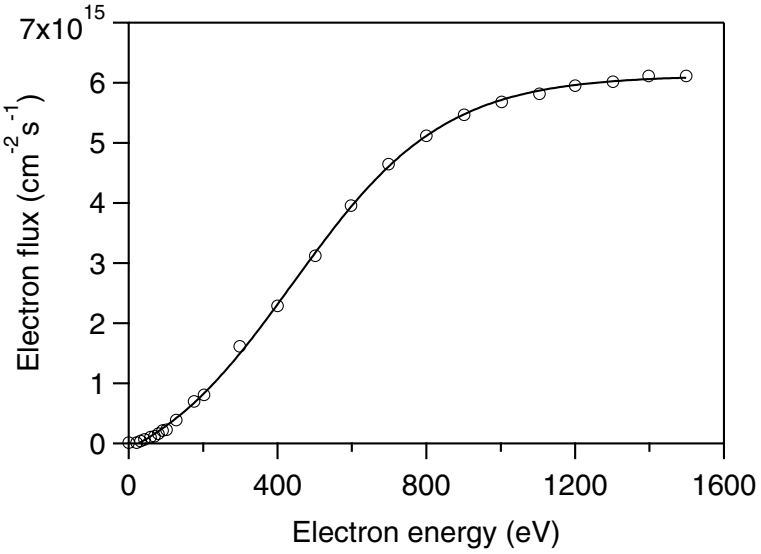

Figure 2.10: Electron flux emitted by an electron gun (Kimball Physics, 3H-1399) as a function of the electron energy. The circles denote values measured with a Faraday cup set at 150 mm from the electron gun and the solid line denotes a fitting curve.

discharge of He. The X-ray source provides two types of light, Al K_α ($h\nu$ = 1487 eV) and Mg K_α ($h\nu$ = 1254 eV). The energy analyzer was controlled by a home-made LabVIEW program. The energy resolution for He I UPS and XPS was estimated as 150 meV and 2 eV from the broadening of the Fermi edge and a $4f_{7/2}$ peak of Au, respectively.

2.2.2 Apparatus for NRA

For NRA, accelerated $^{15}N^{2+}$ ions were prepared in an accelerator, 5 MV vertical tandem-type Van der Graaf accelerator (Peletron corp.) at Micro Analysis Laboratory, Tandem Accelerator (MALT) in The University of Tokyo. Schematic of the accelerator is shown in Fig. 2.11 (a). At the first step of the generation of the $^{15}N^{2+}$ ions, a cathode target, which is a mixture of $Ti^{15}N$ and C, is sputtered by Cs^+ accelerated to 6 keV. The sputtering produces $C^{15}N^-$ ion, which is injected to the first stage of the accelerator. The $C^{15}N^-$ is accelerated to about 3 MeV and collides with Ar gas at the terminal. The collision changes the $C^{15}N^-$ into $^{15}N^{2+}$ ion, which is accelerated to $\sim$ 6.4 MeV in the second stage of the accelerator. An analyzing magnet chooses the mass of the ion and analyzes the energy. The obtained $^{15}N^{2+}$ beam is introduced to a beam line of 1E or 1C by a switching magnet.

The experiments for $SrTiO_3$(001) surfaces were performed in an UHV chamber with a base pressure of 2×10^{-8} Pa at the 1E beam line. A schematic of the chamber is shown in Fig. 2.11 (b). The experimental components in the chamber are similar to these in the preparation chamber for PES. Molecular hydrogen is purified by the purifier (Power+Energy Inc., model 3001) before the exposure of molecular hydrogen and atomic hydrogen. The electron gun is the

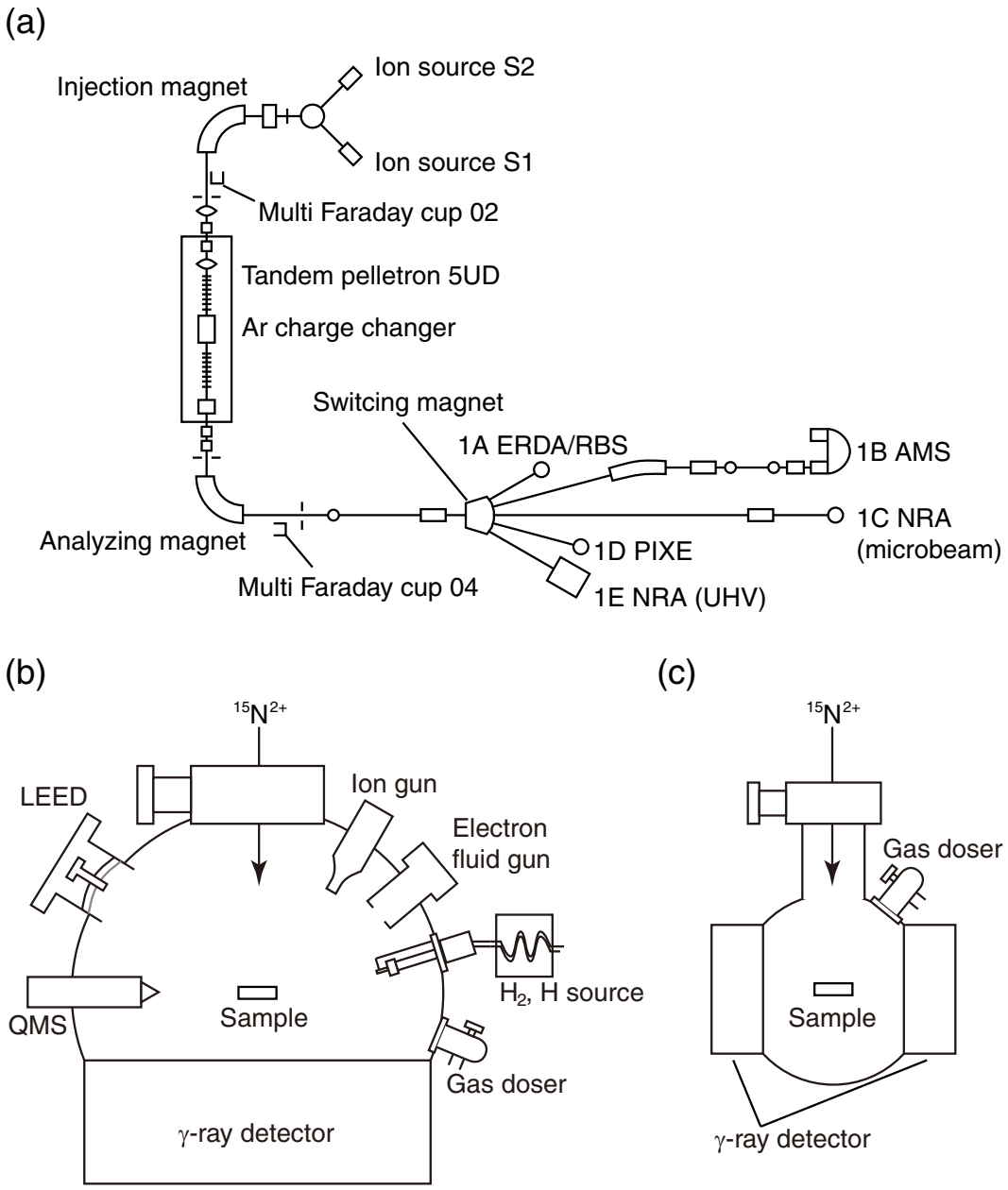

Figure 2.11: Schematics of (a) a 5 MV vertical tandem-type Van der Graaf accelerator and beam lines, (b) a chamber at 1E beam line, and (c) a chamber at 1C beam line.

same as that used in the PES experiments. The electron flux is accordingly estimated by Eq. (2.51). γ-ray emitted in NRA experiments is detected by a γ-ray scintillator behind the sample.

The experiments for a stainless steel surface were performed in another UHV chamber illustrated in Fig. 2.11 (c) with a base pressure of 1×10^{-5} Pa at the 1C beam line. The $^{15}N^{2+}$ beam intensity and the sensitivity for the γ-ray detection were approximately twice as high as that in the 1E beam line, because two γ-ray detectors were installed in the chamber.

2.2.3 Development of apparatus for hydrogen scattering experiments

In this section, the apparatus used for hydrogen scattering experiments, which we have developed in the present work, is described. The apparatus mainly consists of an atomic and molecular hydrogen beam source and a state-selective detective system for hydrogen by REMPI.

Outline

A scale model and a schematic of the system are shown in Fig. 2.12 and Fig. 2.13 (a), respectively. For the molecular hydrogen beam, a nozzle made of quartz glass or stainless steel with exit diameters of between 30 μm and 500 μm is mounted on an xy stage. The inlet pressure of molecular hydrogen is $10^2 \sim 10^5$ Pa depending on the nozzle exit diameter. Then, the nozzle introduces molecular hydrogen into the first chamber with a skimmer. Passing through a differential pumping and an aperture, the molecular hydrogen is introduced into the sample chamber as a beam.

For the atomic hydrogen beam, on the other hand, a quartz glass nozzle with an exit diameter of 500 μm is directly attached to the first chamber instead of the nozzle for molecular hydrogen. A microwave cavity is mounted on the front side of the O-ring seal. Microwave generated by the cavity dissociates molecular hydrogen into atomic hydrogen with an inlet pressure of $\sim$ 100 Pa. If the position of the microwave cavity is far from the nozzle exit, the generated atomic hydrogen recombines to form molecular hydrogen on the quartz glass surface. Therefore, the cavity was placed as close to the flange as possible.

The molecular or atomic hydrogen beam is directly characterized by a quadrupole mass spectrometer or REMPI in the sample chamber. For scattering experiments, a sample is exposed to the molecular hydrogen beam. Scattered molecular hydrogen from the sample is measured with REMPI. Molecular hydrogen ionized by REMPI is collected by an ion optical system with an electric lens and a repeller. Then a micro channel plate (MCP) detects the H_2^+ ions produced by (2 + 1)REMPI.

H_2(2 + 1) REMPI *via* E,F$^1\Sigma_g^+ \leftarrow$ X$^1\Sigma_g^+$ is performed with laser with a wavelength of $\sim$ 201 nm. A schematic of the laser system is shown in Fig. 2.13 (b). Nd:YAG laser (Continuum8010) generates light with λ =532 nm by the second harmonic of the fundamental light with λ =1064 nm. The 532 nm light with a power of $<$ 300 mJ/pulse pumps dye laser (Lambda Physik SCANMATE 2E) whose dye is Rhodamin640 (Oscillator and Preamplifier: 79.4 mg/l, Amplifier: 22.5 mg/l). The generated light with $\lambda \sim$ 605 nm by the dye laser is frequency-tripled with two β-

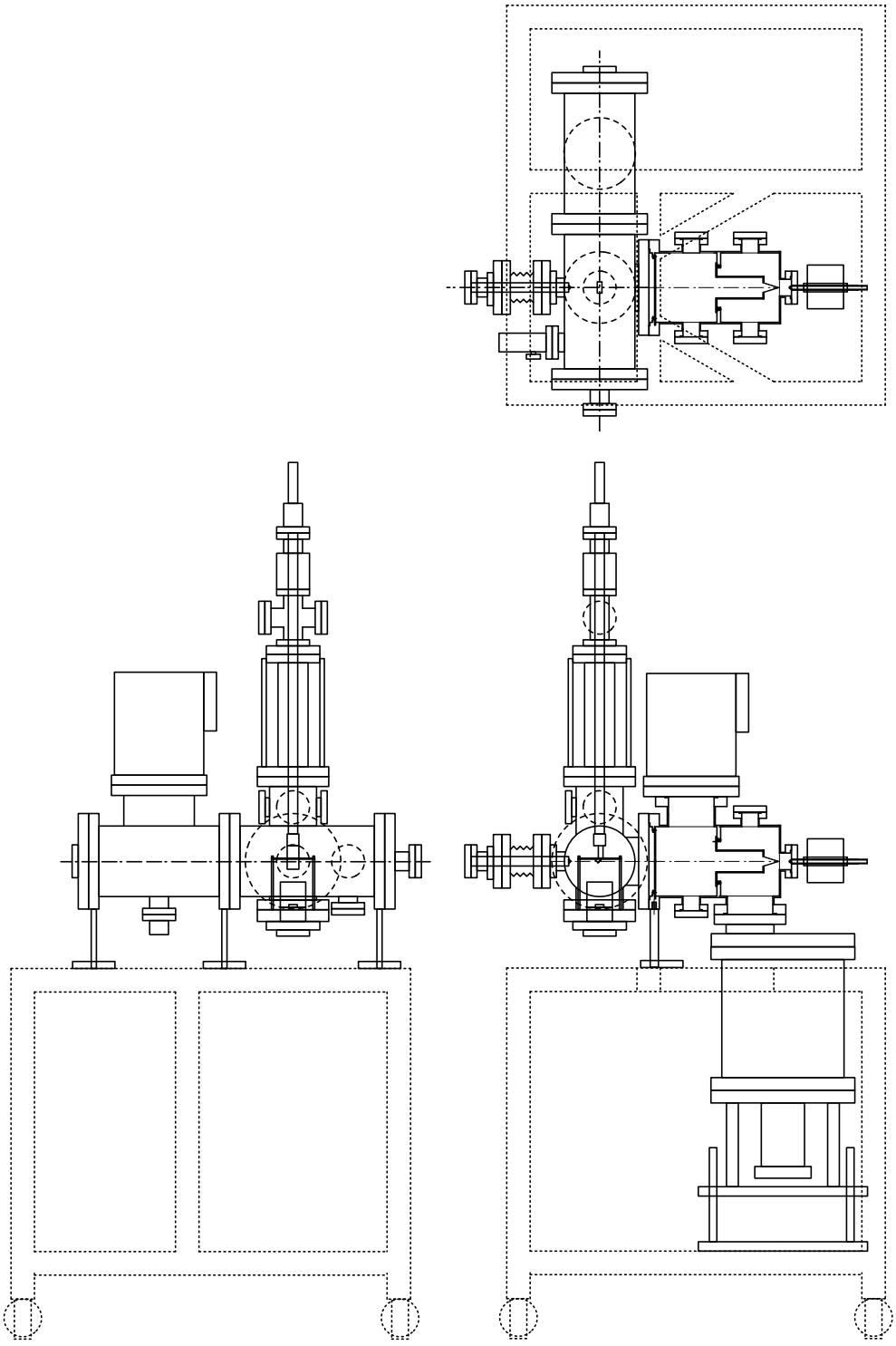

Figure 2.12: A scale model of an apparatus used for hydrogen scattering experiments.

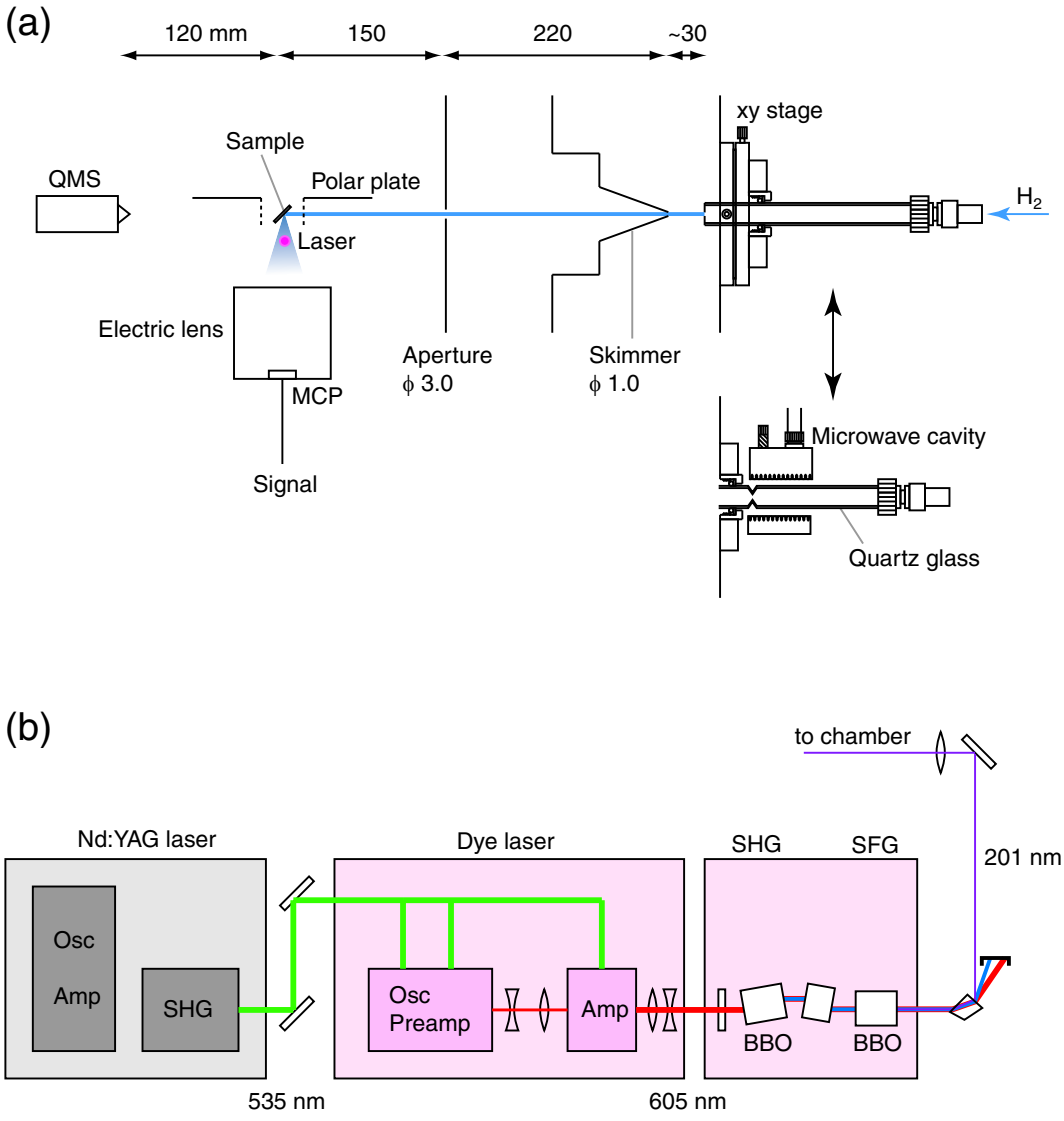

Figure 2.13: Schematics of (a) the apparatus for hydrogen scattering experiments and (b) laser system for REMPI.

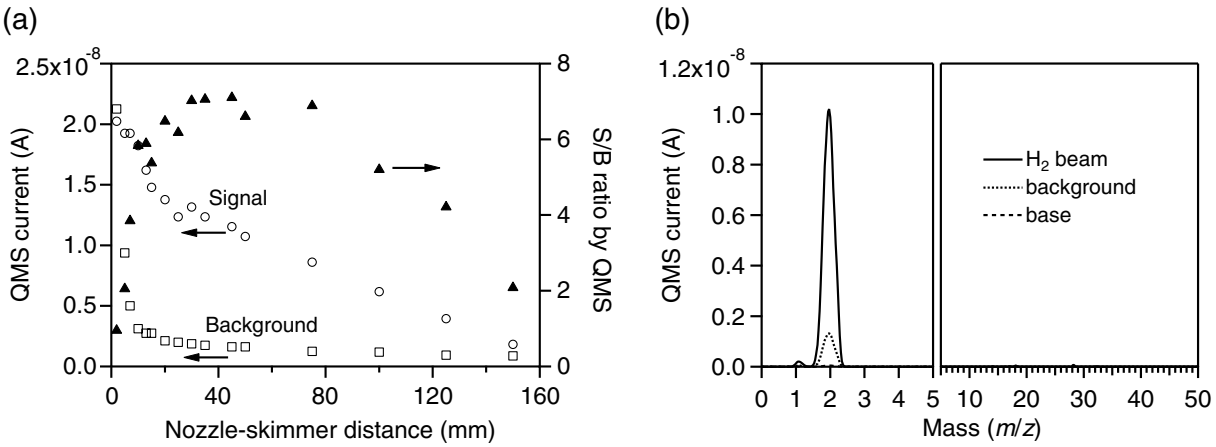

Figure 2.14: (a) The nozzle-skimmer distance dependence of H_2 beam intensity, the background, and the signal-background ratio measured by QMS for nozzle exit diameter of 500 μm. (b) QMS spectra of H_2 beam, the background, and the base pressure for the nozzle diameter of 500 μm with the nozzle-skimmer distance of 30 mm and the nozzle pressure of 100 Pa.

BaB_2O_4 (BBO) crystals, where the second harmonic and the sum frequency produce the light with $\lambda \sim 201$ nm.

Adjustment of molecular hydrogen beam

The intensity of the molecular hydrogen beam depends on the distance between the nozzle exit and the skimmer. After the beam alignment, the nozzle-skimmer distance dependence of the beam intensity and the background was measured by QMS. The background was derived from the pressure rise in the sample chamber by the beam incidence, which was measured by cutting the beam with a shield in front of QMS. It should be noted that the beam signal and the background (S/B) ratio measured by QMS is not in accordance with the true S/B ratio, because the sensitivity of QMS for the background is higher than that for the beam, and the background due to the difference in their incident solid angle. Figure. 2.14 (a) shows the signal, background, and S/B ratio at a nozzle-exit diameter of 500 μm. The inlet H_2 pressure in the nozzle was 100 Pa and the pressure in the first chamber was 2×10^{-2} Pa. In Fig. 2.14 (a), the beam signal and the background monotonically decreased as the nozzle-skimmer distance increased. On the other hand, the S/B ratio showed a maximum at the nozzle-skimmer distance of between 30 mm and 80 mm. The decrease of the S/B ratio at the distance of above 80 mm is considered to be caused by the Mack disk, where the beam intensity is drastically lowered by scattering. The position of the Mach disk calculated from Eq. (2.42) was 75 mm, which is consistent with the result. On the other hand, the low S/B ratio at the distance of below 30 mm can be explained as follows. A large part of the molecular hydrogen effused from the nozzle goes into the differential pumping chamber, which increased the pressure. The filled hydrogen in the differential pumping chamber

diffused into the sample chamber and increased the background.

Figure 2.14 (b) shows the QMS spectra for the nozzle diameter of 500 μm with the nozzle-skimmer distance of 30 mm and the nozzle pressure of 100 Pa. The S/B ratio measured with QMS was 7.0 as also shown in Fig. 2.14 (b). The introduction of the H_2 beam into the sample chamber increased the QMS signals at the mass of 18 and 28, whose intensity is 1/200 as high as H_2 beam itself.

The flux F ($m^{-2}s^{-1}$) of the molecular beam at a chamber can be evaluated from the pressure increase in the chamber ΔP. In a steady state, the increase of the number of molecules in a chamber per unit time by incident molecular beam $dN_{\rm beam}/dt$ is identical to the number of pumped molecules per unit time $dN_{\rm pump}/dt$,

$$\frac{dN_{\rm beam}}{dt} = \frac{dN_{\rm pump}}{dt}. \tag{2.52}$$

Pumping speed S ($m^3\ s^{-1}$) and the change of the volume density of molecules by incident beam in the chamber Δn (m^{-3}) gives $dN_{\rm pump}/dt$ as

$$\frac{dN_{\rm pump}}{dt} = \Delta n \cdot S \tag{2.53}$$

$$= \frac{\Delta P \cdot S}{k_{\rm B}T}, \tag{2.54}$$

where the relation $\Delta P = \Delta n k_{\rm B} T$ is used. The molecules are regarded as in equilibrium with chamber temperature T. On the other hand, $dN_{\rm beam}/dt$ is given by

$$\frac{dN_{\rm beam}}{dt} = FA, \tag{2.55}$$

where A (m^2) is the cross section of the beam. Combining Eqs. (2.52)-(2.55) yields

$$F = \frac{\Delta P S}{A k_{\rm B} T}. \tag{2.56}$$

In the case of Fig. 2.14 (b), ΔP of 1.1×10^{-6} Pa, S for H_2 of 0.35 $m^3 s^{-1}$, and the aperture diameter of 3.0 mm evaluated the beam flux of 1.3×10^{15} $cm^{-2}s^{-1}$.

For the other nozzle-exit diameter, the nozzle-skimmer distance of 20~30 mm was employed as results of similar calibration. The flux of the beam with the nozzle exit diameter of 30 μm and a inlet H_2 pressure of 1.3×10^4 Pa is 3×10^{15} $cm^{-2}s^{-1}$.

Adjustment of atomic hydrogen beam

The atomic hydrogen beam is generated by the dissociation of molecular hydrogen with microwave irradiation. Microwave accelerates electrons in gas atmosphere, which collide with molecular hydrogen. The collision dissociates molecular hydrogen into mainly atomic hydrogen at the ground state or excited states. The accelerated electrons also ionize atomic hydrogen

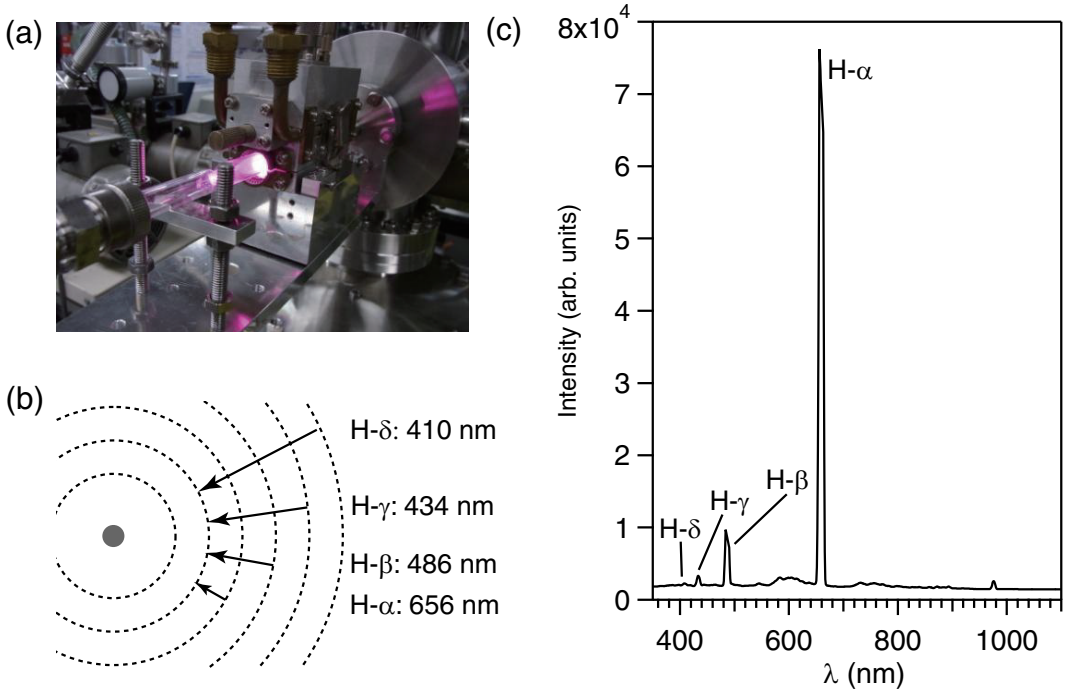

Figure 2.15: (a) Emission from molecular hydrogen irradiated with microwave. (b) A schematic of Balmer series. (c) A typical spectrum for H_2 dissociation with the H_2 inlet pressure and the microwave power of 80 Pa and 85 W, respectively.

by collision. The atomic hydrogen at the excited states emits the light, as shown in Fig. 2.15 (a). In particular, the transition from excited states to the state with the principal quantum number of 2 emits visible light, which is called the Balmer series. Figure 2.15 (b) shows a schematic of the transition for the Balmer series. Light emitted by $(3 \rightarrow 2)$, $(4 \rightarrow 2)$, $(5 \rightarrow 2)$, and $(6 \rightarrow 2)$ transitions are called H-α, H-β, H-γ, and H-δ lines, whose wavelength are 656 nm, 486 nm, 434 nm, and 410 nm, respectively. Figure 2.15 (c) shows a typical spectrum for H_2 dissociation in the apparatus measured with optical emission spectrometer (Rover Scientific, LN/CCD-1100PF/UV). The H_2 inlet pressure and the microwave power were 80 Pa and 85 W, respectively. With the assumption that the excitation and deexcitation probability of atomic hydrogen is independent of external parameters such as microwave power and pressure, the total intensity of the Balmer series is proportional to the volume density of atomic hydrogen generated in the quartz glass.

Figure 2.16 (a) shows the microwave power dependence of the emission intensity, which is the integral of the Balmer series. The inlet pressure of molecular hydrogen in the quartz glass was 80 Pa. The emission intensity gradually increases above the microwave power of 20 W, which is the threshold power of the plasma generation. As the microwave power exceeds 80 W, the emission intensity dramatically increased and then gradually decreased. The behavior is due to the balance of the translational energy of electrons and the collision cross section. With the power of above 85 W, microwave accelerates electrons which provide molecular hydrogen with the dissociation energy. On the contrary, the effective cross section of collisions between

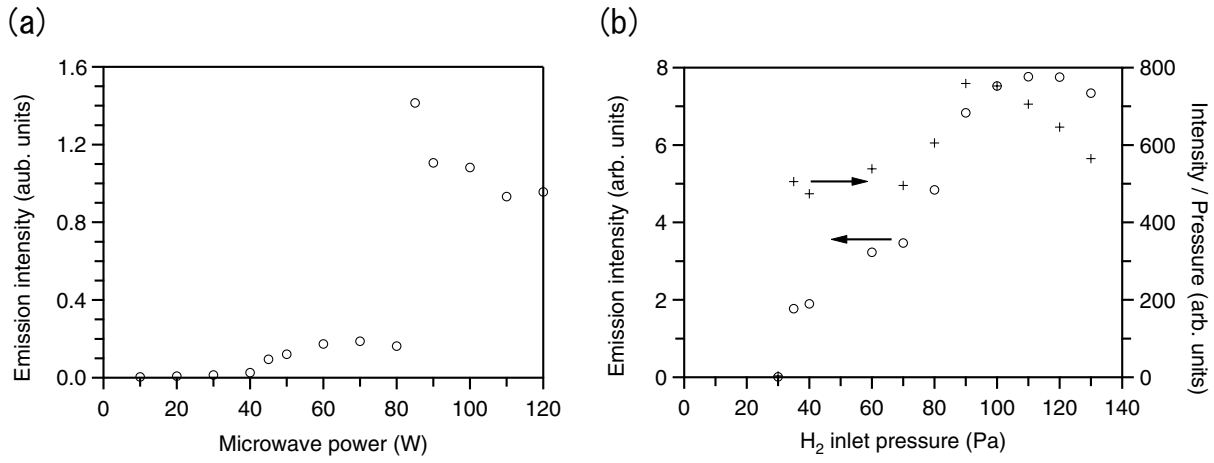

Figure 2.16: The emission intensity of the microwave discharge of molecular hydrogen as a function of (a) microwave power and (b) H_2 inlet pressure. The emission intensity divided by the H_2 inlet pressure is also plotted on the right-hand axis in (b).

the electrons and molecular hydrogen decreases at a higher electron energy, which leads to reduction of the dissociation rate of H_2.

In Fig. 2.16 (b), the emission intensity is plotted on the left-hand axis as a function of the H_2 inlet pressure in the quartz glass. The microwave power was 85 W. The emission intensity started to increase at a pressure of 30 Pa, showed a maximum at 110 Pa, and then decreased. The behavior can be explained as follows. The discharge probability increases with increasing number density of hydrogen, which is proportional to the pressure. On the other hand, the flow velocity of hydrogen in the region is accelerated with the increase of the pressure. Higher current velocity lowers the sojourn time of hydrogen in the discharge region, which decreases the dissociation probability. The competition of the two factors yields a maximum for the emission probability. In order to consider the dissociation rate for each hydrogen molecule, the emission intensity divided by the H_2 inlet pressure is plotted on the right-hand axis in Fig. 2.16 (b). The trend is similar to that of the simple emission probability, though, the position of the maximum moved to around the H_2 inlet pressure of 100 Pa.

These results suggest that the microwave power of around 85 W and the H_2 inlet pressure of around 100 Pa are appropriate for the efficient dissociation of molecular hydrogen. Figure 2.17 shows the QMS spectra for the hydrogen beam with and without microwave irradiation, from which the background is subtracted. The dissociation of molecular hydrogen by the microwave irradiation results in a peak for atomic hydrogen in the QMS spectra. The change in the peak height for molecular hydrogen evaluated the dissociation rate, because the QMS sensitivity for H and H_2 is different. The dissociation rate α is given by

$$\alpha = \frac{I_{\mathrm{on}} - I_{\mathrm{off}}}{I_{\mathrm{on}}}, \tag{2.57}$$

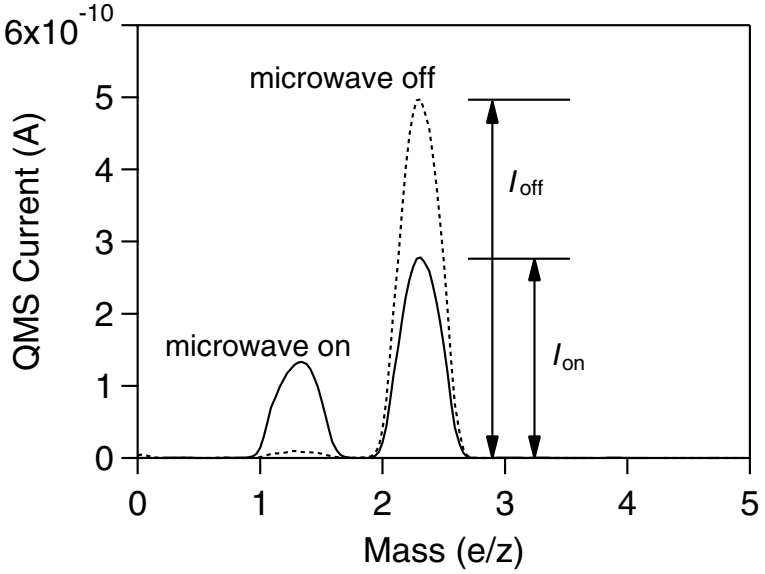

Figure 2.17: QMS spectra of hydrogen beam with and without microwave irradiation after background subtraction.

where I_{on} and I_{on} are the peak height for H_2 with and without microwave irradiation, respectively. From Eq. (2.57), α was calculated to be 0.45. The flux of the atomic hydrogen beam was 6.6×10^{13} cm^{-2}s^{-1}.

Characterization of H_2 beam by REMPI

Width of H_2 beam

The space distribution of the H_2 beam was characterized by REMPI. When the H_2 beam from the nozzle with the exit diameter of 500 μm was introduced in the measurement chamber, the REMPI signal of H_2 with $J = 1$ state was measured as a function of the laser position, as shown in Fig. 2.18. The possible H_2 beam width of 4.2 mm was geometrically determined by lines through the exit of the nozzle and the edge of the aperture in the system shown in Fig. 2.12. The H_2 beam width estimated from Fig. 2.18 was 4.2 $\sim$ 4.4 mm, which is consistent with the geometrical beam width. Thus, REMPI has confirmed that the H_2 beam width is characterized by the geometric structure.

Rotational temperature of H_2 beam

In order to estimate the rotational temperature of the H_2 beam, the REMPI spectra of a gas phase H_2 was used for the normalization of the intensity. Figure 2.19 (a) shows REMPI spectra of gas phase H_2 with a pressure of 2.5×10^{-5} Pa measured at room temperature. Fitting with a Gaussian to each rotational-state profile gives the ratio of the REMPI signals for $J = 0 \sim 3$ states as 1 : 3.23 : 0.68 : 0.35. The population of the $J = 0 \sim 3$ states is theoretically given by

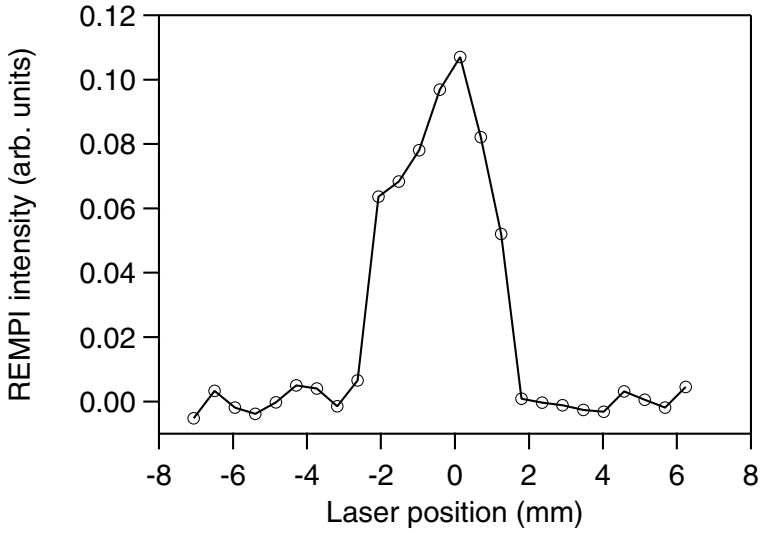

Figure 2.18: REMPI signal of hydrogen with the $J = 1$ state as a function of the laser position with H_2 beam incidence.

the Boltzmann distribution,

$$I = g_N(2J+1)\exp\left(-\frac{E_{\rm rot}}{k_{\rm B}T}\right), \tag{2.58}$$

where I is the population of a state, g_N is the nuclear-spin degeneracy of the state, and $E_{\rm rot}$ is the rotational energy of the state. Equation (2.58) gives the ratio of the population of the $J = 0 \sim 3$ states at room temperature as $1.00 : 5.03 : 0.87 : 0.64$. The mismatch between the measured ratio and the theoretical ratio is derived from laser conditions. The ratio between the measured populations and the theoretical populations is used for the correction of signals of the measured REMPI spectra.

Figure 2.19 (b) shows a REMPI spectrum for the H_2 beam. The diameter of the used nozzle was 30 μm, the inlet H_2 pressure in the nozzle was 1.0×10^4 Pa, and the beam flux at the measurement position was 3×10^{15} cm^{-2}s^{-1}. Gaussian fitting to the spectrum yields the population of the $J = 0 \sim 3$ states. The obtained population was normalized to the correction factor as obtained from the gas phase measurement. Figure 2.19 (c) shows the normalized population of $J = 0 \sim 3$ states. The rotational temperature $T_{\rm rot}$ of the beam is estimated from a Boltzmann plot of Fig. 2.19. The transformation of Eq. (2.58) yields

$$ln\left[\frac{I}{g_N(2J+1)}\right] = -\frac{1}{k_{\rm B}T_{\rm rot}}E_{\rm rot}, \tag{2.59}$$

where $T_{\rm rot}$ is the rotational temperature. Equation (2.59) means that $T_{\rm rot}$ is estimated from the gradient of a Boltzmann plot. Figure 2.19 (d) shows the Boltzmann plot of Fig. (2.19) (c). Fitting with a straight line on the Boltzmann plot estimated the rotational temperature of the beam as 308 ± 42 K, which is equal to the room temperature in the range of error.

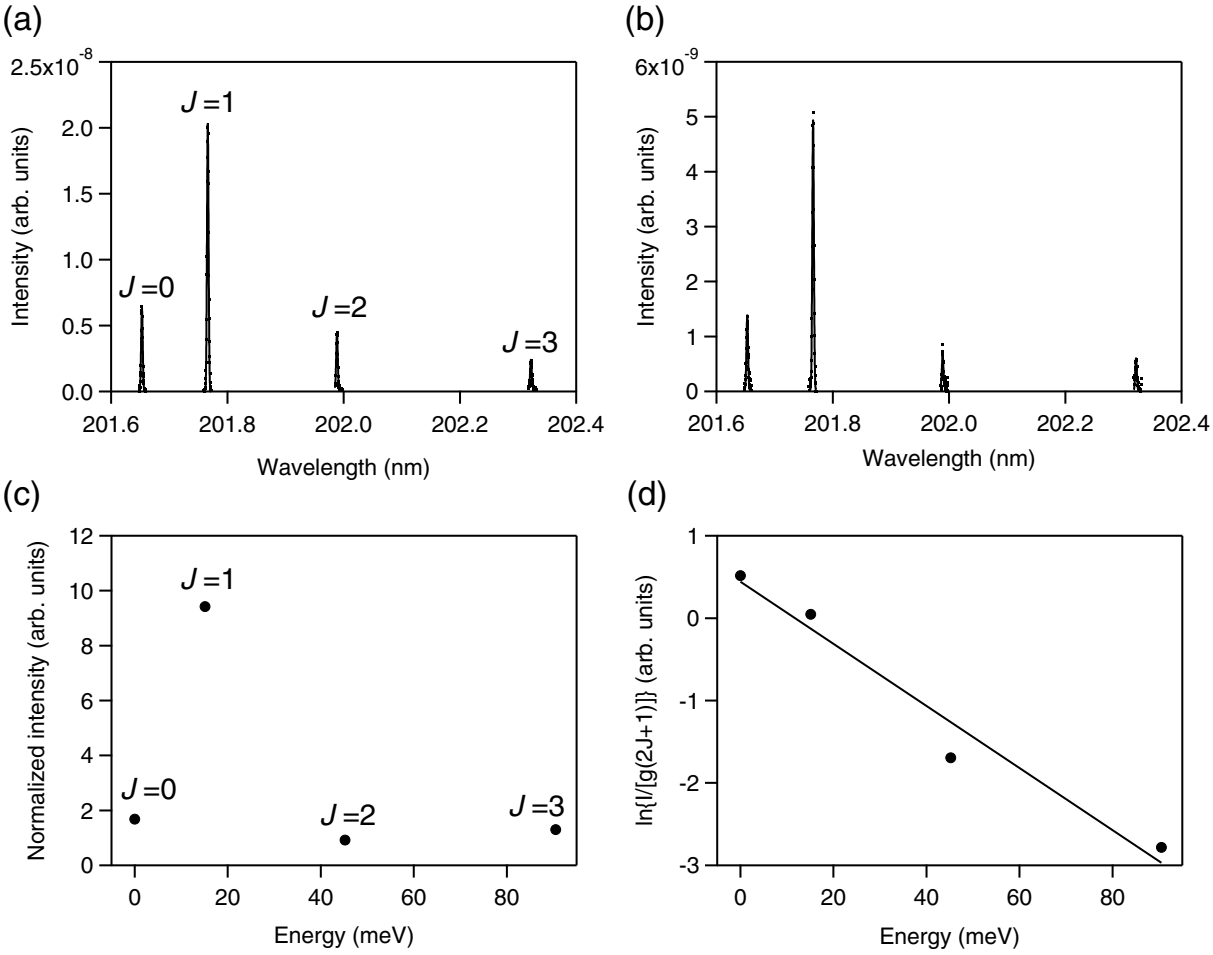

Figure 2.19: REMPI spectra of (a) a gas phase of H_2 and (b) the H_2 beam. (c) The adjusted population of the $J = 0 \sim 3$ states in the H_2 beam. (d) The Boltzmann plot of the population in the H_2 beam.

2.3 Samples

This chapter introduces $SrTiO_3$(001) surfaces and stainless steel surfaces, which were used in the present study as a single crystal oxide surface and an inhomogeneous oxide surface, respectively.

2.3.1 $SrTiO_3$

$SrTiO_3$ is a typical perovskite type transition metal oxide. The unit cell of $SrTiO_3$ is shown in Fig. 2.20. It forms a layer-by-layer structure along the [001] axis, in which the TiO_2 layer and SrO layer are stacked alternately. $SrTiO_3$ with the stoichiometric composition is an insulator with a band gap of 3.17 eV [113, 114]. Carriers can be doped by the replacement of cations [115] or the formation of oxygen vacancies [116]. The doping modulates the bulk carrier density

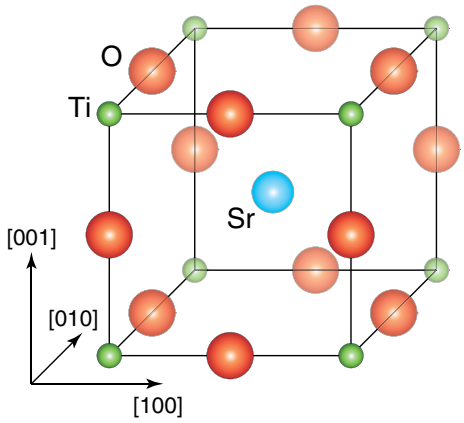

Figure 2.20: A schematic of the unit cell of $SrTiO_3$.

of between 10^{18} cm^{-3} and 10^{21} cm^{-3} and changes the bulk into a superconductor with T_c of $0.1 \sim 0.5$ K [117].

2.3.2 Surfaces of $SrTiO_3$(001)

The surface of $SrTiO_3$ has received greater attention in recent years due to photocatalytic activity under visible light [27, 118, 119] and generation of a two-dimensional electron gas [120, 121] as well as for the substrate of oxide-based devices [122, 123].

The structure of $SrTiO_3$ changes as a function of temperature. Cleaning the surface by the heat treatment under 800 °C keeps the structure (1×1) [124, 125]. Approximately 90 % of the surface is covered by the TiO_2 layer and the rest shows a SrO layer [126]. When it is heated to a higher temperature, desorption of oxygen atoms induces the reconstructions of the surface structure. The surface shows (2×1) and (4×4) structures by UHV annealing up to 800 °C and 900 °C, respectively [127, 128]. Upon annealing at higher temperatures the surface changes into (2×2) and $(\sqrt{5} \times \sqrt{5}) - R26.6$ structures [129, 130, 131]. The surface was reported to be perfectly terminated by a TiO_2 layer after the etching in a pH-controlled buffered NH_4F-HF (BHF) solution, however, subsequent annealing at $600 \sim 800$ °C forms a bilayer of TiO_2 with the (2×1) periodicity [132].

If we look at the electronic property of the surface, the surface is also insulating with stoichiometric composition. Recent works revealed that the Nb-doped semiconducting surface becomes metallic by cleavage [120], UV irradiation [121], and the adsorption of atomic hydrogen [71, 72]. In the two former cases, two dimensionality of the conductive electrons has also been observed.

2.3.3 Stainless steel

Stainless steel is an alloy, which mainly consists of Fe, Cr, and Ni. Fe and the other metal atoms are randomly located on the lattice position in a unit cell. The phases of the stainless steel are

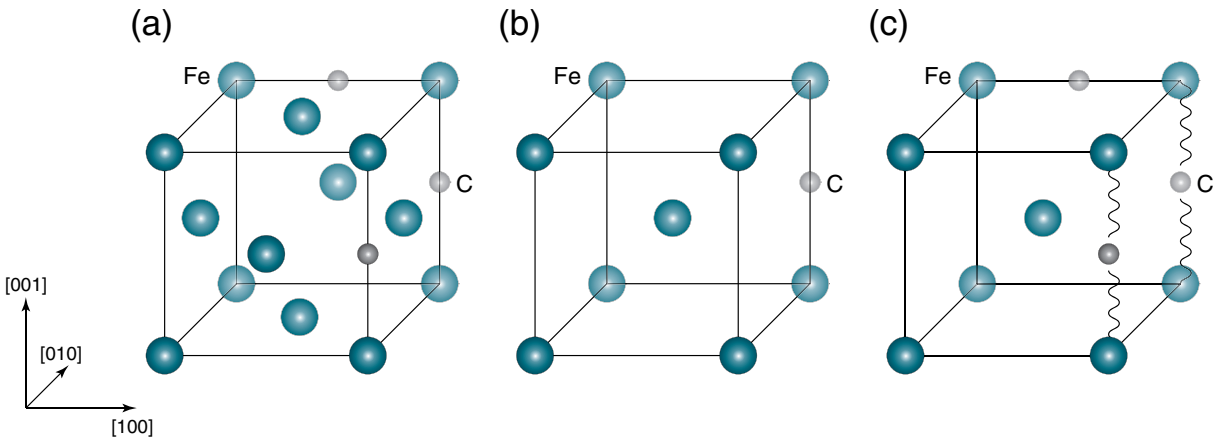

Figure 2.21: Schematics of unit cells for (a) the austenite phase, (b) the ferrite phase, and (c) the martensite phase.

similar to those of Fe. One is the austenite phase, which forms the unit cell as shown in Fig. 2.21 (a). The unit cell is a face-centered cubic lattice, in which carbon atoms are located on interstitial sites. The phase is widely used for household products, tanks for liquid natural gas, and nuclear reactors because it has high thermal and corrosion resistance. Among the austenite stainless steel, the composition of the two popular types 304 and 316 are listed in Table 2.2.

Table 2.2: The composition in % of type 304 and 316 stainless steel except Fe.

	C	Si	Mn	P	S	Ni	Cr	Mo
type 304	< 0.08	<1.00	<2.00	<0.045	<0.030	8.00~10.50	18.00~20.00	-
type 316	< 0.08	<1.00	<2.00	<0.045	<0.030	10.00~14.00	16.00~18.00	2.00~3.00

Due to the resistance for magnetization and low outgassing rate, type 304 and 316 stainless steel are often utilized for vacuum chambers. The ferrite phase has a body-centered cubic lattice with low solid solution of carbon, as shown in Fig. 2.21 (b). Kitchens and furniture usually use the phase. The martensite phase also has a body-centered cubic lattice, although a large amount of carbon exists in the lattice. The carbon distorts the lattice as shown in Fig. 2.21 (c). The phase is used for blades and shafts because of the high hardness.

2.3.4 Surfaces of stainless steel

Corrosion resistance of the stainless steel is due to the Cr_2O_3 films on the surface. In reality, however, the surface is covered by complex oxides of iron and chromium [134].

Frankenthal *et al*. showed that the depth profile of iron on Fe-Cr alloy surfaces changes as a function of temperature [135]. They have investigated the composition of the alloy surfaces with different Fe-Cr ratios using Ne and He ion sputtering. The amount of oxygen in the surface

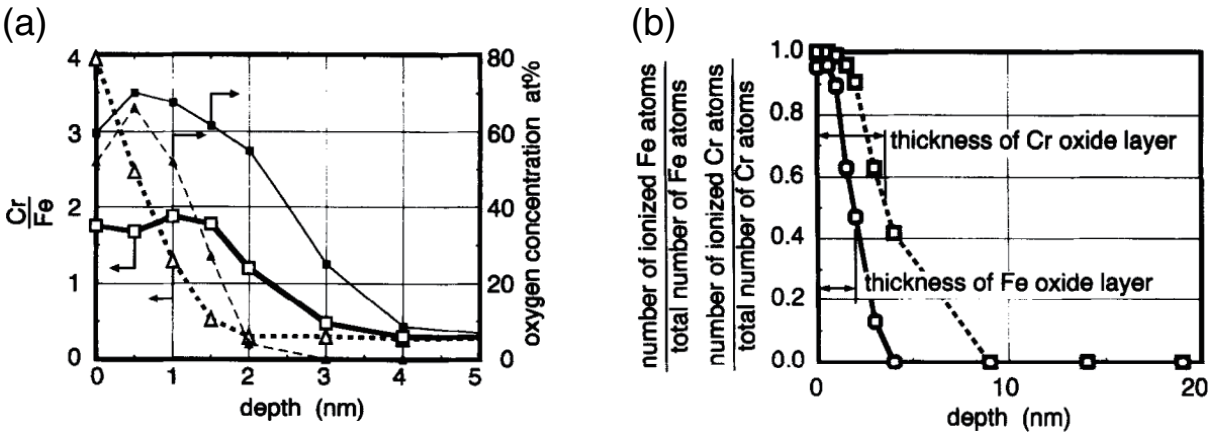

Figure 2.22: (a) The depth profile of the Cr/Fe ratio and the concentration of oxygen on a 304 type stainless steel surface. The squares and the triangles denote the Cr/Fe ratio and the concentration of oxygen. The open markers are for the sample exposed to air at room temperature after heat treatment in vacuum. The closed markers are for the sample heated in air. (b) The depth profiles of ionized Fe (open circle) and Cr (open square) divided by the number of Fe toms and Cr atoms, respectively. Reproduced from [133] with permission from Elsevier.

oxidized layer continuously decreased toward the bulk. The Cr/Fe ratio in the oxidized layer was proportional to that in the bulk and took maximum at the depth of 2.3 Å. Heat treatments of the samples decreased the Cr/Fe ratio, which became nearly 0 at 380 °C. The Cr/Fe ratio just beneath the oxide film decreased below 300 °C and increased above 300 °C.

Odaka *et al*. have measured depth profiles of the oxide film on stainless steel with X-ray photoemission spectroscopy combined with Ar ion sputtering [133]. Their sample made of type 304 stainless steel was heated at 400 °C in 10^{-4} Pa for 30 min. Then the exposure to air for 1 hour and heating at 200 °C in vacuum for 18 hours were repeated three times. After that, air was exposed to the sample for 1 hour and the chamber was evacuated. The measured Cr/Fe ratio and the concentration of oxygen as a function of the depth are plotted in Fig. 2.22 (a). The Cr/Fe ratio, which was 4 at the topmost surface, decreased as the depth increased and was in accordance with the bulk value at the depth of 2 nm. From the depth profile of the oxygen concentration, the thickness of the oxide layer was estimated to be about 3 nm. Additional heating of the sample at 200 °C in air for 3 hours and the evacuation changed the profiles, as shown in Fig. 2.22 (a). Cr diffused to around 4 nm and the degree of the oxidation increased. Figure 2.22 (b) shows the numbers of ionized metals normalized by the numbers of the metals in the sample as a function of the depth. Thickness of the iron and chromium oxides in the sample were 5 nm and 10 nm, respectively.

Water and acid treatment of stainless steel changes the part of the surface oxides into hydroxides and oxyhidroxides [136, 137, 138, 139]

Chapter 3

Single-crystal $SrTiO_3$

3.1 Control of the Surface Electronic Structure of $SrTiO_3$(001) by Modulation of the Density of Oxygen Vacancy

The influence of electron irradiation and following oxygen adsorption on the electronic and atomic structure of a $SrTiO_3$(001) surface was investigated by ultraviolet photoemission spectroscopy (UPS). Electron irradiation induced an in-gap state (IGS) as observed by UPS keeping the surface (1×1), which is considered to originate from oxygen vacancies on the topmost surface due to electron-stimulated desorption (ESD) of oxygen. Electron irradiation also caused a downward shift of the valence band maximum indicating downward band-bending and formation of a conductive layer on the surface. Adsorption of oxygen on the electron-irradiated surface, on the other hand, reduced the intensity of IGS along with upward band-bending, which points to disappearance of the conductive layer. The results show that ESD and oxygen adsorption can control the surface electronic structure switching between semiconducting and metallic regimes by changing the density of the oxygen vacancy.

3.1.1 Introduction

On $SrTiO_3$ surfaces, oxygen vacancies on the surface have an influence on the electronic properties of the surface [46, 47] and promote the interaction with gas molecules [56, 57, 140, 141], in common with other oxides [48, 49, 50]. In previous studies, oxygen vacancies have often been introduced by annealing or ion sputtering of the sample. However, annealing of $SrTiO_3$ caused a variety of surface reconstructions [142, 128, 131, 143] and ion sputtering makes the surface disordered and non-stoichiometric [56, 57, 144, 125, 145, 146].

The way to introduce oxygen vacancies on oxide surfaces without changing the crystal structure includes two methods: Epitaxial growth of thin films under a precise control of oxygen gas supply [147, 148] and electron stimulated desorption (ESD) of oxygen [149]. In the process of ESD, core-hole excitation associated with electron irradiation induces selective desorption of

atoms such as hydrogen and oxygen on the topmost layer [149, 150, 151, 59]. Oxygen ESD is of particular interest because O vacancies are expected to be formed only at the topmost layer in a controlled manner. Although ESD of oxygen on $SrTiO_3$ surfaces has been reported [23], its effects on $SrTiO_3$ atomic and electronic structures remain to be elucidated.

In the present paper, we have studied the effects of electron irradiation and subsequent oxygen adsorption on the electronic structure of the $SrTiO_3$(001) surface with ultraviolet photoemission spectroscopy (UPS) and low-energy electron diffraction (LEED). Electron irradiation induced desorption of oxygen on the topmost surface producing in-gap states keeping the surface (1×1). With increasing electron dose, the intensity of the in-gap state increased and the conduction band minimum crossed the Fermi level forming a conductive layer on the surface. Following exposure of oxygen, on the other hand, was found to reduce the in-gap state intensity. The maximum area density of surface electrons and oxygen vacancies generated by the ESD is estimated to be 1–2 $\times$ 10^{14} cm^{-2}.

3.1.2 Experimental detail

The sample used in the present study is non-doped $SrTiO_3$(001). A clean $SrTiO_3$(001) surface was prepared by heat treatment at 923 K under oxygen gas (99.999 % purity) of 6.5 $\times$ 10^{-4} Pa for 30 min. The surface is expected to be dominantly covered by the TiO_2 layer with a slight mixture of the SrO layer [126]. Then the surface was annealed in ultrahigh vacuum (UHV) at 1000 K for 10 min, which is lower than the temperature for reconstructions [126]. This process slightly introduces oxygen vacancies in the bulk, which causes electric conductivity and allows UPS measurements without charging-up. The electron density induced by annealing is $\sim10^{19}$ cm^{-3}, which is too small to be seen in UPS measurements [116]. The surface was finally exposed to oxygen of 1000 L (1 L = 1.33 $\times$ 10^{-4} Pa·s) at room temperature to compensate oxygen vacancies on the surface, which we regard as the vacancy-free surface in the present paper. Electron irradiation was performed with an electron fluid gun at an energy of 1500 eV and a sample temperature of room temperature. The electron flux was monitored by a Faraday cup. The UPS measurement was carried out with the He I line (21.22 eV) at an incidence angle of 45 $^\circ$ in the normal emission at room temperature. The typical acquisition time for a spectrum was 500 s. The flux of the light was $<$ 4.5 Jcm^{-2}, which is enough small to avoid photostimulated desorption of oxygen by the light [121].

3.1.3 Results

Figure 3.1(a) shows UPS spectra near the Fermi level (E_F) taken for vacancy-free, UHV-annealed, and electron-irradiated surfaces. For the vacancy-free surface, no particular feature was observed between E_F and -3.1 eV except background and a hump at -2.7 eV, which was ascribed to the emission due to the 23.1 eV line of He I [144]. The strong intensity below -3.1 eV corresponds to the valence band mainly due to O $2p$ of $SrTiO_3$(001). The position of the valence band maximum (E_V) was evaluated by linear extrapolation of the valence band to the zero

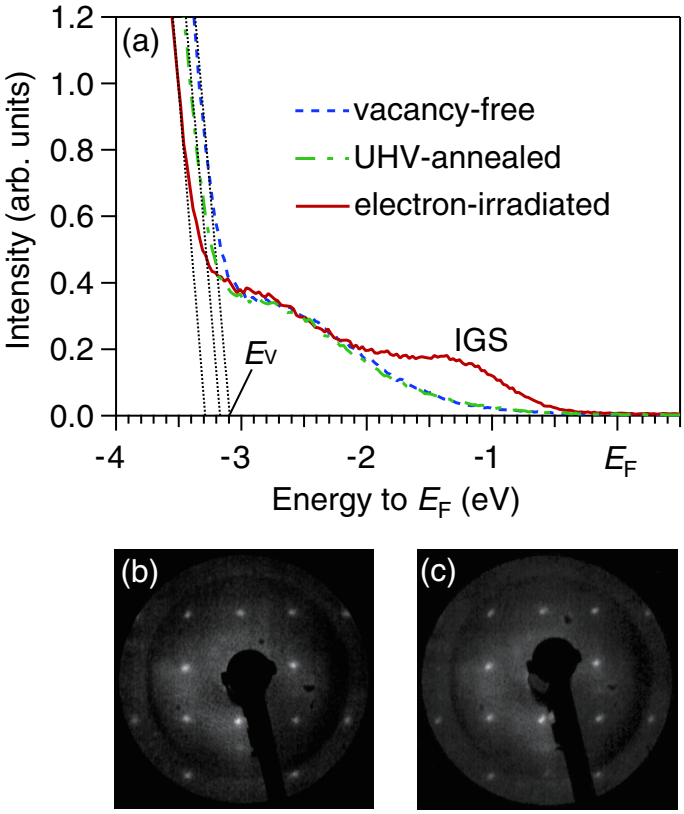

Figure 3.1: (a) Ultraviolet photoemission spectra of ultrahigh-vacuum-annealed, vacancy-free and electron-irradiated $SrTiO_3$(001) surfaces near the Fermi level (E_F) with a photon energy of 21.2 eV taken at room temperature. The energy and the amount of irradiated electrons are 1500 eV and 5×10^{18} cm^{-2}, respectively. IGS and E_V denote the in-gap state and the valence band maximum, respectively. Low-energy electron diffraction patterns of (b) the vacancy-free and (c) the electron-irradiated $SrTiO_3$(001) surfaces with an electron energy of 135 eV taken at room temperature. Reproduced from the post-print of [152].

intensity as shown in Fig. 3.1(a). After electron irradiation of 5.0×10^{18} cm^{-2}, the spectrum revealed an electronic state in the band gap at 1.3 eV below E_F. As reported for Ar-sputtered, La-doped and H-adsorbed $SrTiO_3$ surfaces [56, 115, 71], the in-gap state (IGS) derives from the electron doping into the Ti 3*d* band of $SrTiO_3$. As displayed in Fig. 3.1(a), the electron irradiation also shifts E_V toward a lower energy. As electron irradiation tends to induce oxygen ESD, the electron doping is likely to be associated with oxygen vacancies on the topmost surface in the present work. ESD induces oxygen desorption as a neutral species, which was originally O^{2-} in $SrTiO_3$(001). As a result, the two electrons in O^{2-} are transferred to the Ti 3*d* band on the surface. There have been several discussions on how the doped electrons are localized in the band gap forming IGS, such as the polaronic effect [153] and the Ti 3*d*-O 2*p* hybridization effect [154].

For the UHV-annealed surface, on the other hand, the position of E_V was shifted by −70 meV

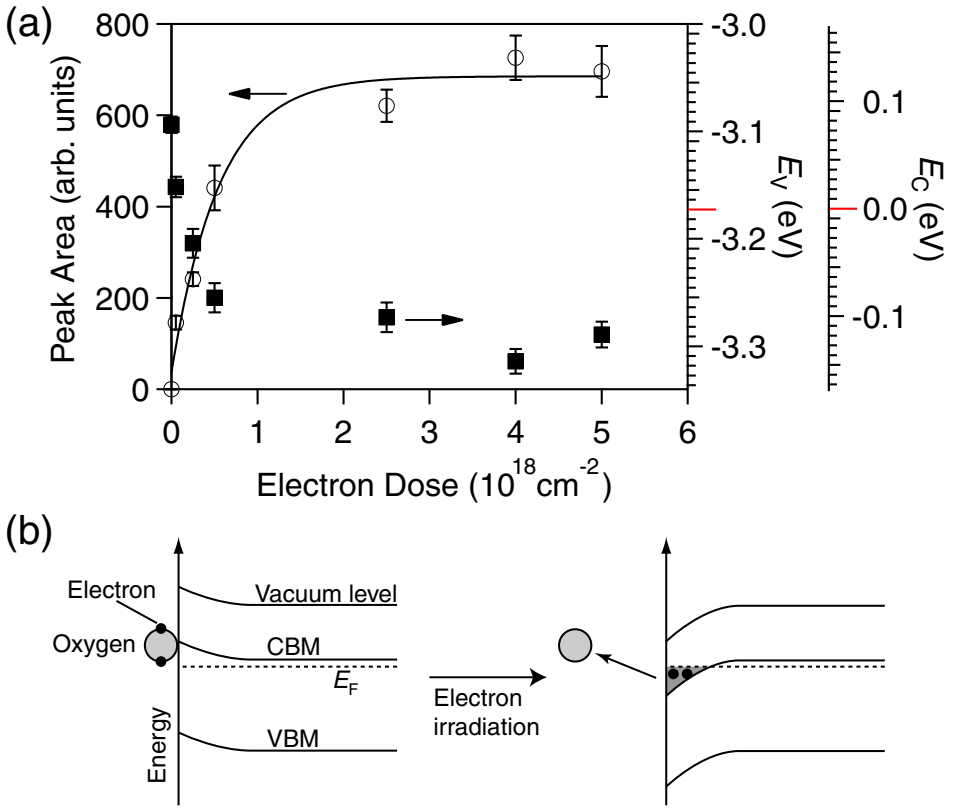

Figure 3.2: (a) Peak area of the in-gap state, positions of the valence band maximum (E_V) and conduction band minimum (E_C) on the vacancy-free $SrTiO_3$(001) surface as a function of the electron dose with an electron energy of 1500 eV. (b) A schematic of the band bending due to the electron irradiation. CBM and VBM denote the conduction band maximum and the valence band minimum, respectively. Adapted from the post-print of [152].

compared to that of the vacancy-free surface. This indicates that there occurs band bending after UHV-annealing. The reason for this band-bending is likely to be introduction of oxygen vacancy at the surface. Judging from the peak area of IGS, however, the density of the surface oxygen vacancies by the UHV annealing is lower than 1/10 of that induced by ESD. Figure 3.1(b) and (c) shows LEED patterns at a primary electron energy of 135 eV for the vacancy-free and electron-irradiated surfaces. The surface remains (1×1) with a slight increase of the background intensity after electron irradiation.

Figure 3.2(a) shows the peak area of IGS and the position of E_V as a function of the number of irradiated electrons on the vacancy-free surface. The position of the conduction band minimum (E_C) is also shown by adding the bulk band gap energy of 3.17 eV to E_V [113, 114]. The peak area increases with increasing amount of electron irradiation and saturates at about 2×10^{18} cm^{-2}. A fit with an exponential function to the experimental data gives the ESD cross section of 1.8×10^{-18} cm^2. This value is smaller than that for TiO_2 of 9×10^{-17} cm^2 [59], probably

because the chemical stability of oxygen atoms in $SrTiO_3$ is higher than that in TiO_2 [155]. The saturation density of oxygen vacancy is estimated to be $\sim 10^{14}$ cm^{-2} as discussed below, which is about 15 % of the surface oxygen density of $SrTiO_3$(001). This indicates that the electron-stimulated desorption of oxygen is quenched at a certain electron dose. The quenching of oxygen ESD is considered to be caused by neutralization of the excited hole relevant to ESD with the doped electron [59].

Next, we focus on the shift of E_V and E_C. Figure 3.2(a) also shows that the electron irradiation lowers E_V from −3.09 eV to −3.29 eV and E_C from 0.08 eV to −0.12 eV with the assumption that the band gap is 3.17 eV. This means a downward band bending near the surface, and as a result, E_C seems to cross E_F suggesting that a conductive layer is formed on the surface, as shown in Fig. (3.2)(b). The degree of the band bending is close to that caused by atomic-hydrogen adsorption on a Nb-doped $SrTiO_3$(001) surface, where a band bending of 0.2 eV was observed along with formation of a metallic state [71]. Metallic states at E_F was not observed in the present study with electron irradiation of 5×10^{-18} cm^{-2} as shown in Fig. 3.1(a). This is because the photon energy of 21.22 eV used in the present study. The metallic state appears around Γ point, which can be efficiently excited to a final state at 81 eV above E_F with a photon energy of 81 eV [71].

The electron-irradiated surface was then exposed to molecular oxygen. Figure 3.3(a) shows the peak area of IGS and the positions of E_V and E_C as a function of oxygen exposure. The dosing of oxygen reduces the peak area of IGS, which eventually becomes 0 at an oxygen exposure of ∼2.5 L. This is because neutral oxygen is either dissociatively or molecularly adsorbed at the oxygen vacancy receiving electrons from the surface. At the same time, E_V and E_C shift toward a higher energy, and E_C crosses E_F quenching the conductive layer on the surface, as shown in Fig. (3.3(b). As a result, the surface is considered to be depleted. It is noted that the positions of E_V and E_C further increase with increasing oxygen exposure from 10 to 1000 L. This result suggests that oxygen is dissociatively adsorbed on the Ti site with a small probability [156].

3.1.4 Discussion

On the assumption that the oxygen adsorption at the oxygen vacancy is a first-order reaction, the density of oxygen vacancy produced by ESD can be estimated from IGS as follows. The adsorption rate of oxygen on the surface is given by

$$\frac{d\sigma}{dt} = \frac{snv}{4\sigma_0}(\sigma_0 - \sigma), \tag{3.1}$$

where, σ is the area density of the adsorbed oxygen on the oxygen vacancy, t is time, s is the sticking probability, n is the number density of molecular oxygen in the gas phase, v is the root-mean-square velocity, σ_0 is the initial area density of the oxygen vacancy. Since the peak area of IGS is proportional to the number of doped electrons by the oxygen vacancy, a fit of the exponential function to the data in Fig. 3.3 gives $\sigma_0/s = 1.9 \times 10^{14}$ cm^{-2}. Since an oxygen

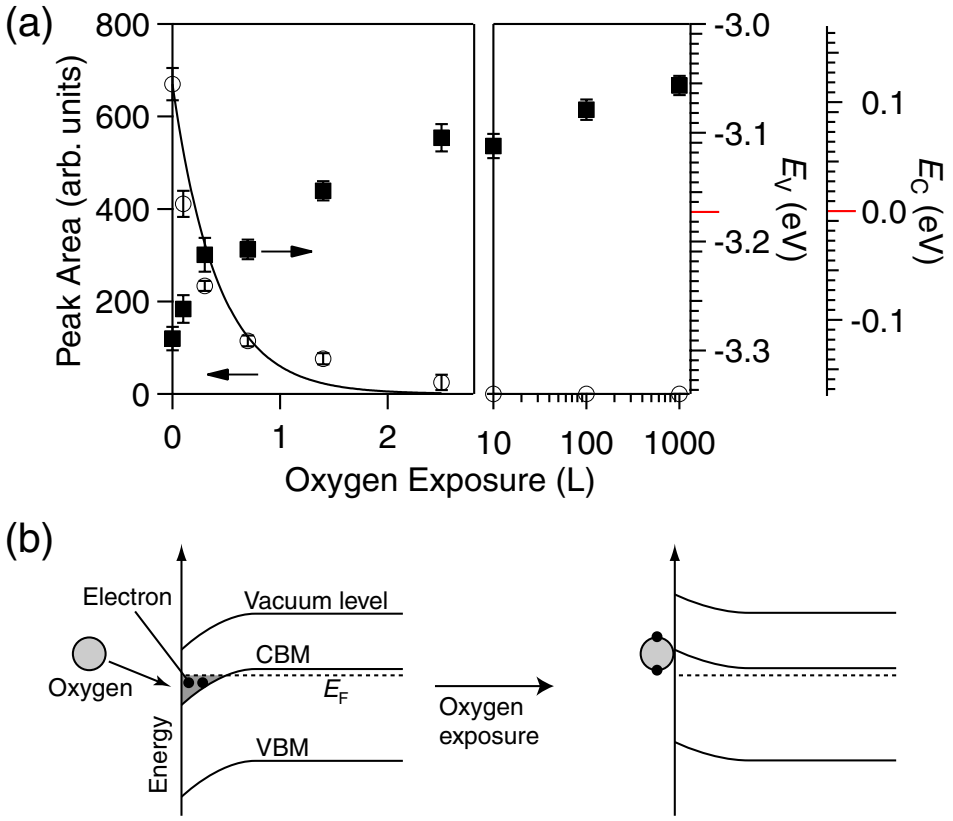

Figure 3.3: (a) Peak areas of the in-gap state, positions of the valence band maximum and conduction band minimum on the electron-irradiated $SrTiO_3$(001) surface as a function of oxygen exposure. (b) A schematic of the band bending due to the oxygen exposure. CBM and VBM denote the conduction band maximum and the valence band minimum, respectively. Adapted from the post-print of [152].

vacancy donates two electrons [54], the final area density of doped electrons on the surface by electron irradiation n_S is twice as much as σ_0 and n_S/s is estimated to be 3.8×10^{14} cm^{-2}. In the case of TiO_2, s is around 0.6 [157]. By assuming that s on $SrTiO_3$ is similar, σ_0 and n_S are estimated to be 1×10^{14} cm^{-2} and 2×10^{14} cm^{-2}, respectively.

The area density of doped electrons can also be estimated by the metallic state (MS) when E_V is located at below E_F [158, 120, 71]. We assume that the conductive layer forms MS in the present study and discuss the relation between MS and IGS. Fig. 3.2 (a) indicates that the electron doping started to grow IGS without the appearance of MS, as schematically shown in Fig. 3.4 (a). Then, when E_V crossed E_F, MS appeared and started to grow. This means that the growth of IGS is independent of that of MS. In other words, both of the states reflect the amount of doped electrons independently.

Therefore, based on the values of n_S estimated from MS in the previous works [158, 120], we evaluate n_S in the present study without using the peak area of IGS but with using the band bending. In the Wedge model, the bent band is expressed by a triangle well as shown in Fig.

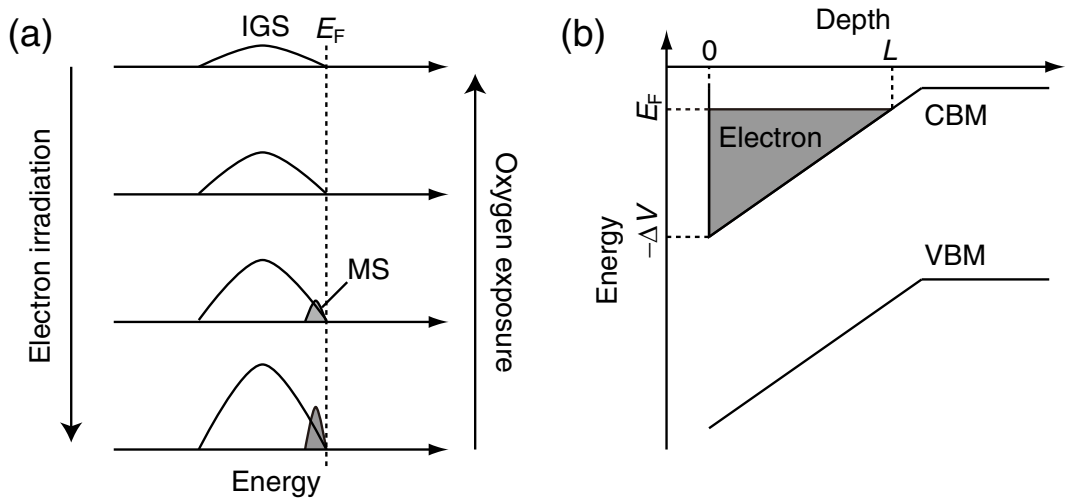

Figure 3.4: (a) A schematic of the relation between an in-gap state (IGS) and a metallic state (MS) as a function of the change of the doped electrons by the electron irradiation and the oxygen exposure. (b) A schematic of the Wedge model. CBM and VBM denote the conduction band maximum and the valence band minimum, respectively.

3.4 (b). The band bending ΔV is given by

$$\Delta V = eFL, \tag{3.2}$$

where e is the elementary charge, F is the electric field, and L is the depth of the triangle well. The homogeneous volume density of doped electrons N_S represents n_S as

$$n_S = \frac{N_S L}{2}. \tag{3.3}$$

Combining Eqs. (3.2) and (3.3) yields

$$n_S = \frac{N_S}{2eF}\Delta V. \tag{3.4}$$

Santander-Syro *et al*. estimated that n_S, L, and F were 1.5×10^{14} cm^{-2}, ~15 Å, and 8.3×10^7 Vm^{-1}, respectively [120]. Substituting the values of n_S and L into Eq. (3.3) gives N_S of 2×10^{21} cm^{-3}. Then substituting the F and the N_S into Eq. (3.4) yields the relation between ΔV (eV) and n_S (cm^{-2}) as

$$n_{S(\text{Santander–Syro})} = 1.2 \times 10^{15}\Delta V. \tag{3.5}$$

On the other hand, Aiura *et al*. have obtained ΔV, N_S, and L of 0.2 eV, 8.4×10^{20} cm^{-3}, and 70 Å , respectively [158]. Substituting the values of ΔV and the L into Eq. (3.2) gives F of 2.9×10^7 Vm^{-1}. Eq. (3.4) is transformed into

$$n_{S(\text{Aiura})} = 1.5 \times 10^{15}\Delta V. \tag{3.6}$$

Finally, substituting the band bending of 0.20 eV obtained by Fig. 3.2 into Eqs. (3.5) and (3.6) yields n_S of 2.4×10^{14} and 3.0×10^{14} cm^{-2}, respectively, which are well consistent with the value of 2×10^{14} cm^{-2} estimated from the IGS change by the oxygen adsorption.

3.1.5 Conclusion

In conclusion, the effects of electron irradiation and oxygen exposure on the electronic and atomic structure of $SrTiO_3$(001) were investigated by UPS and LEED. While electron irradiation induces an in-gap state due to oxygen ESD on the topmost surface, the vacancy-free surface is restored by molecular-oxygen dosage. Electron irradiation also induces downward band-banding, which seems to result in formation of a conductive layer in the surface. This allows us to control the area density of the oxygen vacancy at the surface thereby enabling us to switch the surface between semiconducting and metallic regimes. As a future prospect, it will be possible to fabricate a nanoscale metallic structure with a desired electron density by locally producing oxygen vacancies with focused electrons.

3.2 Two Charged States of Hydrogen on the $SrTiO_3$(001) Surface

The effects of hydrogen exposure on the electronic structure of two types of $SrTiO_3$(001) surfaces, oxygen-deficient (OD) and nearly-vacancy-free (NVF) surfaces, were investigated with ultraviolet photoemission spectroscopy and nuclear reaction analysis. Upon molecular hydrogen exposure to the OD surface which reveals in-gap states at 1.3 eV below the Fermi level, the in-gap state intensity was reduced to half the initial value at a hydrogen coverage of $0.9 \pm 0.7 \times 10^{14}$ cm^{-2}. On the NVF surface which has no in-gap state, on the other hand, atomic-hydrogen exposure induced in-gap states, and the hydrogen saturation coverage was evaluated to be $3.1 \pm 0.8 \times 10^{14}$ cm^{-2}. We argue that H is positively charged as $H^{\sim 0.3+}$ on the NVF surface by being coordinated to the O atom, whereas H is negatively charged as H^- on the OD surface by occupying the oxygen vacancy site. The stability of H^- at the oxygen vacancy site is discussed.

3.2.1 Introduction

The behavior of hydrogen on the $SrTiO_3$ surface is of particular interest, because molecular hydrogen is formed as a result of photolysis of water [27, 118] and the surface is metalized by adsorption of atomic hydrogen [71, 72]. The adsorbed hydrogen on the surface forms an O-H bond [70, 72], which has also been observed in the stoichiometric bulk[159, 160]. Although hydrogen is possibly adsorbed to cations in addition to oxygen, such hydrogen-cation complexes have not been identified on the $SrTiO_3$ surface to date. With further exposure of the sample to hydrogen, it is naively expected that oxides are reduced producing oxygen vacancies. While annealing of a (Ba,Sr)TiO_3 film in D_2/N_2 forming gas induced a substantial increase in the leakage current [161], annealing of $SrTiO_3$ in hydrogen atomosphere incorporated hydrogen in the bulk without making O-H bonds and removed the electrons doped by oxygen vacancies [160]. The results suggest that an oxygen vacancy is possibly occupied by hydrogen forming a vacancy-hydrogen complex with hydrogen negatively charged, which is shown to be stable by a recent theoretical study [162]. The possible presence of the hydride anion at the oxygen-vacancy site has been experimentally reported for other oxides such as MgO [73, 74], $12CaO{\cdot}7Al_2O_3$ [76], and $BaTiO_3$ [78], and theoretically predicted for ZnO [75, 79], MgO [75], TiO_2 [80], and $BaTiO_3$.[77].

A previous photoemission studies have shown that the in-gap state due to electron doping into the Ti 3*d* state on a $SrTiO_3$(111) surface reduced by annealing in H_2 atmosphere, ion bombardment, and post annealing decreases upon H_2 dosage [57, 163]. Although hydrogen interaction with oxygen vacancies on $SrTiO_3$ is of interest and importance, the study was conducted on a disordered surface [57, 163], and the detailed investigateion remained to be done. The moti-

vation behind the present study is thus to clarify the interaction of hydrogen and concomitant charge transfer with the $SrTiO_3$ surfaces with and without oxygen vacancies. We have investigated the effects of hydrogen exposure on the electronic structure of the OD and NVF surfaces of $SrTiO_3$(001) with ultraviolet photoemission spectroscopy (UPS). Molecular hydrogen exposure to the OD surface reduced surface electrons as probed by the in-gap state intensity induced by oxygen vacancies in contrast to the NVF surface where atomic hydrogen exposure increased the in-gap state intensity. Since the knowledge of the hydrogen density on the surface is indispensable for accurate estimation of the charged state of hydrogen, we applied H-specific ^{1}H(^{15}N, $\alpha\gamma$)^{12}C nuclear reaction analysis (NRA) to quantify the surface hydrogen coverage on the surfaces. The increase of the hydrogen coverage of the NVF surface and the OD surface was quantitatively evaluated to be $3.1 \pm 0.8 \times 10^{14}$ cm^{-2} and $0.9 \pm 0.7 \times 10^{14}$ cm^{-2}, respectively. In combination of the UPS and NRA results, the charged state of adsorbed hydrogen and its stability are discussed.

3.2.2 Experimental detail

A clean $SrTiO_3$(001) surface was prepared by heat treatment at 923 K under 6.5×10^{-4} Pa of oxygen gas (99.999 % purity) for 30 min. The surface is expected to be dominantly covered by the TiO_2 layer with a slight mixture of the SrO layer [126]. Then the surface was annealed in ultrahigh vacuum (UHV) at 1000 K for 10 min, which is lower than the temperature for reconstructions [126]. This process introduces oxygen vacancies in the bulk, which causes electric conductivity and allows UPS measurements without charging-up. The density of the oxygen vacancy on the surface induced by annealing is $<<10^{13}$ cm^{-2} [152], which we regard as an NVF surface. Low-energy electron diffraction (LEED) of the NVF surface showed a (1×1) pattern. An OD $SrTiO_3$(001) surface was prepared by electron irradiation on the NVF surface, which causes ESD of oxygen with the surface kept at (1×1) [152]. Electron irradiation of 5×10^{18} cm^{-2} was performed at an energy of 1500 eV and a sample temperature of room temperature. The area density of the produced oxygen vacancy was estimated to be $\sim 1 \times 10^{14}$ cm^{-2} [152], as shown in Sect. 3.1.

H_2 gas (99.999 % purity) was purified by a palladium membrane heated at 400 °C and introduced into the UHV chamber. Atomic hydrogen was produced by passing the purified H_2 gas in a tungsten tube heated at 1900 K. As the dissociation probability in the tungsten tube is not known, mixture of H and H_2 was supplied to the surface. In the present experiments, the $SrTiO_3$(001) surface was exposed to either molecular H_2 or mixture of H+H_2 at room temperature.

The surface electronic structure was investigated by using UPS with the He I line (21.22 eV) at an incident angle of 45 ° in normal emission at room temperature. The absolute amount of hydrogen and its depth profile were investigated by NRA at the 1E beam line of the 5 MV Van de Graaff Tandem accelerator in the Microanalysis Laboratory (MALT) of The University of Tokyo [164]. The $^{15}N^{2+}$ ion beam irradiated the surface at a current of 40–100 nA and a beam

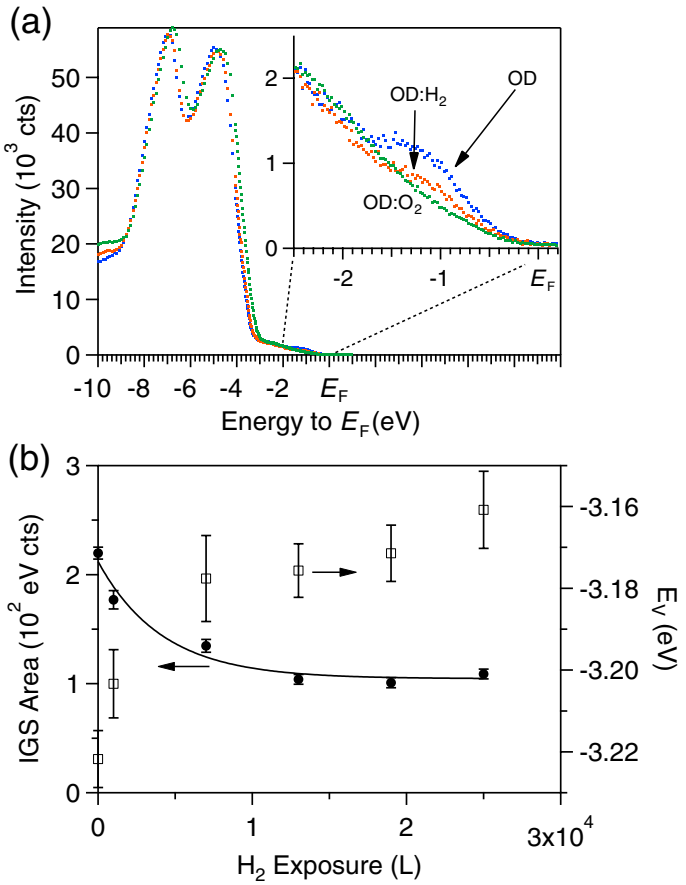

Figure 3.5: (a) Ultraviolet photoemission spectra taken at room temperature for the oxygen-deficient (OD) $SrTiO_3$(001) surface (blue), the OD surface exposed to H_2 of 2.5×10^4 L (OD:H_2, red) and the OD surface exposed to O_2 of 10 L (OD:O_2, green) with a photon energy of 21.22 eV. (b) The peak area of the in-gap state (IGS) and the position of the valence band maximum (E_V) on the OD surface as a function of the H_2 exposure. The mark on the ordinate axis indicated by OD denotes the IGS area for the OD surface. Reproduced from the post-print of [166].

diameter of 2–4 mm on the surface at room temperature. The stopping power (dE/dz) of 2.67 keV/nm for $SrTiO_3$ [165] defines the probing depth.

3.2.3 Results

Figure 3.5 (a) shows the change in the UPS spectrum near the Fermi level (E_F) upon O_2 exposure (OD:O_2) and H_2 exposure (OD:H_2) on the OD surface. For the OD surface, an electronic state is observed at −1.3 eV in the band gap (IGS), which is caused by oxygen vacancies on the topmost surface due to electron stimulated desorption [152]. As reported for Ar-sputtered [56], La-doped [115], and H-adsorbed $SrTiO_3$ surfaces [71], IGS derives from the electron doping into the Ti 3*d* band of $SrTiO_3$. Although the real cause for the IGS is not yet clarified [153, 154],

the IGS intensity is used as an index of the surface electron density in the present study.

As shown in Fig. 3.5 (a), O_2 exposure of 10 L on the OD surface completely removes the IGS. At the same time, the position of the valence band maximum (E_V) is shifted to a higher energy. The energy shift is estimated to be 0.2 eV by evaluating the E_V position after linear extrapolation of the valence band spectrum to zero intensity. After H_2 exposure of 2.5×10^4 L (1 L = 1.33×10^{-4} Pa·s) on the OD surface, the peak area of the IGS also decreased. The peak area of the IGS and E_V as a function of H_2 exposure are shown in the Fig. 3.5 (b). The H_2 exposure reduces the peak area of the IGS to a half of the initial value. It appears that the electrons in the IGS induced by oxygen vacancies are transferred to adsorbed hydrogen. Furthermore, the work function change due to H_2 exposure was estimated to be −0.1 eV from the shift of the cut-off energy of the secondary electron. Along with these changes, E_V was also shifted from −3.22 eV to −3.16 eV. From the E_V value, the position of the conduction band minimum (E_C) is estimated by assming the band-gap energy of 3.17 eV, which suggests a shift of E_C from −0.05 eV to 0.01 eV. This indicates that the band is upward bent and that E_C crosses E_F suppressing the conductive layer originating from the surface oxygen vacancy. It is noted that a metallic state is not observed in the UPS spectrum of Fig. 3.5 (a) although E_C is expected to lie below E_F for the OD surface. This is because of the photon energy of 21.22 eV used in the present study. The metallic state appears around the Γ point, which can be efficiently excited to a final state at 81 eV above E_F with a photon energy of 81 eV [71].

Figure 3.6 (a) demonstrates the UPS spectra near E_F for the NVF surface before and after a $H+H_2$ exposure of 9×10^3 L (NVF:$H+H_2$) along with the spectrum of the OD surface. Whereas the spectrum revealed no change with H_2 exposure to the NVF surface, a significant increase of IGS was recognized after $H+H_2$ exposure. The peak area of IGS and E_V as a function of the $H+H_2$ exposure are shown in Fig. 3.6 (b). The peak area increased with increasing $H+H_2$ exposure and saturated at about 3×10^3 L. The peak area at saturation was 44 % of that of the OD surface. At the same time, the $H+H_2$ exposure lowered E_V from −3.12 eV to −3.17 eV and induced a work function change of −0.3 eV. With the $H+H_2$ exposure, furthermore, a small feature developed at −10.5 eV, which is consistent with the previous study [72] and attributed to the O-H bond [167], implying that hydrogen was adsorbed on the oxygen atom. These results indicate electron transfer from hydrogen to the surface. The decrease of the work function is considered to be caused by the electric dipole moment at the O-H bond. Note that E_C is estimated to change from 0.05 to 0 eV from the change of E_V on the assumption of the band gap of 3.17 eV.

The NRA profiles measured for the NVF, NVF:H_2, NVF:$H+H_2$ and OD:H_2 surfaces are shown in Fig. 3.7. The surfaces were exposed to either H_2 or $H+H_2$ of $5 \times 10^4 \sim 1 \times 10^5$ L, where the change of the IGS intensity saturated. All profiles reveal a maximum at the resonance energy indicating that H is present at the surface. The solid curves in the figure are fits with a Gaussian function of the form $A\exp(-(E_i - E_0)^2/w^2)$, where A, E_0, and w are fit parameters. We measured the NRA profiles two or three times for each surface to confirm that the data were reproducible within the experimental accuracy. For all profiles in Fig. 3.7, E_0 was equal to

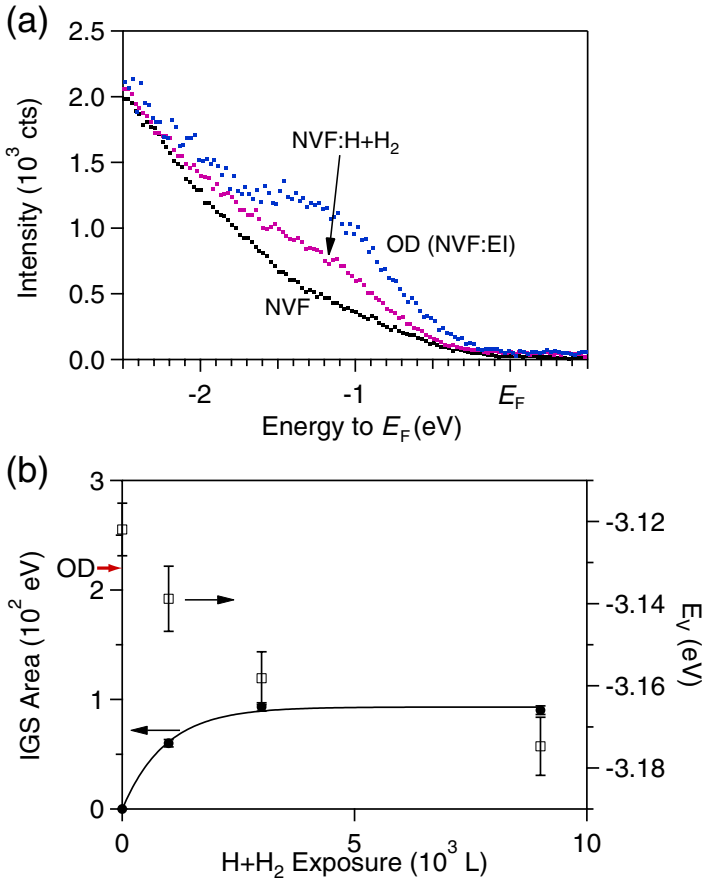

Figure 3.6: (a) Ultraviolet photoemission spectra taken at room temperature for the nearly-vacancy-free (NVF, black) $SrTiO_3$(001) surface, the NVF surface exposed to H+H_2 of 9×10^3 L (NVF:H+H_2, red) and the OD surface (blue) at a photon energy of 21.22 eV near the Fermi level (E_F). (b) The peak area of the in-gap state (IGS) and the position of the valence band maximum (E_V) as a function of the H+H_2 exposure. The peak area of IGS for the OD surface is marked on the left axis. Reproduced from the post-print of [166].

the resonance energy within the uncertainty, and w was 9.4 ± 0.15 keV reflecting the Doppler width due to the zero-point vibration [99]. Table 3.1 shows the area density of hydrogen on the surfaces estimated from the fit values.

For the NVF surface, σ_H is $(2.2 \pm 0.4) \times 10^{14}$ cm^{-2} even without hydrogen exposure. The observed signal might originate from hydrogen trapped at defect sites due to background gas adsorption, although the origin remains to be elucidated. The amount of hydrogen adsorbed on the surface due to hydrogen exposure is therefore estimated by subtracting the σ_H value for the NVF surface from those obtained after hydrogen exposure, which is shown in Table 3.1 as $\Delta\sigma_H$. As the hydrogen density due to the H_2 exposure to the NVF surface seems to be negligible within the experimental uncertainty, H_2 is not adsorbed on $SrTiO_3$ without oxygen vacancies. This result is in agreement with that the UPS spectrum of the NVF surface showed no change

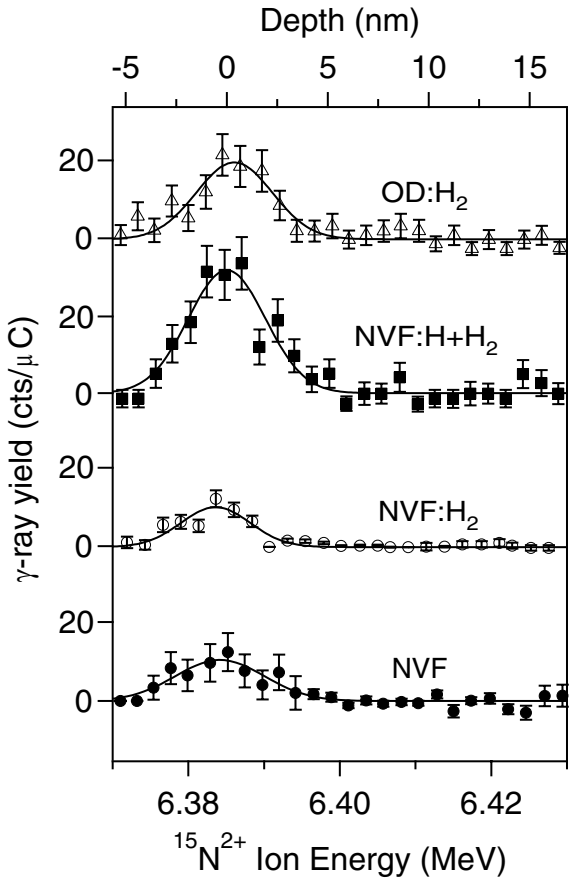

Figure 3.7: $^1H(^{15}N, \alpha\gamma)^{12}C$ nuclear reaction profiles taken at room temperature for the nearly-vacancy-free (NVF) $SrTiO_3$(001) surface, the NVF surface exposed to H_2 (NVF:H_2), the NVF surface exposed to H+H_2 (NVF:H+H_2) and the oxygen-deficient $SrTiO_3$(001) surface exposed to H_2 (OD:H_2). Reproduced from the post-print of [166].

by H_2 exposure. On the other hand, $\Delta\sigma_H$ is $(3.1 \pm 0.8) \times 10^{14}$ cm^{-2} with the H+H_2 exposure to the NVF surface, which corresponds to the situation where 0.47 hydrogen adsorbs in the surface unit cell of TiO_2. Yukawa *et al.* estimated the H coverage as $0.8 \sim 1.1 \times 10^{14}$ cm^{-2} from the O 1s photoemission analysis [72], which is smaller than the present result. This might be because the H dosage did not reach the saturation in their work or O 1s analysis underestimated the H coverage. For the OD:H_2 surface, the $\Delta\sigma_H$ value coincides with the oxygen vacancy density of $\sim 1 \times 10^{14}$ cm^{-2} due to electron irradiation [152], although the uncertainty is large. The results suggest that a hydrogen atom adsorbs at the oxygen vacancy site.

Table 3.1: The area density of hydrogen σ_H evaluated from the NRA profiles for the nearly-vacancy-free (NVF) surface, the NVF surface exposed to H_2 of 5×10^4 L (NVF:H_2), the NVF surface exposed to H+H_2 of $1{\times}10^5$ L (NVF:H+H_2) and the oxygen-deficient surface exposed to H_2 of 1×10^5 L (OD:H_2). $\Delta\sigma_H$ denotes the difference of σ_H from that of NVF.

Surface	σ_H (10^{14} cm^{-2})	$\Delta\sigma_H$ (10^{14} cm^{-2})
NVF	2.2 ± 0.4	-
NVF:H_2	2.0 ± 0.5	−0.2 ± 0.6
NVF:H+H_2	5.3 ± 0.7	3.1 ± 0.8
OD:H_2	3.1 ± 0.7	0.9 ± 0.7

3.2.4 Discussion

Charged state of adsorbed hydrogen

We first discuss the origin of the IGS due to the H+H_2 exposure. On the NVF surface, there is a possibility that atomic hydrogen abstracts the oxygen atom at the surface as a water molecule, which leads to formation of the oxygen vacancy on the surface. However, oxygen abstraction by atomic hydrogen is induced only above 500 K in the case of TiO_2 [168]. The calculated formation energy of the oxygen vacancies in TiO_2 and $SrTiO_3$ is 4.44 eV [169], and 5.45 eV [170], respectively, which indicates oxygen atoms are more stable in $SrTiO_3$ than in TiO_2. On these bases, the abstraction of oxygen atoms by atomic hydrogen at room temperature is not likely to occur on the $SrTiO_3$ surface. We therefore argue that the IGS observed in Fig. 3.6 is induced by hydrogen adsorbed on oxygen at the surface. We evaluate the area density of electrons donated to the surface from the IGS intensity. The IGS intensity on the OD surface shown in Fig. 3.5 corresponds to the surface electron with an area density of $\sim 2 \times 10^{14}$ cm^{-2} evaluated in Sect. 3.1 [152]. On the assumption that the IGS intensity is proportional to the surface electron density in IGS, comparison of the IGS intensity of the NVF:H+H_2 surface with that of the OD surface gives the areal electron density of 0.8×10^{14} cm^{-2} on the NVF:H+H_2 surface. This value is similar to the electron density of 0.6×10^{14} cm^{-2} estimated from the Fermi wavevector of the metallic state in previous work [71]. Since the amount of the adsorbed hydrogen on this surface is $\sim 3.1 \times 10^{14}$ cm^{-2}, a hydrogen atom is estimated to donate ~ 0.3 electron to the surface as $H^{\sim 0.3+}$. This electron transfer leads to formation of a dipole layer on the surface. We assume that the O–H bond length is 0.1 nm, the permittivity changes from the vacuum value of ϵ_0 to that of $SrTiO_3$ ($\sim 300\epsilon_0$ [171]) at the middle of the O–H, and the charge of hydrogen uniformly distributes from the top to the half of the O–H bond. Then, the potential difference in this layer is evaluated to be −0.4 V, which is in rough agreement with the workfunction change of −0.3 eV.

For the OD:H_2 surface, the adsorbed hydrogen reduces the IGS intensity to half the initial value. Since the H coverage is similar to the oxygen vacancy density, one hydrogen atom seems

to adsorb on the oxygen vacancy on the surface. This appears to indicate that one hydrogen receives one electron from the OD surface and the hydrogen exists in the H^- state.

Stability of H^- at an oxygen vacancy site

Previous experimental studies claimed that H^- is present at the oxygen site in bulk oxides [73, 74, 76, 78]. It is also theoretically shown that oxygen vacancies are stably occupied by hydrogen as H^- in TiO_2, $BaTiO_3$ and $SrTiO_3$ [80, 77, 162]. It is suggested that the Madelung energy is dominant for stabilization of H^-. We discuss in the following the stability of H^- around the oxygen vacancy on the $SrTiO_3(001)$ surface. We first consider the energy required for the H^- formation on $SrTiO_3$:

$$SrTiO_3 + \frac{1}{2}H_2 \rightarrow SrTiO_3^+ + H^-, \tag{3.7}$$

whose energy diagram is shown in Fig. (3.8)(a). The dissociation energy of H_2 and the electron affinity of H are 2.3 eV/H [172], and 0.8 eV [172], respectively. The ionization energy of $SrTiO_3$ is assumed to be the sum of the work function (5.1 eV) [173] and the energy of the IGS from E_F (1.3 eV). As a result, the energy required for the above reaction becomes 7.9 eV. The energy gain due to adsorption of H^- on $SrTiO_3^+$ mainly originates from the electrostatic potential energy between H^- and the ions in $SrTiO_3^+$, because H^- is a closed-shell ion [174]. Then, the total energy for H^- adsorption on $SrTiO_3$ is given by the difference between the electrostatic potential and the H^- formation energy.

We calculate the electrostatic potential energy as a sum of the Madelung energy and the repulsive energy between the electron orbital of H^- and $SrTiO_3(001)^+$ with a surface oxygen vacancy. The atomic structure of the surface is schematically shown in Fig. 3.8 (b), and the electrostatic potential was calculated by varying the H^- position. One extra electron charge due to the IGS was assumed to be shared by the nine Ti atoms around the oxygen vacancy on the top layer. Figure 3.8 (c) shows a contour plot of the Madelung energy as a function of the H^- position calculated with the Ewald method,[175] which represents a local maximum of -19.5 eV at the oxygen vacancy site along the [100] direction. This is because of the attractive interaction from the neighboring Ti ions. Along the [010] and [001] directions, on the other hand, the Madelung energy shows a minimum at the oxygen vacancy site, which means the oxygen vacancy site is a saddle point for the Madelung energy.

The repulsive energy U is assumed to be the Born-Mayer type function given by $U = a\exp(-d/b)$, where d is the distance between the centers of ions and a and b are the Born-Mayer parameters for each pair of ions. The Born-Mayer parameters are adjusted with the measured H^- radii as follows. The Born-Mayer parameters for O^{2-} with each ion in $SrTiO_3$ are given by Prade *et al.* as shown in Table 3.2 [176].

We obtain the parameters for H^- by adjusting the parameters for O^{2-} following the procedure proposed by Catlow and Fender [177]. First, the parameter b's for O^{2-} can be commonly used for H^-. Next, the parameter a's for H^- are given by multiplying a for O^{2-} by a scaling factor $\exp[(r_{H^-} - r_{O^{2-}})/b]$, where $r_{O^{2-}}$ and r_{H^-} are the ionic radii of O^{2-} and H^-, respectively. We used

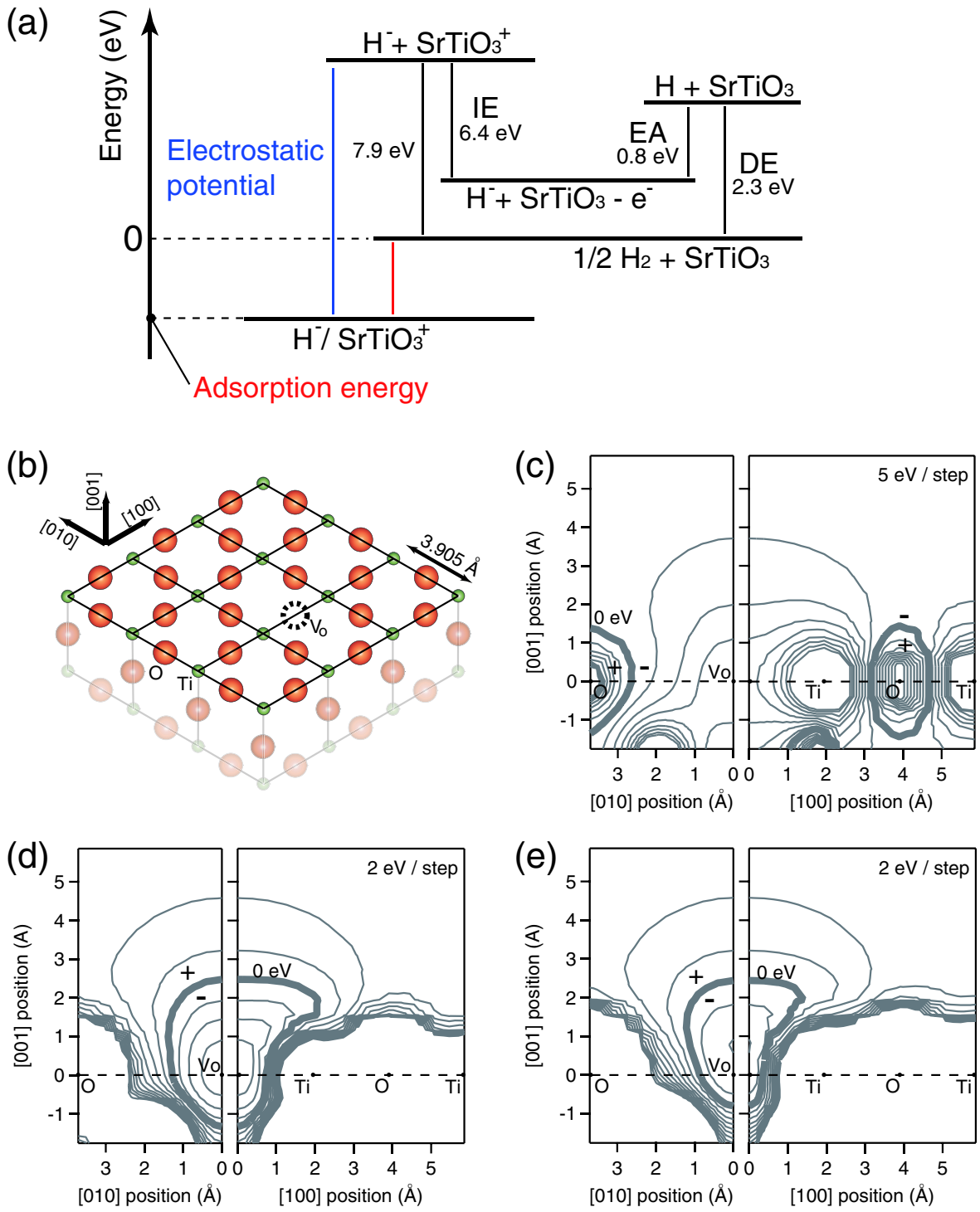

Figure 3.8: (a) An energy diagram for the H^- formation on $SrTiO_3$. IE, EA, and DE denote the ionization energy of $SrTiO_3$, the electron affinity of H, and the dissociation energy of H_2, respectively. (b) A schematic of the $SrTiO_3$(001) surface with an oxygen vacancy (V_o). (c) A contour plot of the Madelung energy for H^- around an oxygen vacancy (V_o). Contour plots of the total energy around V_o for H^- with H^- radii of (d) 1.25 Å and (e) 1.46 Å. Adapted from the post-print of [166].

Table 3.2: Born-Mayer parameteres for $SrTiO_3$ given by Prade *et al*. [176].

	a (eV)	*b* (Å)
Sr^{2+}-O^{2-}	3864	0.2831
Ti^{4+}-O^{2-}	1083	0.3340
O^{2-}-O^{2-}	99829	0.1786

Table 3.3: *a* for various r_{H^-} on $SrTiO_3$.

r_{H^-} (Å)	*a* (eV)		
	Sr-H	Ti-H	O-H
1.25	2275	691	43097
1.46	4776	1296	139695

$r_{O^{2-}}$ of 1.40 Å, which is almost independent of the environment [178]. For r_{H^-}, on the other hand, the value distributes from 1.2 to 1.6 Å, depending on the environment [179]. Table 3.3 shows *a*'s for H^- with r_{H^-} of 1.25 and 1.46 Å, which are the values in TiH_2, NdH_2, LiH, and NaH, respectively.

Figure 3.8 (d) and (e) shows the total energy profiles for H^- with radii of 1.25 and 1.46 Å, respectively, which correspond to the radii measured for TiH_2 and NaH, respectively.[179] Most of the H^- radius measured for other materials are between 1.25 and 1.46 Å.[179] Although the actual H^- radius is not known, the total energy takes positive values on Ti and O atoms, which prohibit adsorption of H^- on these sites. Although a Ti atom has a positive charge of 4+, which stabilizes H^-, two O^{2-}'s next to the Ti atom weaken the positive electrostatic potential. Then the electric repulsive energy between the Ti and H^- reduces the gain of the electronstatic potential, and the total energy becomes positive on the Ti atom. On the other hand, the total energy reveals a negative value only around the oxygen vacancy site. It is worth emphasizing that the total energy takes a minimum in all directions for any radii of H^- at the oxygen vacancy site. This indicates that H^- can stably adsorb only at the oxygen vacancy site on $SrTiO_3$(001) due to the large gain of the electrostatic potential energy.

3.2.5 Conclusion

We have studied the electronic structure of the H-adsorbed $SrTiO_3$(001) surfaces. Whereas the in-gap state due to oxygen vacancies was partially removed by H on the oxygen-deficient $SrTiO_3$(001), H adsorption induced in-gap states on the nearly-vacancy-free $SrTiO_3$(001). By taking account of the absolute H coverage and the in-gap state intensity, we argued that hydrogen is positively and negatively charged on the nearly-vacancy-free and oxygen-deficient surfaces, respectively, revealing an amphoteric character. The charged state was estimated as

$H^{\sim 0.3+}$ and H^{-}, respectively. Furthermore, this work will contribute to the elucidation of the hydrogen dynamics in hydrogen sensing by oxide-based sensors and the hydrogen formation reaction in water photolysis on oxide surfaces, all of which are essential to the use of hydrogen as an energy source.

3.3 Rotational and Nuclear-Spin State Transition of Hydrogen in Scattering on $SrTiO_3$(001) Surfaces with and without Oxygen Vacancies.

In this section, we have studied the distribution of the rotational states of molecular hydrogen scattered from the $SrTiO_3$(001) surfaces with and without oxygen vacancies using the molecular hydrogen beam and the state-selective detection introduced in Chap. 2. The ratio of the ortho and para hydrogen in the incident beam and scattered hydrogen was estimated from the rotational distribution. The probability of the ortho-para conversion in the scattering process was estimated to be 0.15 ± 0.05 and 0.28 ± 0.05 for the surface without and with oxygen vacancies, respectively. The magnetic properties of the surface oxygen vacancies are discussed on the basis of the change in the rotational distribution.

3.3.1 Introduction

Molecular hydrogen exists in two nuclear-spin isomers, ortho-hydrogen and para-hydrogen. Due to the symmetry of the total wave function with respect to the permutation of the two nuclei, ortho-hydrogen having the total nuclear spin $I = 1$ is in the rotational state with odd rotational quantum number J, while para-hydrogen of $I = 0$ has even J. The population of each rotational state is determined by the Boltzmann distribution. The conversion between ortho and para states is so slow in the gas phase with a conversion time of the order of 10^{20} s. On the other hand, the ortho-para conversion can be promoted on surfaces. The main mechanisms are interaction with localized spins, virtual electron transfer, and surface electric field, as explained in Chap. 1. In addition to them, ortho-para conversion in dynamic adsorption processes was also reported [180, 181]. However, the mechanism remains to be elucidated.

In the present study, we use the $SrTiO_3$(001) surface as a sample, because $SrTiO_3$ has high controllability of the surface electronic structure as shown in Chap. 3. Annealing in oxygen atmosphere keeps the surface insulating. On the other hand, annealing in ultra high vacuum induces oxygen vacancies in the bulk, which dope electrons. As a result, the bulk becomes semiconducting. In addition, electron irradiation causes electron stimulated desorption of oxygen and creates surface oxygen vacancies, which results in further electron doping at the surface.

Impurities such as oxygen vacancies in oxides can have localized spins. Theoretical works have predicted the existence of localized spins on oxygen vacancies in TiO_2 [80] and hydrogen atoms adsorbed on ZnO [182]. These localized spins are, however, paramagnetism because of the low density. Due to the limited availability of detection of the paramagnetic spin at surfaces, the magnetic character of the localized states at oxide surfaces is yet to be clarified.

With these in mind, the aim of the study is to confirm the existence or non-existence of a localized spin in the defect such as oxygen vacancies by using ortho-para conversion which is

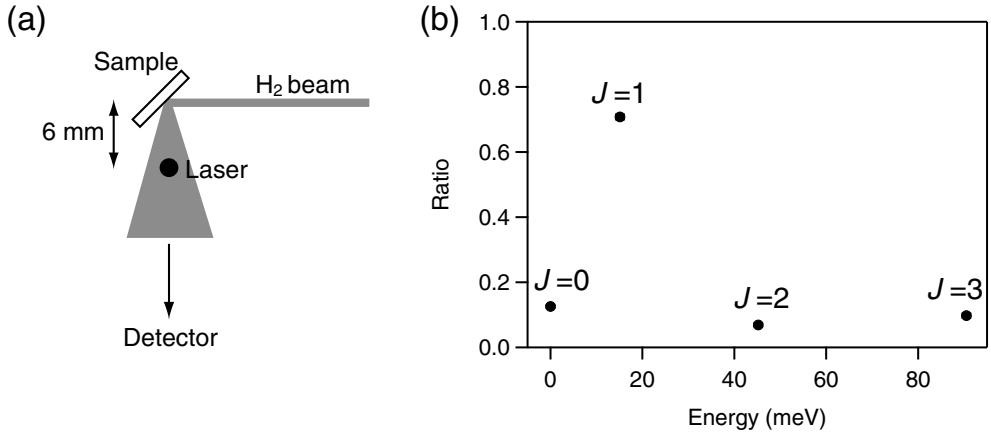

Figure 3.9: (a) A schematic of the experimental setup. (b) The ratio of rotational states of H_2 in H_2 beam used in the present study.

sensitive to magnetic dipole moments. The other aim includes the elucidation of the mechanism in ortho-para conversion in dynamic processes. Control of the atomic and electronic structure of a surface is effective for the latter aim to specify the factor which promotes the conversion.

In this chapter, we have investigated the rotational and nuclear-spin states transition of H_2 on electron-density-controlled $SrTiO_3$(001) in a scattering regime using the system explained in Chap. 2 which we have constructed.

3.3.2 Experimental detail

The sample used in the present study is non-doped $SrTiO_3$(001). A clean and insulating surface (O_2 annealed surface) was prepared by heat treatment at 923 K under oxygen gas (99.999 % purity) of 6.5×10^{-4} Pa for 30 min. Annealing the insulating surface at 1000 K in UHV for 30 min produced a semiconducting surface (UHV annealed surface), in which carriers are doped by the generation of oxygen vacancies in the bulk. The magnitude of the amount of the carrier density was $\sim 10^{19}$ cm^{-3}.

The experimental setup is schematically shown in Fig. 3.9(a). The samples were exposed to the H_2 beam with the system explained in Chap. 2. The flux of the beam was evaluated to be 3×10^{15} cm^{-2}s^{-1}. The incident angle of the beam to the samples was 45 °. The incident and scattered beam is state-selectively detected by REMPI via the E, F $^1\sum_g^+$ states. The scattered beam was measured at 6.0 mm from the samples. The intensity of $J = 0 \sim 3$ states was normalized to the correction factors obtained with the intensity in a gas phase of H_2. The ratio of $J = 0 \sim 3$ states in the beam is shown in Figure 3.9. A Boltzmann plot of the populations in Fig. 3.9(b) gave a rotational temperature of 308 ± 42 K. $I_{J=1,3}/I_{J=0,2}$ ratio in the beam was 4.1, which is an overestimate compared to the theoretical value of 3.0 at room temperature.

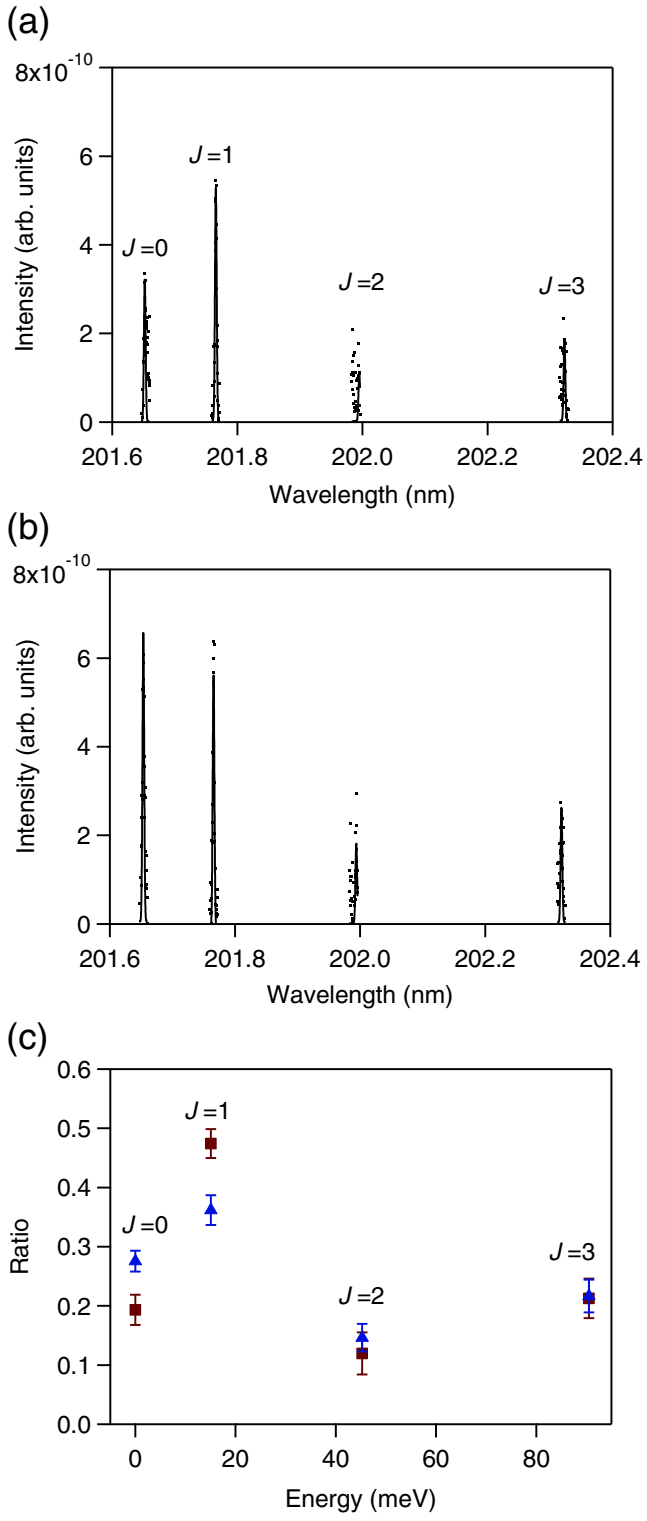

Figure 3.10: REMPI spectra of H_2 scattered from (a) O_2 annealed and (b) UHV annealed $SrTiO_3$(001) surfaces. (c) The ratio of rotational states of H_2 scattered from the O_2 annealed (closed square) and the UHV annealed (closed triangle) surfaces.

3.3.3 Results

Figure 3.10 (a) and (b) shows REMPI spectra of H_2 scattered from the O_2 annealed and UHV annealed $SrTiO_3$(001) surfaces, respectively. Fitting with gaussian to the spectra gives the intensity of each rotational state. The intensity was compared with that of gas-phase H_2 for normalization. The ratio of rotational states for the O_2 annealed and UHV annealed surfaces is shown in Fig. 3.10 (c). $I_{J=1,3}/I_{J=0,2}$ ratio of H_2 scattered from the O_2 annealed and UHV annealed surfaces was estimated to be 2.2 ± 0.3 and 1.4 ± 0.2, respectively. The change in the ratio suggests that the scattering induced the ortho-para conversion of H_2. Furthermore, the conversion rate on the UHV-annealed surface is larger than that on the O_2 annealed surface.

3.3.4 Discussion

With an assumption that the total amount of $J = 0 \sim 3$ states is conserved during the scattering, the difference of the intensity of each state between the incident beam and the scattered H_2 was calculated as shown in Fig. 3.11 (a). Figure 3.11 (a) shows that the scattering on both of the O_2 annealed and UHV-annealed surfaces decreased the intensity of the $J = 1$ state and increased the intensity of the $J = 0, 2, 3$ states. We focus on the transition between the ortho and para states. The probability of the ortho-para conversion P_{op} is defined to be

$$P_{\mathrm{op}} = \frac{\Delta I_1 + \Delta I_3}{I_1^i + I_3^i}, \tag{3.8}$$

where $I_{J'}^i$ is the intensity of the initial state with a rotational quantum number of J' and $\Delta I_{J'}$ is the change in the intensity for the $J = J'$ state. In the case of the scattering experiment, the initial and final states correspond to the H_2 in the beam and the scattered H_2, respectively. P_{op} for H_2 scattered on the O_2-annealed and the UHV-annealed surfaces is calculated to be 0.15 ± 0.05 and 0.28 ± 0.05, respectively. This suggests that the ortho-para conversion was induced in the scattering process.

We focus on the promotion of P_{op} by the UHV annealing. Promotion of P_{op} was also reported on the O_2-coadsorbed Ag(111) surface. Figure 3.11 (b) shows P_{op} in the adsorption process on the O_2 adsorbed Ag(111) surface as a function of the area density of the adsorbed O_2. The increase in P_{op} is approximately proportional to the area density of O_2, which has been attributed to the magnetic moment of O_2. The corresponding area density of Bohr magnetons on the O_2-adsorbed Ag(111) surface and normalized P_{op} compared to P_{op} on a clean surface are also plotted on the top and the right axis, respectively. If the promotion of the ortho-para conversion on the UHV-annealed surface is due to the magnetic moment on the oxygen vacancies on the surface, the area density of the magnetic moment is deduced from Fig. 3.11 (b). The UHV-annealing increased the P_{op} up to 1.9 ± 0.7 times as large as that for the O_2 annealed surface. By comparing the promotion rate with those in Fig. 3.11 (b), the intensity of the magnetic moment is deduced to be an area density of $1.7 \pm 1.4 \times 10^{13}$ cm^{-2}. The UHV annealed surface contains oxygen vacancies of $\sim 10^{19}$ cm^{-3} in the bulk [116], whose area density on the surface

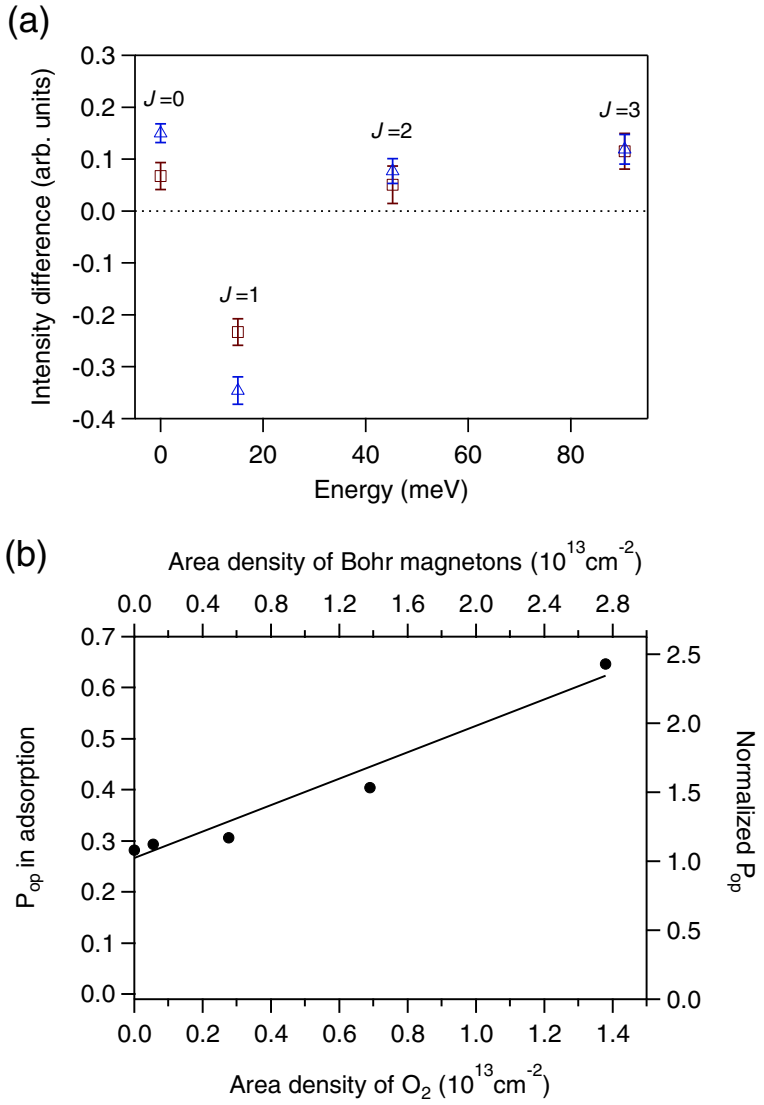

Figure 3.11: (a) Differences of the intensity of $J = 0 \sim 3$ states between the incident H_2 beam and H_2 scattered from the O_2 annealed (open square) and the UHV annealed (open triangle) $SrTiO_3$(001) surfaces. (b) P_{op} as a function of the coverage of molecular oxygen on a Ag(111) surface at 6.8 K [180]. The corresponding area density of Bohr magnetons and the normalized P_{op} with respect to P_{op} on clean Ag(111) surface are plotted on the top and the right axis, respectively.

is $\sim 10^{13}$ cm^{-2}. The coincidence between the order of the calculated area density of the dipole moment and the area density of the oxygen vacancies suggests that the oxygen vacancies possess localized spins.

The present work showed the ortho-para conversion occur in a scattering process. Ortho-para conversion in dynamic processes has been observed on surfaces such as Ag(111) and solid ice [36, 181]. In addition to the ortho-para conversion in physisorbed states, the adsorption process in which H_2 transitions from an unbound state in a gas phase to physisorbed states also promoted the ortho-para conversion. In the experiments on Ag(111), H_2 in a gas phase at room temperature is exposed to Ag(111) at a temperature of 6.8 K. Immediately after the adsorption, $J = 1/J = 0$ was found to be 1.1, which means that the adsorption process induced ortho-para conversion. On the Ag(111) surface at 6.8 K, the rotational states of H_2 are only in the $J = 0$ and $J = 1$ states because of the low temperature. Therefore, Eq. (3.8) estimates P_{op} in the adsorption process as 0.3. The adsorption process consists of the approach of H_2 to a surface and the relaxation of H_2 in a potential well of the physisorbed state.

In the former process, the time scale in which H_2 is influenced by fields on a surface is $\sim 10^{-13}$ s because the space distribution of the surface field is $\sim 10^{-10}$ m and the velocity of H_2 is $\sim 10^3$ m/s. The latter relaxation process is determined by the vibration of H_2 whose time scale is $\sim 10^{-12}$ s [183, 184]. On the other hand, the time scale of the scattering of H_2 is $\sim 10^{-13}$ s as in the approach process in physisorption. Because the time scale for H_2-surface interaction is comparable to that for physisorption, it is no wonder that the ortho-para conversion occurs in the scattering process.

In the present work, the rotational temperature of the incident H_2 beam was in accordance with room temperature and the sample was also at room temperature. Therefore, the rotational temperature of the scattered H_2 averaged with respect to all the trajectories must be identical to room temperature. The observed ortho-para conversion is considered to occur in specific trajectories, which are achieved by the experimental setup in the present study. As a future plan, it is desirable that all the trajectories will be investigated.

3.3.5 Summary

The intensity of the $J = 0 \sim 3$ states of H_2 scattered from the O_2 annealed and the UHV annealed $SrTiO_3$(001) surfaces has been measured with REMPI. Probability of the o-p conversion in the scattering process were estimated to be 0.15 ± 0.05 and 0.28 ± 0.05 for the O_2 annealed and the UHV annealed surfaces, respectively. The promotion of the conversion by oxygen vacancies on the UHV annealed surface was discussed to be derived from localized spin on the oxygen vacancies.

Chapter 4

Inhomogeneous metal oxide

4.1 Analytical Formula for Calculating Adsorption Density of States on Chamber Surfaces from Measured Pressure Change

Pressure decay during an evacuation process of a vacuum chamber often shows a power-law dependence on time, which is considered to reflect the distribution of the adsorption energy of particles on the surface of the chamber. We derive an analytical formula that directly transforms the pressure change into the adsorption density of states. This method shows that the power-law behavior is equivalent to the situation in which the chamber surface has a constant- or exponential-type adsorption density of states for particles under a quasi-static condition.

4.1.1 Introduction

In an evacuation process, gas particles are desorbed from the chamber surface with a finite residence time. In order to explain the power-law decay, the adsorption energy of particles is assumed to be distributed in a certain range revealing the variation of the residence time. The distribution of the adsorption energy is called the adsorption density of states (ADOS). In the framework of the adsorption model, Horikoshi has numerically shown the power-law decay of the pressure by employing the constant (Temkin-type) and the exponential (Freundlich-type) ADOS [95]. Further, assuming a quasi-static equilibrium in which the rate of adsorption balances with the rate of desorption, the power-law decay was derived on the assumption of the Temkin-type [185, 186, 96, 187, 188, 189] and the Freundlich-type [185, 186, 96, 187] ADOS. Ha *et al*. introduced the Fermi-Dirac function to describe the occupancy of the adsorption site with a specific energy, and discussed the power-law decay [190]. Despite much effort, however, the physics behind the power-law decay remains to be elucidated. This is because previous studies only showed that the Freundlich (Temkin)-type ADOS is a necessary condition for the evacuation curve with a power-law decay. Furthermore, the applicable condition of the quasi-static equilibrium used in the studies has not been strictly discussed, as shown in Sect. 4.1.3.

In this section, we derive an analytical formula to transform the pressure change into a unique form of ADOS on the surface of chambers under the quasi-static equilibrium condition. In the elicitation process, the applicable condition of the quasi-static equilibrium is rigorously derived. This method shows that the Freundlich (Temkin)-type ADOS is the necessary and sufficient condition for the evacuation curve with a power-law decay under the quasi-static equilibrium. This method also enables us to analyze evacuation curves with arbitrary shapes, which has not been realized in previous studies.

In Sect. 4.1.2, we will obtain the formula to transform the pressure change into ADOS based on the rate equation for adsorption-desorption and the balance of the number of particles. In Sect. 4.1.3, we will obtain ADOS from the pressure change showing a power-law decay. We also derive the applicable condition of the quasi-static solution and show the concept of deriving ADOS from the change in pressure, compared with the measurement of the electronic density of states. Finally, Sect. 4.1.4 contains a summary and concluding remarks.

4.1.2 Derivation of analytical formula of ADOS

Description of number of particles in a chamber and differential equations

The number of particles in a chamber $M(t)$ is given by

$$M(t) = Vn(t) + A\sigma(t), \tag{4.1}$$

where $n(t)$ is the number density of particles in the gas phase, $\sigma(t)$ is the area density of adsorbed particles on the surface of the chamber, V is the volume of the chamber, and A is the surface area of the chamber. $M(t)$ changes as a function of time, because particles are evacuated with a pump from the chamber. The differentiation of Eq. (4.1) results in

$$\frac{dM(t)}{dt} = V\frac{dn(t)}{dt} + A\frac{d\sigma(t)}{dt}. \tag{4.2}$$

In the case of the evacuation of a vacuum chamber, Eq. (4.2) is called the evacuation equation. During an evacuation process, $n(t)$ and $dM(t)/dt$ are experimentally obtained. While a pressure gauge measures $n(t)$, a pump with a known pumping speed gives $dM(t)/dt$.

$\sigma(t)$ is given by integrating the occupancy of a single adsorbed state $\theta(E,t)$ and the adsorption density of states $g_a(E)$ with respect to the adsorption energy E as follows:

$$\sigma(t) = \int_{-\infty}^{0} g_a(E)\theta(E,t)dE. \tag{4.3}$$

$g_a(E)dE$ gives the site density in the energy range $E \sim E + dE$ and is normalized as

$$\sigma_0 = \int_{-\infty}^{0} g_a(E)dE, \tag{4.4}$$

where σ_0 is the area density of all adsorption sites.

We let $k_a(E)$ and $k_d(E)$ be the reaction rate constants of adsorption and desorption, respectively. Then, the reaction rate of adsorption and desorption on one site with E is given by

$$\begin{aligned}\frac{d(g_a(E)\theta(E,t))}{dt} &= k_a(E)n(t)g_a(E)\{1-\theta(E,t)\} \\ &- k_d(E)g_a(E)\theta(E,t). \end{aligned} \tag{4.5}$$

Next, a known $n(t)$ gives the exact solution of Eq. (4.5):

$$\begin{aligned}\theta(E,t) &= e^{-\left(\int^t k_a n(t')dt' + k_d t\right)}\left[R\right. \\ &+ \left.\int^t k_a n(t') e^{\left(\int^{t'} k_a n(t'')dt'' + k_d t'\right)} dt'\right], \end{aligned} \tag{4.6}$$

where R is an integral constant determined by the initial condition. Thus, Eq. (4.2) becomes a homogeneous Fredholm integral equation of the first kind [191] written as

$$\int_{-\infty}^{0} g_a(E)\frac{\partial\theta(E,t)}{\partial t}dE = \frac{1}{A}\frac{dM(t)}{dt} - \frac{V}{A}\frac{dn(t)}{dt}. \tag{4.7}$$

With known $dM(t)/dt$ and $n(t)$, we can derive $g_a(E)$. However, a homogeneous Fredholm equation of the first kind is difficult to solve, except in special cases, since it contains a definite integral and nonlinear terms [191]. Therefore, transformation of the equation is considered in Sect's. 4.1.2-4.1.2.

Applicable condition of quasi-static equilibrium for θ

We define a constant $N(E)$ as $N(E) \equiv k_d/k_a$, and express $n^*(E,t)$ as $n^*(E,t) \equiv n(t)/N(E)$. The time scale of the pressure change in which θ changes from ~1 to ~0 is designated as $T(E)$, and $t^*(E)$ is expressed as $t^*(E) \equiv t/T(E)$. We additionally define $\tau(E) \equiv 1/k_d(E) = 1/k_a(E)N(E)$. By the use of these expressions, Eq. (4.5) is rewritten as

$$\epsilon\frac{\partial\theta}{\partial t^*} = -\theta + n^*(1-\theta), \tag{4.8}$$

$$\epsilon(E) \equiv \frac{\tau(E)}{T(E)}. \tag{4.9}$$

With the above definitions, n^* and t^* are dimensionless, and the order of magnitude of $\partial\theta/\partial t^*$, θ, n^*, and $(1-\theta)$ becomes $o(1)$.

Here, θ is expanded in a series of ϵ:

$$\theta = \theta_0 + \epsilon\theta_1 + \epsilon^2\theta_2 + \cdots. \tag{4.10}$$

In Eq. (4.10), θ_0 is a good approximate solution when $\epsilon\theta_1/\theta_0$, $\epsilon^2\theta_2/\theta_0 \cdots << 1$. When $\epsilon << 1$,

in particular, $\epsilon\theta_1/\theta_0 << 1$ is a representative condition for θ_0 to be a good approximate solution. We evaluate the condition as follows. Substituting Eq. (4.10) into Eq. (4.8) gives

$$\epsilon\frac{\partial}{\partial t^*}(\theta_0 + \cdots) = -(\theta_0 + \epsilon\theta_1 + \cdots) + n^*(1 - \theta_0 - \epsilon\theta_1 - \cdots). \tag{4.11}$$

Equation (4.11) is an identity expressed as a series of ϵ. The requirement that each coefficient is identical to 0 yields

$$\epsilon^0 \quad : \quad 0 = -\theta_0 + n^*(1 - \theta_0), \tag{4.12}$$

$$\epsilon^1 \quad : \quad \frac{\partial\theta_0}{\partial t^*} = -(1 + n^*)\theta_1. \tag{4.13}$$

Solving Eqs. (4.12) and (4.13) gives

$$\theta_0 = \frac{n^*}{n^* + 1}, \tag{4.14}$$

$$\theta_1 = -\frac{dn^*}{dt^*}\frac{1}{(n^* + 1)^3}. \tag{4.15}$$

Equation (4.14) is equivalent to the Langmuir adsorption equation. Combining Eqs. (4.14) and (4.15), the condition $\epsilon\theta_1/\theta_0 << 1$ is expressed as

$$\left|\frac{\epsilon\theta_1}{\theta_0}\right| = \left|\epsilon\frac{1}{n^*}\frac{dn^*}{dt^*}\frac{1}{(n^* + 1)^2}\right| << 1. \tag{4.16}$$

The meaning of Eq. (4.16) is discussed in Sect. 4.1.3. When Eq. (4.16) holds, θ is approximated by θ_0, which is the solution of Eq. (4.12). Since the first and second terms of the right-hand side of Eq. (4.8) are the velocities of desorption and adsorption, respectively, Eq. (4.12) means that the velocity of adsorption is balanced with that of desorption. This corresponds to a quasi-static equilibrium between gas particles and adsorbed particles on the surface. Equation (4.16) is quantitatively evaluated for $n(t)$ of the power-law decay in Sect. 4.1.3.

Approximate solution of θ

Assuming the condition of Eq. (4.16), we express $\theta_0(E, t)$ with the chemical potential of gas. Here, the internal degrees of freedom of particles are ignored, and the partition functions of a bare site and an adsorption state are considered to be equal to 1. The partition function of particles in gas phase Q_g is described by the three-dimensional translational partition function of ideal gas as follows [193, 194]:

$$Q_g = Vq_g, \quad q_g = \left(\frac{m}{2\pi\hbar^2\beta}\right)^{\frac{3}{2}}, \tag{4.17}$$

where q_g is the three-dimensional translational partition function of ideal gas per volume of gas particles and m is the mass of a particle. When adsorption and desorption are balanced, k_d/k_a is

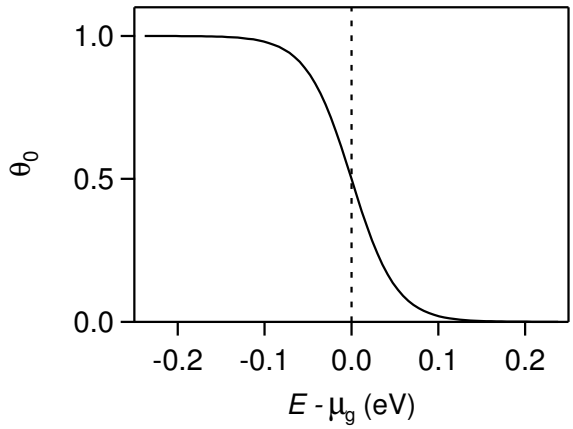

Figure 4.1: θ_0 as a function of $E - \mu_g$. Reproduced from the post-print of [192].

given by

$$\frac{k_d}{k_a} (= N) = q_g e^{\beta E}. \tag{4.18}$$

The chemical potential of ideal gas μ_g is, on the other hand, given by (see Appendix 4.1.5)

$$\mu_g(t) = \frac{1}{\beta} \ln \left[\frac{n(t)}{q_g} \right]. \tag{4.19}$$

With Eqs. (4.18) and (4.19), $n^*(E,t)(= n(t)/N(E))$ is rewritten as

$$n^* = \exp[-\beta\{E - \mu_g(t)\}]. \tag{4.20}$$

Substituting Eq. (4.20) into Eq. (4.14) yields

$$\theta_0(E,t) = \frac{1}{e^{\beta\{E-\mu_g(t)\}} + 1}. \tag{4.21}$$

θ_0 in Eq. (4.21) is the Fermi-Dirac function, which originates from the statistical property in which only one particle occupies one adsorption state. Figure 4.1 shows θ_0 as a function of $(E - \mu_g)$. When E of an adsorption state is sufficiently smaller than μ_g at a given time, the state is occupied. In contrast, the state is unoccupied when E is sufficiently larger than μ_g.

Expansion of the integral equation

Substituting Eqs. (4.19) and (4.21) into Eq. (4.7) yields

$$\frac{d\mu_g}{dt} \frac{\partial}{\partial \mu_g} \int_{-\infty}^{0} g_a(E) \frac{1}{e^{\beta(E-\mu_g)} + 1} dE = \frac{1}{A} \frac{dM(t)}{dt} - \frac{\beta V q_g}{A} e^{\beta \mu_g} \frac{\partial \mu_g}{\partial t}. \tag{4.22}$$

Since $n(t)$ changes as a function of time and μ_g is related to n as described by Eq. (4.19), μ_g is

a function of t, which we describe as $\mu_g = f(t)$. Since n changes monotonially, t is inversely expressed as a function of μ_g as $t = f^{-1}(\mu_g)$. Rearrangement of eq. (4.22) gives

$$\frac{\partial}{\partial \mu_g} \int_{-\infty}^{0} g_a(E) \frac{1}{e^{\beta(E-\mu_g)}+1} dE = F(\mu_g) \tag{4.23}$$

$$F(\mu_g) \equiv \frac{(dM/dt)}{A\left(d\mu_g/dt\right)} - \frac{\beta V q_g}{A} e^{\beta \mu_g}. \tag{4.24}$$

In eq. (4.24), μ_g and dM/dt are measured quantities in an evacuation process, and thus $F(\mu_g)$ is a known quantity. An asymptotic expansion (the Sommerfeld expansion) of the left-hand side of eq. (4.23) is given by [195]

$$\begin{aligned} &\frac{\partial}{\partial \mu_g} \int_{-\infty}^{0} g_a(E)\theta_0(E,\mu_g) dE \\ &= \frac{\partial}{\partial \mu_g} \left[\int_{-\infty}^{\mu_g} g_a(E) dE + \sum_{i=1}^{\infty} \frac{a_i}{\beta^{2i}} \frac{d^{2i-1}}{dE^{2i-1}} g_a(E)|_{E=\mu_g} \right] \\ &= \sum_{i=0}^{\infty} \frac{a_i}{\beta^{2i}} \frac{d^{2i}}{d\mu_g^{2i}} g_a(\mu_g), \\ &a_i \equiv 2\left(1 - \frac{1}{2^{2i}} + \frac{1}{3^{2i}} - \frac{1}{4^{2i}} + \cdots\right). \end{aligned} \tag{4.25}$$

Substituting Eq. (4.25) into Eq. (4.23) and replacing μ_g with E yields

$$\sum_{i=0}^{\infty} \frac{a_i}{\beta^{2i}} \frac{d^{2i}}{dE^{2i}} g_a(E) = F(E), \tag{4.26}$$

where $F(E)$ is a known function as described by Eq. (4.24). In Eq. (4.26), $g_a(E)$ becomes equal to $F(E)$ if only the term with $i = 0$ is considered. The terms with $i > 0$ form a differential equation, which is solved in Sect. 4.1.2.

Solution of the differential equation

$g_a(E)$ satisfies a boundary condition

$$g_a(E) = 0 \ (E < E_{min}, E > E_{max}), \tag{4.27}$$

where E_{min} and E_{max} are constants. Solving Eq. (4.26) under Eq. (4.27) gives the solution of $g_a(E)$ as (see Appendix 4.1.5 for details),

$$g_a(E) \quad = \quad \sum_{j=0}^{\infty} b_{2j} F^{(2j)}(E)$$

$$= F(E) - \frac{\pi^2}{6\beta^2}F^{(2)}(E) + \frac{\pi^4}{120\beta^4}F^{(4)}(E) + \cdots, \tag{4.28}$$

where j is an integer and $F^{(2j)}(E)$ denotes $d^{(2j)}F/dE^{(2j)}$.

Summarizing this section, a change in $n(t)$ is replaced by a change in μ_g following Eq. (4.19), and $g_a(E)$ is expressed by Eqs. (4.28) and (4.26) under the condition of Eq. (4.16).

4.1.3 Discussion

Derivation of $g_a(E)$ from $P-t$ curves with power-law shapes

It is experimentally known that the pressure change during an evacuation process in a molecular-flow region often takes the form of

$$P(t)\left(=\frac{1}{\beta}n(t)\right) = \alpha t^{-\gamma}, \tag{4.29}$$

with constants α and $\gamma(\sim 1)$ [196, 189, 190]. In this section, $g_a(E)$ derived from Eq. (4.29) is discussed. The applicable condition of the quasi-static equilibrium for Eq. (4.29) is evaluated in Sect. 4.1.3.

Substituting Eq. (4.29) into Eq. (4.19) gives

$$\mu_g(t) = f(t) = \frac{1}{\beta}\ln\left(\frac{\beta\alpha}{q_g}t^{-\gamma}\right), \tag{4.30}$$

$$\frac{d\mu_g}{dt} = -\frac{\gamma}{\beta}\left(\frac{q_g}{\beta\alpha}\right)^{1/\gamma} e^{\beta\frac{1}{\gamma}\mu_g}, \tag{4.31}$$

and

$$t = f^{-1}(\mu_g) = \left(\frac{\beta\alpha}{q_g}\right)^{\frac{1}{\gamma}} e^{-\frac{\beta}{\gamma}\mu_g}. \tag{4.32}$$

In an evacuation process, dM/dt represents the pumping speed, which takes the form of

$$\frac{dM}{dt} = -a\tilde{v}n(t), \tag{4.33}$$

where a is the area of the pumping orifice with an ideal pump and $\tilde{v}$ is one-quarter of the root-mean-square velocity of gas particles [197]. Substituting Eq. (4.19) into Eq. (4.33) yields

$$\frac{dM(t)}{dt} = -a\tilde{v}q_g e^{\beta\mu_g}. \tag{4.34}$$

Then, substituting Eqs. (4.31) and (4.34) into Eq. (4.24) and replacing μ_g by E give

$$F(E) = Ce^{\beta\left(1-\frac{1}{\gamma}\right)E} - De^{\beta E}$$

$$\begin{aligned} C &\equiv \frac{a\tilde{\nu}\beta q_g}{A\gamma}\left(\frac{\beta\alpha}{q_g}\right)^{\frac{1}{\gamma}} \\ D &\equiv \frac{\beta q_g V}{A}. \end{aligned} \tag{4.35}$$

We finally obtain $g_a(E)$ from Eq. (4.28),

$$\begin{aligned} g_a(E) &= C\left[1-\frac{\pi^2}{6}\left(1-\frac{1}{\gamma}\right)^2+\cdots\right]e^{\beta\left(1-\frac{1}{\gamma}\right)E} \\ &- D\left[1-\frac{\pi^2}{6}+\cdots\right]e^{\beta E}. \end{aligned} \tag{4.36}$$

Here, the second term on the right-hand side of Eq. (4.36) is negligible compared with the first term when

$$\begin{aligned} Ce^{\beta\left(1-\frac{1}{\gamma}\right)E} &>> De^{\beta E} \\ \Leftrightarrow E &< \frac{\gamma}{\beta}\ln\left[\frac{a\tilde{\nu}}{\gamma V}\left(\frac{\beta\alpha}{q_g}\right)^{1/\gamma}\right]. \end{aligned} \tag{4.37}$$

In a typical system where $a/V = 0.02$ (m^{-1}) [95], $\alpha = 1$ (Pa· s^{γ}), $\gamma = 1$ [196, 198], and the temperature is 300 K, Eq. (4.37) is written as $E < -0.69$ eV. Under the condition of Eq. (4.37), $g_a(E)$ shows a single exponential form when $\gamma \neq 1$ and a constant form when $\gamma = 1$. The existence of such ADOS's, which are called the Freundlich and Temkin types, was the hypothesis behind the discussion of the power-law evacuation curve in previous papers [95, 96, 187]. It is worth emphasizing that the equivalence of the power-law decay described by Eq. (4.29) with the Freundlich- or Temkin-type ADOS is analytically derived in the present study.

It should be noted that Eq. (4.36) is intrinsically independent of T. Therefore the relation that the partial differential of Eq. (4.36) with respect to T is equal to 0 deduces the temperature dependence of γ.

Additionally, we note that ADOS in equation (4.36) is rewritten as a power of the Boltzmann factor $e^{-\beta E}$ that gives the relative probability of the adsorption state,

$$g_a(e^{-\beta E}) \propto (e^{-\beta E})^{\frac{1}{\gamma}-1}. \tag{4.38}$$

This suggests that the number of the state follows a power law with a fractal character. Some surfaces show a fractal feature in which the number of the flat region follows a power of the area with a fractal dimension [199, 200]. Clarifying the detailed relationship between the surface structure and ADOS in terms of the power-law behavior is a subject for a future work.

Quasi-static equilibrium in $P-t$ curves with power-law shapes

In this section, we evaluate Eq. (4.16). For this purpose, considering the maximum value of $\epsilon\theta_1/\theta_0$ as a function of n^* in Eq. (4.16) is sufficient. dn^*/dt^* is obtained from Eq. (4.29) as follows:

$$\frac{dn^*}{dt^*} = -T\left(\frac{N}{\beta\alpha}\right)^{\frac{1}{\gamma}} \gamma n^{*\left(1+\frac{1}{\gamma}\right)}. \tag{4.39}$$

Substituting Eq. (4.39) into Eq. (4.16) represents $\epsilon\theta_1/\theta_0$ as a function of n^*,

$$\left|\frac{\epsilon\theta_1}{\theta_0}\right| = \tau\left(\frac{N}{\beta\alpha}\right)^{\frac{1}{\gamma}} \gamma \frac{n^{*\left(\frac{1}{\gamma}\right)}}{(n^*+1)^2}. \tag{4.40}$$

Then, the differentiation of Eq. (4.40) with respect to n^* is given by

$$\frac{\partial}{\partial n^*}\left|\frac{\epsilon\theta_1}{\theta_0}\right| = \tau\left(\frac{N}{\beta\alpha}\right)^{\frac{1}{\gamma}} (2\gamma-1)\frac{n^{*\left(\frac{1}{\gamma}-1\right)}}{(n^*+1)^3}\left(n^* - \frac{1}{2\gamma-1}\right). \tag{4.41}$$

In view of Eq. (4.41), $\epsilon\theta_1/\theta_0$ takes a local maximum in the region $n^* > 0$ with

$$n^* = \frac{1}{2\gamma-1} \tag{4.42}$$

when $\gamma > 1/2$. With $\gamma \leq 1/2$, Eq. (4.40) monotonically increases with increasing n^*. Hence, when the pressure measurement starts at $n^* = n_0^*$, Eq. (4.40) takes the maximum value of n_0^*. As a result, Eq. (4.16) is rewritten as

$$\left|\tau\left(\frac{N}{\beta\alpha}\right)^{\frac{1}{\gamma}} \frac{(1-2\gamma)^{2-\frac{1}{\gamma}}}{4\gamma}\right| << 1 \quad \left[\gamma > \frac{1}{2}\left(\frac{1}{n_0^*}+1\right)\right] \tag{4.43}$$

$$\left|\tau\left(\frac{N}{\beta\alpha}\right)^{\frac{1}{\gamma}} \gamma \frac{n_0^{*\left(\frac{1}{\gamma}\right)}}{(n_0^*+1)^2}\right| << 1 \quad \left[\gamma < \frac{1}{2}\left(\frac{1}{n_0^*}+1\right)\right]. \tag{4.44}$$

Interpretation of applicable condition of quasi-static equilibrium

In this section, we first evaluate T representing the time scale for the change of θ, and then discuss the quasi-static equilibrium condition. We define T as the time when $\theta(E,t)$ changes between $y(\sim 0.2)$ and $(1-y)$. When θ is not far from $\theta_0(E,t)$, substituting $\theta_0 = y$ and $\theta_0 = (1-y)$ into Eq. (4.14) gives the corresponding $n^*(t)$:

$$n^*(E,t_y) = \frac{y}{1-y}, \tag{4.45}$$

$$n^*(E,t_{(1-y)}) = \frac{1-y}{y}, \tag{4.46}$$

respectively. Here, t_y and $t_{(1-y)}$ denote the time at $\theta_0 = y$ and $\theta_0 = (1-y)$, respectively. Since $n^*(E,t_y) < n^*(E,t_c)$ and $n^*(E,t_{(1-y)}) > n^*(E,t_c)$, and both are on the order of 1, we consider the first-order Taylor expansion of $n^*(E,t)$ around $n^*(E,t_c)$ where t_c is defined by the time when $n^*(E,t_c) = 1$,

$$n^*(E,t) \sim n^*(E,t_c) + \left(\frac{dn^*}{dt}\right)_{t=t_c}(t-t_c). \tag{4.47}$$

Equation (4.47) gives

$$n^*(E,t_y) - n^*(E,t_{(1-y)}) = \left(\frac{dn^*}{dt}\right)_{t=t_c}(t_y - t_{(1-y)}). \tag{4.48}$$

Since $T(E) = \left|t_y(E) - t_{(1-y)}(E)\right|$, substituting Eqs. (4.45) and (4.46) into Eq. (4.48) yields

$$\frac{1}{T} = \left|\left(\frac{1}{n^*}\frac{dn^*}{dt}\right)_{t=t_c}\frac{y(1-y)}{1-2y}\right|. \tag{4.49}$$

Since $t = T \cdot t^*$,

$$\left|\left(\frac{1}{n^*}\frac{dn^*}{dt^*}\right)_{t=t_c}\right| = \frac{1-2y}{y(1-y)}. \tag{4.50}$$

As shown in Eq. (4.42), the left-hand side of Eq. (4.16) takes a maximum value when $n^* \sim 1$, in other words, $t \sim t_c$. Equation (4.16) is accordingly rewritten as

$$\max\left\{\left|\frac{\epsilon\theta_1}{\theta_0}\right|\right\} \sim \left|\epsilon\frac{1}{n^*}\frac{dn^*}{dt^*}\frac{1}{(n^*+1)^2}\right|_{t=t_c} << 1. \tag{4.51}$$

Substituting Eq. (4.50) into Eq. (4.51) gives

$$\max\left\{\left|\frac{\epsilon\theta_1}{\theta_0}\right|\right\} \sim \left|\epsilon\frac{1}{4}\frac{1-2y}{y(1-y)}\right| \sim \epsilon << 1. \tag{4.52}$$

Thus, $\epsilon\theta_1/\theta_0 << 1$ is equivalent to $\epsilon(E) << 1$. That is, when $T(E)$ is much longer than $\tau(E)$, the velocity of adsorption can be balanced with the velocity of desorption. Then, $\theta(E,t)$ becomes equal to $\theta_0(E,t)$; in other words, $\epsilon\theta_1$ becomes negligible compared with θ_0.

Kanazawa discussed the condition under which the quasi-static equilibrium holds. He assumed that the condition corresponds to

$$\left|\frac{1}{n}\frac{dn}{dt}\right| << \frac{d\phi}{dt}, \tag{4.53}$$

where $\phi \equiv \theta - \theta_0 \sim \epsilon\theta_1$ [96]. Since the maximum value of the left-hand side of Eq. (4.53) is $1/T$ as presented above, Eq. (4.53) corresponds to $1/\tau << d\theta_1/dt$. The meaning of Eq. (4.53) is neither physically clear nor mathematically rigorous. As discussed in this section, the applicable condition of the quasi-static equilibrium corresponds to $\epsilon << 1$, which indicates that the right-hand side of Eq. (4.53) should have been $1/\tau$.

Analogy of the formula with scanning tunneling spectroscopy

In this section, we describe the concept of the formula in this paper by comparison with the method for the measurement of the electronic density of states with scanning tunneling spectroscopy (STS). Figure 4.2(a) shows a schematic of the STS measurement. STS measures the electronic density of states (EDOS) $g_e(E)$ of a solid with a tunneling current by varying the applied voltage on the STM tip as a detector. Therefore, the STM tip plays the role of a mediator. As shown in Fig. 4.2(b), the applied voltage V on the tip modulates the chemical potential of the electron in the tip μ_m with respect to the chemical potential of the sample μ_s. EDOS at μ_m is given by $g_e(\mu_m) = (\partial/\partial\mu_m)\int_{-\infty}^{\infty} g_e(E) f_{FD}(E,\mu_m)dE$, where E is the energy of the electrons and $f_{FD}(E,\mu_m)$ is the Fermi-Dirac function. $\partial/\partial\mu_m$ is replaced by d/dV since the change of μ_m from μ_s is equal to V. The tunneling current I is proportional to $\int_{-\infty}^{\infty} g_e(E) f_{FD}(E,\mu_d)dE$ under the assumption that the tunneling probability of electrons and EDOS of the tip are independent of E [201]. We can therefore derive $g_e(E)$ from the first derivative of the tunneling current (dI/dV).

On the other hand, the formula derived in this paper regards the gas phase particles as the mediator and a pressure gauge as the detector, as shown in Fig. 4.2(c). The chemical potential of the gas particles of μ_m [Eq. (4.19)] is modulated by the evacuation or introduction of gas. When the change of μ_m satisfies the quasi-static equilibrium, the chemical potential of the sample μ_s becomes equal to μ_m, as shown in Eq. (4.21) and in Fig. 4.2(d). The information of ADOS at μ_m is reflected in the desorption flux of particles described as $F(\mu_m) = (\partial/\partial\mu_m)\int_{-\infty}^{\infty} g_{ads}(E)\theta_0(E,\mu_m)dE$. Then, we can deduce ADOS according to Eq. (4.28).

4.1.4 Conclusion

In this section, we derived an analytical formula for calculating the adsorption density of states (ADOS) on the surface of a chamber. The applicable condition of the quasi-static equilibrium is also shown rigorously. Using the formula, we derive exponential and constant forms of ADOS from the power-law decay of the pressure in evacuation processes. The formula can also deduce ADOS from an arbitrary form of pressure change in a chamber under the quasi-static equilibrium. The formula therefore contributes to understanding the microscopic behavior of gas particles on complex chamber surfaces, allowing us to evaluate the change in the surfaces, including reactivity, corrosion, and degradation, through the analysis of ADOS. Such knowledge is of essential importance for reaction chambers, pressure vessels, and nuclear reactors.

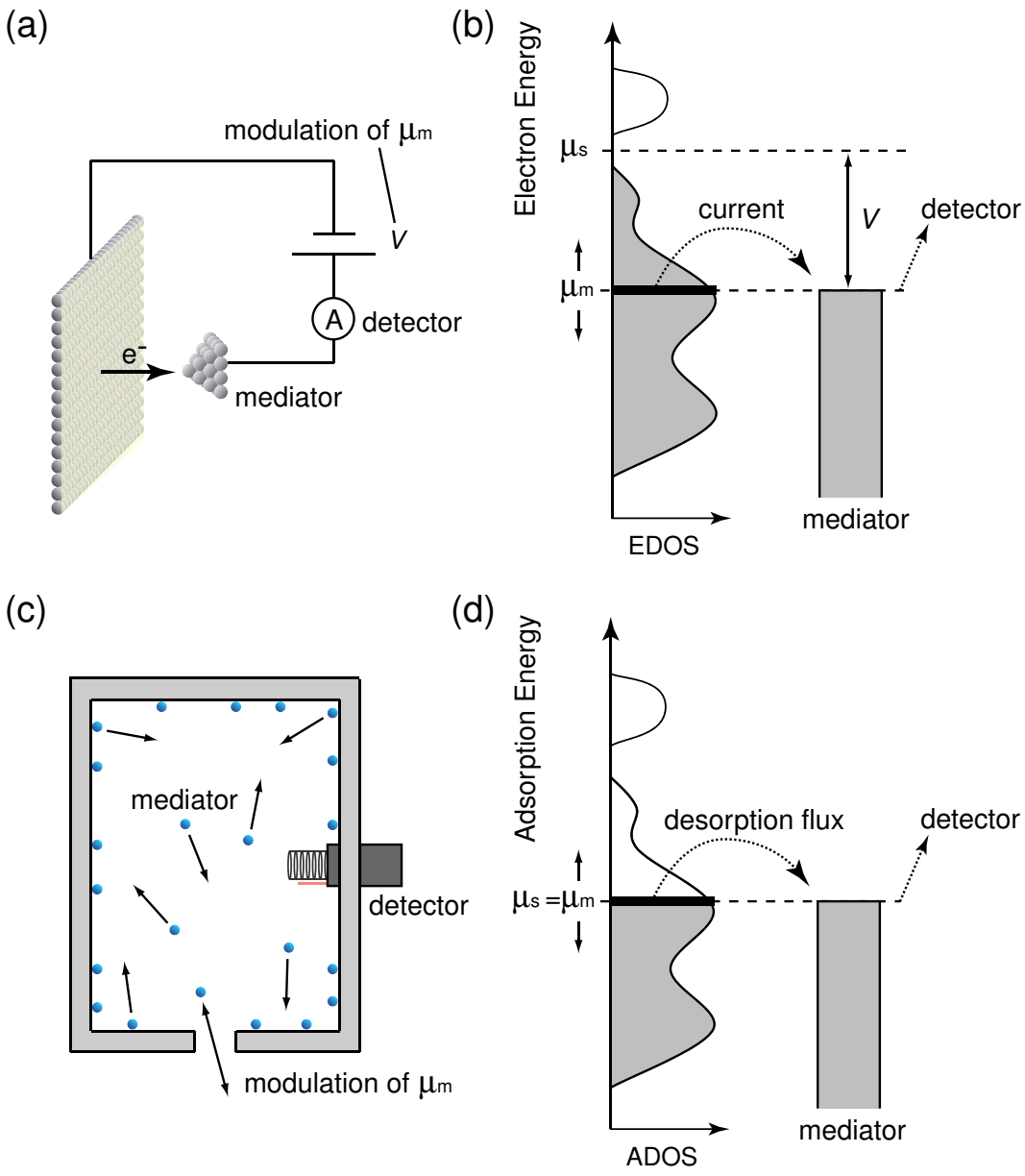

Figure 4.2: (a) Schematic illustration of scanning tunnel spectroscopy (STS) measurement. The STM tip and current meter act as the mediator and detector in the measurement. The applied voltage V modulates the chemical potential of the tip μ_m. (b) Concept of the measurement of the electron density of states (EDOS) with STS by variation of V. μ_s denotes the chemical potential for electrons of a sample. (c) Schematic illustration of the measurement of the adsorption density of states (ADOS) on the surface of a chamber. The gas phase and pressure gauge act as the mediator and detector in the measurement. A gate of the chamber modulates μ_m. (d) Concept of the measurement of ADOS of a sample with a modulation of μ_m. μ_m is equivalent to the chemical potential of the sample μ_s under the quasi-static equilibrium. Reproduced from the post-print of [192].

4.1.5 Appendix

One-particle partition function and chemical potential

Let $Q(\beta)$ be the one-particle partition function. The partition function of N particles is given by

$$Z(\beta) = \frac{1}{N!} Q(\beta)^N. \tag{4.54}$$

The grand partition function is

$$\Sigma(\beta, \mu) = \sum_N^\infty e^{\beta\mu N} Z. \tag{4.55}$$

Then, the expectation number of particles is written as

$$\langle N \rangle_{\beta,\mu} = \frac{1}{\beta} \frac{\partial}{\partial \mu} \ln \Sigma(\beta, \mu). \tag{4.56}$$

When $Q(\beta)$ does not include N, Eqs. (4.54) and (4.55) yield

$$\begin{aligned} \Sigma(\beta, \mu) &= \sum_N^\infty \frac{1}{N!} \left(Q e^{\beta\mu} \right)^N \\ &= \exp\left(Q e^{\beta\mu} \right). \end{aligned} \tag{4.57}$$

Here, $\sum_N^\infty x^N / N! = e^x$ was used. Substituting Eq. (4.57) into Eq. (4.56) gives

$$\begin{aligned} \langle N \rangle &= e^{\beta\mu} Q \\ \Leftrightarrow \frac{\langle N \rangle}{V} \frac{1}{q} &= e^{\beta\mu} \\ \Leftrightarrow \frac{n}{q} &= e^{\beta\mu}, \end{aligned} \tag{4.58}$$

where q is the one-particle partition function per volume.

General solution of $g_a(E)$

The general solution of

$$\sum_{i=0}^\infty \frac{a_i}{\beta^{2i}} \frac{d^{2i}}{dE^{2i}} g_a(E) = F(E) \tag{4.59}$$

is obtained as a sum of the general solution of a homogeneous Eq. (4.60) $g_a^h(E)$ and a special solution of Eq. (4.59) $g_a^s(E)$:

$$\sum_{i=0}^\infty \frac{a_i}{\beta^{2i}} \frac{d^{2i}}{dE^{2i}} g_a^h(E) = 0. \tag{4.60}$$

Substituting a characteristic solution $e^{\lambda E}$ with a constant λ into Eq. (4.60) yields the characteristic equation

$$\sum_{i=0}^{\infty} \frac{a_i}{\beta^{2i}} \lambda^{2i} = 0. \tag{4.61}$$

Solving Eq. (4.61) for λ gives an even number of solutions $\pm\lambda_i$, where λ_i's are imaginary numbers with a magnitude of $o(\beta)$ since $a_i > 0$ and $o(a_i) = 1$. Therefore, $g_a^h(E)$ is written as

$$g_a^h(E) = \sum_{i=1}^{\infty} \left(A_i e^{\lambda_i E} + B_i e^{-\lambda_i E} \right), \tag{4.62}$$

where A_i and B_i are constants. Next, the special solution of Eq. (4.59), $g_a^s(E)$, is given by

$$\begin{aligned} g_a^s(E) = \quad & \textstyle\sum_{i=1}^{\infty} \frac{e^{\lambda_i E}}{\phi'(\lambda_i)} \int F(E) e^{-\lambda_i E} dE \\ & + \textstyle\sum_{i=1}^{\infty} \frac{e^{-\lambda_i E}}{\phi'(-\lambda_i)} \int F(E) e^{\lambda_i E} dE, \end{aligned} \tag{4.63}$$

where $\phi'(\lambda_i) = (\lambda_i^2 - \lambda_1^2) \cdots (\lambda_i^2 - \lambda_{i-1}^2) 2\lambda (\lambda_i^2 - \lambda_{i+1}^2) \cdots$ [202]. Since $\phi'(-\lambda_i) = -\phi'(\lambda_i)$, replacing the integrals in Eq. (4.63) with partial integrals gives

$$\begin{aligned} g_a^s(E) &= \sum_{i=1}^{\infty} \left[\frac{e^{\lambda_i E}}{\phi'(\lambda_i)} \left(-\frac{1}{\lambda_i} e^{-\lambda_i E} \right) \left(F(E) + \frac{1}{\lambda_i} F'(E) + \frac{1}{\lambda_i^2} F^{(2)}(E) + \cdots \right) \right. \\ &+ \left. \frac{e^{-\lambda_i E}}{\phi'(-\lambda_i)} \frac{1}{\lambda_i} e^{\lambda_i E} \left(F(E) - \frac{1}{\lambda_i} F'(E) + \frac{1}{\lambda_i^2} F^{(2)}(E) + \cdots \right) \right] \\ &= \sum_{i=1}^{\infty} -\frac{1}{\lambda_i^2} \frac{1}{(\lambda_i^2 - \lambda_1^2)(\lambda_i^2 - \lambda_2^2) \cdots} \\ &\times \left(F(E) + \frac{1}{\lambda_i^2} F^{(2)}(E) + \cdots \right). \end{aligned} \tag{4.64}$$

Thus, $g_a^s(E)$ is expressed with constants b_{2j} as

$$g_a^s(E) = \sum_{j=0}^{\infty} b_{2j} F^{(2j)}(E), \tag{4.65}$$

where

$$b_{2j} = \sum_{j=0}^{\infty} \sum_{i=1}^{\infty} -\frac{1}{\lambda_i^{2+2j}} \frac{1}{(\lambda_i^2 - \lambda_1^2)(\lambda_i^2 - \lambda_2^2) \cdots} \tag{4.66}$$

$$= -\sum_{k=1}^{j} a_{2k} b_{2(k-l)}, \quad b_0 = 1. \tag{4.67}$$

The second equality is proved by mathematical induction or the following procedure. Since Eq. (4.65) is a solution of Eq. (4.59), Eq. (4.65) is simply substituted into Eq. (4.59) and we obtain

the identity

$$F(E) + \sum_{j=1}^{\infty} b_{2j} F^{(2j)}(E) + \sum_{i=1}^{\infty} \frac{a_i}{\beta^{2i}} \frac{d^{2i}}{dE^{2i}} \sum_{j=0}^{\infty} b_{2j} F^{(2j)}(E) = F(E)$$
$$\Leftrightarrow \sum_{j=1}^{\infty} b_{2j} F^{(2j)}(E) + \sum_{i=1}^{\infty} \frac{a_i}{\beta^{2i}} \frac{d^{2i}}{dE^{2i}} \sum_{j=0}^{\infty} b_{2j} F^{(2j)}(E) = 0. \tag{4.68}$$

In Eq. (4.68), coefficients of $F^{(2)}(E), F^{(4)}(E), F^{(6)}(E) \cdots$ must be 0, and we obtain the relation of Eq. (4.67).

Thus, the general solution of Eq. (4.59) is given by

$$g_a(E) = g_a^h(E) + g_a^s(E) \tag{4.69}$$
$$= \sum_{i=1}^{\infty} \left(A_i e^{\lambda_i E} + B_i e^{-\lambda_i E} \right) + \sum_{j=0}^{\infty} b_{2j} F^{(2j)}(E) \tag{4.70}$$
$$b_{2j} = -\sum_{k=1}^{j} a_{2k} b_{2(j-k)}, \quad b_0 = 1. \tag{4.71}$$

$g_a(E)$ satisfies the boundary condition

$$g_a(E) = 0 \ (E < E_{min}, E > E_{max}), \tag{4.72}$$

where E_{min} and E_{max} are constants. The first term on the left-hand side of Eq. (4.70) represents oscillatory solutions with a wavelength of $o(1/\beta)$ since λ_i's are imaginary numbers, as presented above. The oscillatory solutions with finite amplitudes cannot exist under the condition of Eq. (4.72), so that all A_m's and B_m's become 0. Therefore, the adsorption density of states is obtained as

$$g_a(E) = \sum_{j=0}^{\infty} b_{2j} F^{(2j)}(E)$$
$$= F(E) - \frac{\pi^2}{6\beta^2} F^{(2)}(E) + \frac{\pi^4}{120\beta^4} F^{(4)}(E) + \cdots. \tag{4.73}$$

4.2 Analysis of a Pumping Curve of Water with the Conversion Equation from Pressure to Adsorption Density of States

A pumping-down curve of a vacuum chamber often shows a power-law dependence on time, which has been attributed to a distribution of the adsorption energy of molecules on the chamber wall. We have recently derived an analytical formula that directly converts pressure changes as a function of time into the adsorption density of states (ADOS). In the present paper, on the basis of this formula, we analyzed the pumping-down curves reported in literatures to obtain ADOS of water molecules. The ADOS was dependent on the initial exposure pressure of water. The origin of the pressure dependence is discussed.

4.2.1 Introduction

The adsorption density of states (ADOS) on a vacuum chamber is a factor to decide evacuation speed. A form of ADOS depends on the composition and structures of a chamber surface, which is changed by baking and strong light irradiation. The quantitative evaluation of changes in chamber surfaces contributes to appropriate treatments of the surfaces.

In this section, experimentally-measured evacuation curves for water molecules were transformed into ADOS with the analytical formula presented in Chap. 4.1.

4.2.2 Review of the method to convert measured pressure change into ADOS

In this section, the analytical method presented in Chap. 4.1 is organized to apply it to measured evacuation curves.

ADOS $g_a(E)$ shown in Eq. (4.28) is given by

$$g_a(E) = F(E) - \frac{\pi^2}{6\beta^2}F^{(2)}(E) + \frac{\pi^4}{120\beta^4}F^{(4)}(E) + \cdots, \tag{4.74}$$

where β is $1/k_{\mathrm{B}}T$, k_{B} is Boltzmann constant, T is temperature, and μ_g is the chemical potential of gas phase. Substituting Eq. (4.33) into Eq. (4.24) and replacing μ_g with E gives $F(E)$ for vacuum chambers,

$$F(E) = \left\{ \left[-\frac{a\tilde{v}q_g}{A}\frac{1}{\left(\frac{d\mu_g}{dt}\right)} - \frac{\beta V q_g}{A} \right] \exp\left(\beta\mu_g\right) \right\}_{\mu_g=E}, \tag{4.75}$$

where $F^{(n)}(E) = d^nF/dE^n$, a is the area of an ideal orifice pump, $\tilde{v}$ is a quarter of the root-mean-

square velocity of gas particles, A is the surface area of a vacuum chamber, V is the volume of the chamber. μ_g is presented with pressure P and the partition function of translational motions of ideal gas molecules q_g as

$$\mu_g = \frac{1}{\beta} \ln\left(\frac{\beta P}{q_g}\right). \tag{4.76}$$

q_g is given by

$$q_g = \left(\frac{m}{2\pi\hbar^2\beta}\right)^{\frac{3}{2}}. \tag{4.77}$$

The usage of Eqs. (4.74) and (4.75) requires the adsorption-desorption equilibrium on chamber surfaces at each moment. A condition of the equilibrium is given by Eq. (4.16). We transform Eq. (4.16) into a form suitable for measured evacuation curves in vacuum chamber, which usually shows power-law decay as

$$P(t) = \alpha t^{-\gamma}, \tag{4.78}$$

where α and γ are constants. Because γ usually takes values near 1, Eq. (4.42) derives $n^* = 1$. Substituting $n^* = 1$ into Eq. (4.16) yields the applicable condition for Eqs. (4.74) and (4.75) with the reaction velocity of first-order desorption k_{d},

$$\left|\frac{1}{P(t)}\left(\frac{dP}{dt}\right)\right|_{t=t_c} << k_d. \tag{4.79}$$

Here, a relation $n(t) = \beta P(t)$ is used. t_c is defined by

$$P(t_c) = \frac{q_g}{\beta} \exp\left(\beta E\right). \tag{4.80}$$

t_c indicates a time when the coverage of a site with adsorption energy E becomes approximately 1/2. The left-hand side in Eq. (4.79) approximately shows the maximum as shown in Eq. (4.51). Therefore, the satisfaction of Eq. (4.79) enable us to use Eqs. (4.74) and (4.75) at all the time.

4.2.3 Analysis of experimentally-measured evacuation curves

In this section, evacuation curves measured by Li *et al.* are converted to ADOS 's. Li *et al.* exposed a chamber made of 304 type stainless steel to water vapor with pressures of 8.0, 0.8, 0.12, 1.2×10^{-2}, and 8.0×10^{-4} Torr (1.1×10^3, 1.1×10^2, 16, 1.6, and 1.1×10^{-1} Pa, respectively) for 60 min following the baking of the chamber. Figure 4.3 shows the evacuation curves measured after the water exposure. The right axis in Fig. 4.3 indicates the chemical potential of water molecules in gas phase corresponding to the pressure shown in the left axis. The chemical potential is calculated with Eq. (4.76). Solid lines are fittings on the data by Eq.(4.78), which demonstrate that the evacuation curves follow power-law decays with γ of approximately 1.

We secondly evaluate the evacuation curves in Fig. 4.3 in terms of Eq. (4.79). Figure 4.4

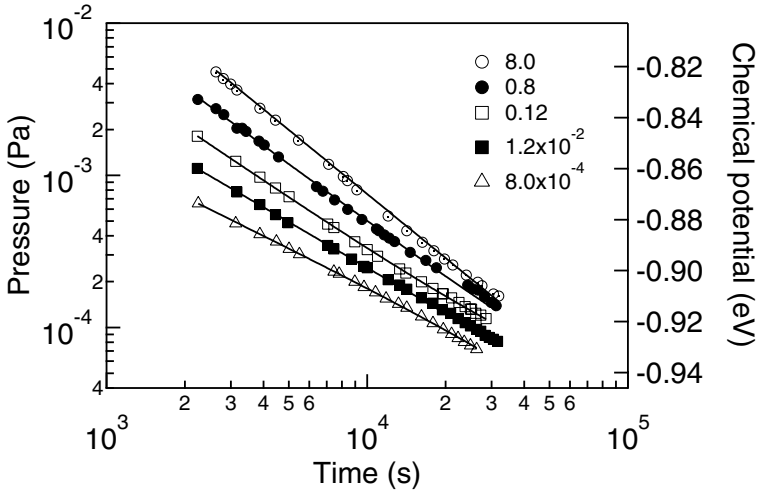

Figure 4.3: Pumping down curves obtained by Li *et al*. [198] for an electro-polished stainless steel (SUS304) vacuum chamber exposed to H_2O for 60 min with pressures of 8.0, 0.8, 0.12, 1.2×10^{-2}, and 8.0×10^{-4} Torr. The solid lines are the results of fitting with a power-law decay function. The chemical potential of gas phase corresponding to the pressure is plotted on the vertical axis of the right-hand side. Adapted from the post-print of [203].

shows the left-hand side of Eq. (4.79) $|(dP/dt)/4P|_{t=t_c}$'s calculated from the evacuation curves in Fig. 4.3 as a function of E. In order to estimate values of k_d in Eq. (4.79), we assume that k_d is presented as Arrhenius equation: $k_d = k_0 \exp(\beta E_d)$ where E_d is the activation energy of desorption. We use 7×10^{12} (s^{-1}) [85] and $-E$ for the value of k_0 and E_d respectively. The calculated k_d is shown as a solid line in Fig. 4.4. $|(dP/dt)/4P|_{t=t_c}$'s for each evacuation curve are 2 or 3 orders of magnitude less than k_d, which means that the evacuation curves in Fig. 4.3 satisfy Eq. (4.79). In other words, adsorption-desorption equilibrium is held at each moment and ADOS for the evacuation curves can be estimated with Eq. (4.74).

The pumping speed in Li *et al*.'s chamber is not listed, however it is estimated as 6 l/s on the assumption that the surface area of their vacuum chamber is 1 m^2 and the total area density of adsorbed water is 1×10^{15} cm^{-2}. If one use a pump with the pumping speed of 100 l/s, for example, a measured evacuation curve with the pump does not satisfy Eq. (4.79). In order to evaluate ADOS with Eq. (4.74), slower pumping speed, which satisfy Eq. (4.79), is required.

Then substituting μ_g and $d\mu_g/dt$ for $P(t)$ in Fig. 4.3 calculated with Eqs. (4.76) into Eq. 4.75 gives $F(E)$ as shown in Fig. 4.5. Combining Eqs. (4.76), (4.74), and (4.75) analytically yields

$$F(E) = \frac{avq_g\beta}{4A\gamma}\left(\frac{\alpha\beta}{q_g}\right)^{\frac{1}{\gamma}} \exp\left[\left(1-\frac{1}{\gamma}\right)\beta E\right]. \tag{4.81}$$

Solid lines in Fig. 4.5 are calculated from Eq. (4.81), which is substituted fitting parameters α and γ in Fig. 4.3.

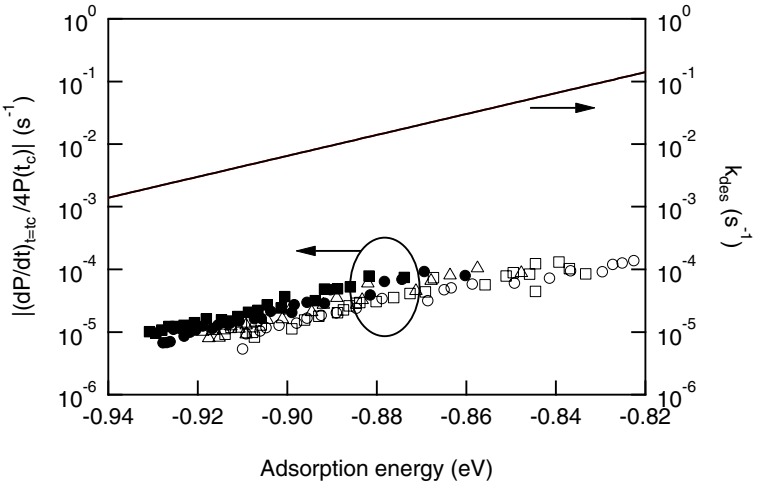

Figure 4.4: $|(dP/dt)/4P|_{t=t_c}$ as a function of the adsorption energy obtained from the experimental data in Fig. 4.3. k_d is plotted as a function of adsorption energy on the vertical axis of the right-hand side. The notations follow Fig. 4.3. Adapted from the postprint of [203].

We finally obtain $g_a(E)$ substituting $F(E)$ into Eq. (4.28). In Fig. 4.5, intervals of the measurement points for $F(E)$ are broad compared with the displacements toward vertical axis, because intervals of the measurement points in Fig. 4.3 is broad. This results in divergence of second and higher terms in Eq. (4.74), which include second or higher orders of differentials. Thus, an application of Eq. (4.74) requires dense measurement points and small errors in a measured evacuation curve to evaluate differentials with higher order as finite values. In the present case, we substitute the solid lines in Fig. 4.5 into Eq. (4.74) for calculation of $g_a(E)$ to avoid the divergence of the terms. Fig. 4.6 shows the calculated ADOS. The shapes of $g_a(E)$ in Fig. 4.6 are similar to and 87∼100 % as much as that of $F(E)$ in Fig. 4.5. This is because $F(E)$ is an exponential function deriving from Eq.(4.81), which is preserved even after the substitution into Eq.(4.74). However, it should be noted that $F(E)$ with a general shape does not become similar to $g_a(E)$.

Fig. 4.6 shows two features by the increase of water exposure. One is the increase of the occupation number in ADOS. The other is changes in the forms of ADOS, which indicates that the number of surface molecules with certain adsorption energy depends on the amount of water exposure.

4.2.4 Discussion

The obtained ADOS distributed at around −0.88 eV. The value is consistent with a measured activation energy of water on an α-Cr_2O_3(001) surface of 0.93 eV [85]. Furthermore, a theoretical work showed that several adsorbed states of water on a Cr_2O_3(0001) surface with the adsorption energy between −0.14 eV and −1.20 eV [204]. The possible multiple adsorbed states can

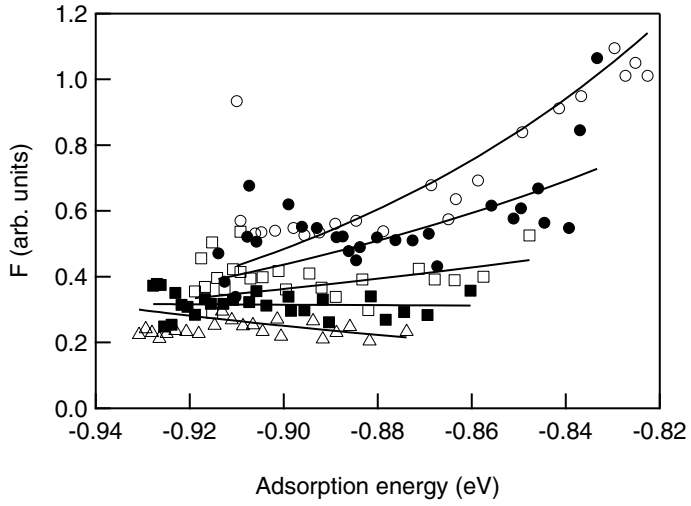

Figure 4.5: F as a function of the adsorption energy obtained from the experimental data and the fitting curves in Fig. 4.3. The notations follow Fig. 4.3. Adapted from the post-print of [203].

explain the distribution of the adsorption energy of water.

Next, we consider the reason for the changes of the form of ADOS. The candidates for the reason include that the out-of-plane diffusion of molecules, change in the condition of the surface, and the in-plane diffusion of molecules on the surface.

When surface pores or an oxide layer absorb water molecules and release them following the diffusion, the desorption of H_2O is delayed by the diffusion. Therefore, sites in pores or an oxide layer are analyzed that they effectively have larger adsorption energy compared with the original adsorption energy of the sites. An out-of-plane diffusion effect can be distinguished by measurements of pressure changes in which the pumping speed is modulated. Furthermore, structure and composition of stainless steel surfaces are often changed by heating. A baking process of a chamber may change surface structures and the composition, as a result, may change the form of ADOS in each experiment.

In the case that exposed gas molecules adsorb and diffuse on a surface, ideally they sequentially occupy sites with lower adsorption energy. However, lower diffusion velocity of the molecules disturbs the diffusion toward sites with lower adsorption energy after the adsorption on sites with higher adsorption energy.

For example, ADOS with the water exposure of 8.0×10^{-4} Torr in the range between -0.93 eV and -0.88 eV is less than ADOS with the water exposure of 8.0 Torr. This means that the water exposure of 8.0×10^{-4} Torr remains sites to be adsorbed between -0.93 eV and -0.90 eV. In other words, part of water adsorbing sites with adsorption energy of about -0.88 eV did not diffuse to sites with lower adsorption energy, which keeps sites with adsorption energy of between -0.92 eV and -0.90 eV unoccupied. Thus, insufficient diffusion cannot realize the most stable adsorption state on a surface. Measurements of intrinsic ADOS require the slow

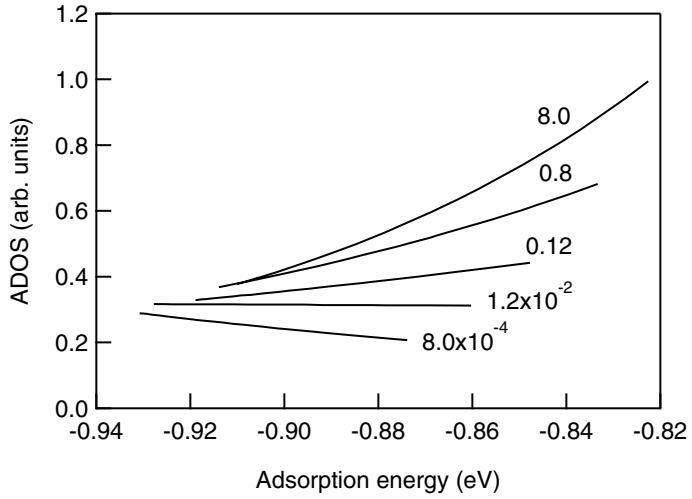

Figure 4.6: $g_a(E)$ as a function of the adsorption energy obtained from the fitting curves in Fig. 4.3. Adapted from the post-print of [203].

and long time exposure of molecules.

4.2.5 Conclusion

We have converted the evacuation curves in Fig. 4.3 to ADOS's in Fig. 4.6 using an analytical formula for calculating ADOS on chamber surfaces from measured pressure change derived in Sect. 4.1. The obtained ADOS's depend on the amount of initial water exposure. This is considered to reflect the out-of-plane diffusion of adsorbed water, the history of the stainless steel surface, or differences of adsorbed states of water. A specification of the factors requires several measurements with different conditions of exposure, temperature in the chamber, and pumping speed.

Analyses of ADOS's are available for other kinds of chambers as well as for vacuum chambers. For example, gas pipe lines and nuclear reactors must avoid the degradation of the surfaces and reaction chambers bring the decrease of reactivity on the surfaces into question. Constant analyses of ADOS's on the chambers quickly and easily notice us microscopic structural changes in the surfaces and changes in ADOS's influencing on reactivity.

Surfaces on vacuum chambers consist of amorphous oxides and hydroxides. Behaviors of gas molecules such as water and hydrogen on the surfaces remains to be elucidated. Applications of the analytical method shown in this study on stored evacuation curves make it possible to quantitatively discuss ADOS's on various surfaces. Obtained knowledge from the analyses will contribute the development of fundamental science on practical surfaces.

4.3 Temperature Dependence of Hydrogen Depth Distribution in the Near-Surface Region of Stainless Steel

The depth profile of hydrogen at a type 304 stainless steel surface was investigated with $^{1}H(^{15}N, \alpha\gamma)^{12}C$ nuclear reaction analysis at various temperatures. Hydrogen was predominantly distributed in the region shallower than 10 nm (surface hydrogen) with an area density of $\sim 1 \times 10^{16}$ cm^{-2}. Hydrogen was found to also exist in a deeper region (>30 nm) with a constant volume density of $\sim 4 \times 10^{20}$ cm^{-3} (bulk hydrogen). While both bulk and surface components gradually decreased as the temperature rose, part of the intensities remained even at 975 K. From the temperature dependence of the amount of the surface hydrogen, the distribution of the activation energy for desorption is discussed.

4.3.1 Introduction

Water and molecular hydrogen are most abundant residual gases in vacuum systems made of stainless steel. In the case of water, the adsorption energy has been shown to reveal a distribution [95, 96, 192, 203], which means that water exists in various adsorption states. The adsorption type is considered to include dissociative adsorption, coordinative adsorption, adsorption through hydrogen bond and formation of hydroxides [204]. Residual hydrogen is, on the other hand, considered to be released into a vacuum following diffusion in the bulk [205]. This indicates that the binding energy and depth distribution of hydrogen species near the surface directly influence the outgassing rate of water and hydrogen in a vacuum system.

Only a few works have studied the depth profile of hydrogen in stainless steel [206, 207, 208] because of the experimental difficulty to quantitatively detect hydrogen. Nuclear reaction analysis (NRA) studies with H-specific $^{1}H(^{15}N, \alpha\gamma)^{12}C$ showed that stainless steel contains hydrogen of $\sim 5 \times 10^{16}$ cm^{-2} at the surface and $10^{20} \sim 10^{21}$ cm^{-3} in the bulk [206, 207]. Furthermore, a study with position-sensitive atom probe (PoSAP) revealed that deuterium coexists with Cr, Ni, and O rather than Fe in stainless steel, and the existence of strongly bound hydrogen in nickel hydride and nickel hydroxide was proposed [208]. However, the thermal stability of hydrogen at each depth, which directly influences the outgassing in a vacuum remained to be done.

In this section, we have studied the temperature dependence of the hydrogen depth profile for a type 304 stainless steel with NRA. The distribution of the activation energy for hydrogen desorption was analyzed on the basis of the experimental data, which is discussed to show a wide distribution from 1.1 to 2.4 eV.

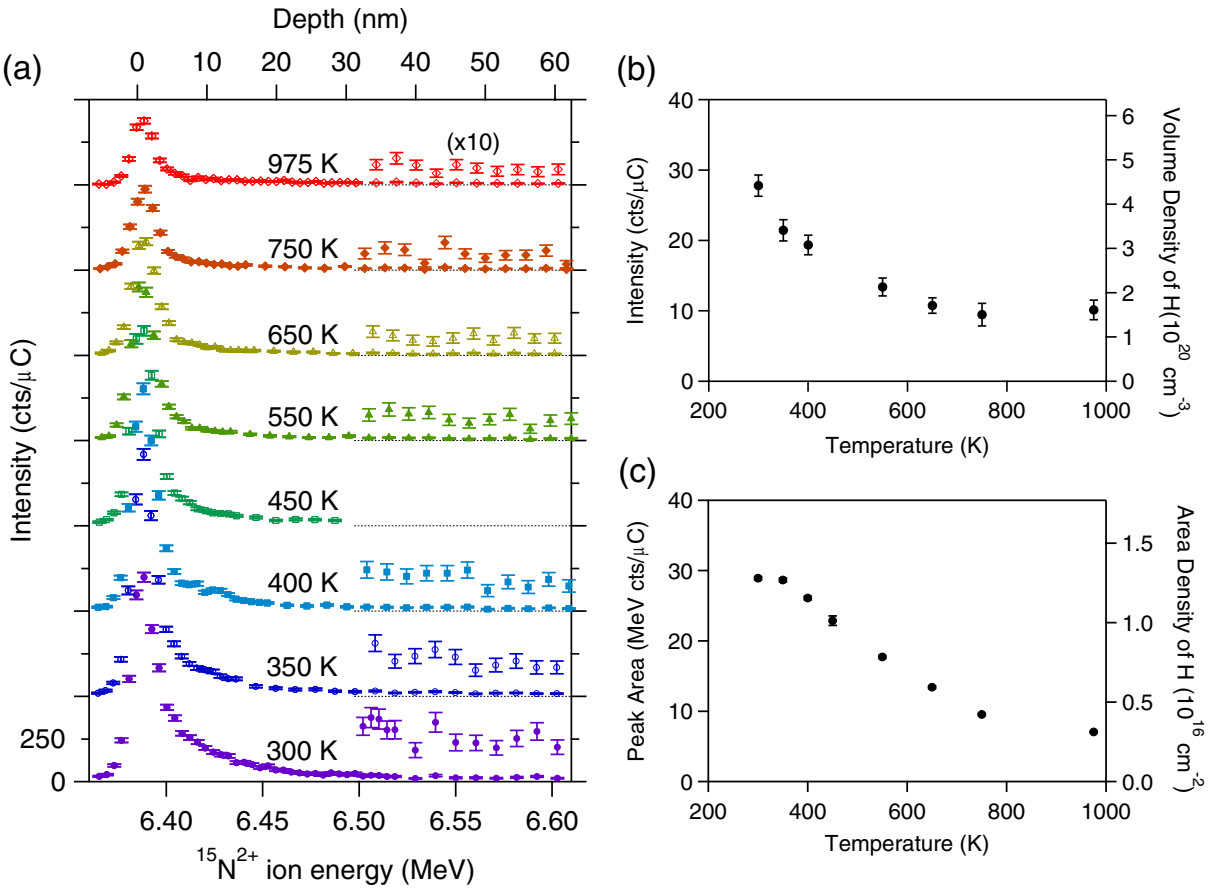

Figure 4.7: (a) NRA profiles on a type 304 stainless steel surface measured at different temperatures. (b) Average γ-ray yields induced by $^{15}N^{2+}$ with higher energy than 6.50 MeV. (c) The integral of the NRA profiles from which the average γ-ray yields are subtracted. Reproduced from a pre-print of [209].

4.3.2 Experimental detail

The sample used in this study is a type 304 stainless steel tip. Its bulk composition confirmed by X-ray fluorescence analysis is 71.6Fe, 18.6Cr, Ni8.4, Mn1.0, Cu0.1, V0.1, Mo0.1 in mol %. The sample is washed with an ultrasonic cleaner in acetone, ethanol and distillated water respectively.

The absolute amount of hydrogen at each depth of the sample were investigated by NRA at the 1C beam line of the 5 MV Van de Graaff Tandem accelerator in the Microanalysis Laboratory (MALT) of The University of Tokyo. The $^{15}N^{2+}$ ion beam irradiated the surface at a current of 40-100 nA and a beam diameter of 2-4 mm on the surface at room temperature. The stopping power (dE/dz) of 6.61 keV/nm for SUS304) [165] is used for defining the probing depth.

4.3.3 Results

Figure 4.7 (a) shows NRA profiles for a type 304 stainless steel surface heated to temperatures of 300 to 975 K. The NRA profile was taken with the sample kept at respective temperatures except that at 975 K. After a measurement, the temperature was raised to the next temperature in an incremental manner. The heating time was therefore in accordance with the measurement time of NRA, which is about 40 min. The sample was finally heated at 975 K for 5 min, and the NRA profile was taken after the temperature was decreased to room temperature. The profile for the 300 K sample reveals a maximum at E_{i} of 6.388 MeV, which is 3 keV higher than the resonance energy. The peak has a FWHM of 17 keV and a tailing feature at a high-energy region. This firstly indicates that the near-surface region with a thickness of ∼10 nm contained a substantial amount of hydrogen (surface hydrogen). Secondly, the bulk region (E_{i} >∼6.50 MeV) also contained a certain amount of hydrogen (bulk hydrogen). Both surface and bulk components were reduced in intensity by the increase of the temperature, however, they remained even after annealing at 975 K.

Figure 4.7 (b) shows the average γ-ray yield in the bulk region as a function of temperature. The right axis in Fig. 4.7 (b) denotes the volume density of the bulk hydrogen calculated from the γ-ray yields. It is apparent that the volume density of the bulk hydrogen immediately start to decrease by elevating the sample temperature and remains almost constant above 550 K. The result implies that there are at least two types of hydrogen in this depth region: One is removed by heating up to 550 K and the other remains above 550 K. Fe, Cr and Ni can contain hydrogen as solid solution with different enthalpies [210]. Furthermore, Ni forms hydride with an enthalpy of −0.30 eV/atom [210]. The different thermal stability of the bulk hydrogen is considered to reflect the differences in the binding state of hydrogen in the sample.

Figure 4.7 (c) shows the integral of the γ-ray yield for the surface hydrogen from which the average γ-ray yields of the bulk hydrogen are subtracted. The average γ-ray yield for 450 K is assumed to have the average value between the value for 400 K and 550 K. The integral correponds to the area density of the surface hydrogen, which is plotted on the right axis in Fig. 4.7 (c). The area density of the surface hydrogen was 1.3×10^{16} cm^{-2} at 300 K. Then it gradually decreases above 400 K and remains constant even at 975 K.

4.3.4 Discussion

We discuss the thermal stability of the surface hydrogen. Hydrogen in stainless steel is released into a vacuum after diffusion to the surface and desorption from the surface. The rate-determining step for the release is considered to be desorption from the surface [211, 212]. Up to 400 K, as seen in Fig. (4.7) (b) and (c), the bulk component appears to decrease significantly, while the decrease of the surface component is marginal. This suggests that bulk diffusion of hydrogen is faster than desorption. We therefore assume that desorption is the rate-determining process here. Then, the thermal stability of the surface hydrogen reflects the effective activation energy of desorption E_{d} of the entire outgassing process of hydrogen. Here, we consider both

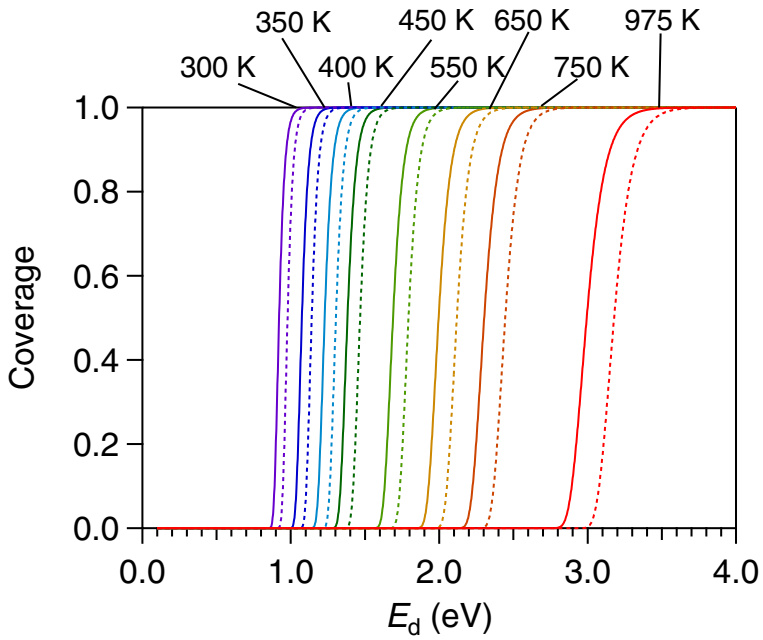

Figure 4.8: The calculated coverage of the site with E_d at each temperature after 300 s (solid lines) and 2700 s (dashed lines). Reproduced from a pre-print of [209].

first-order and second-order processes for hydrogen desorption.

The time dependence of the coverage θ_1 and $theta_2$ in the first- and second-order processes with an activation energy of E_d at constant temperature T is respectively given by

$$\begin{cases} \dfrac{d\theta_1(E_d,t)}{dt} = -A_1 e^{-E_d/k_B T}\theta_1(E_d,t), & \text{(4.82a)} \\ \dfrac{d\theta_2(E_d,t)}{dt} = -A_2 e^{-E_d/k_B T}\theta_2(E_d,t)^2, & \text{(4.82b)} \end{cases}$$

where A_1 and A_2 are constants. We use 7.7×10^{12} s^{-1} for A_1, which is reported for water desorption from Cr_2O_3 [85]. We use the same value for A_2, because A_2 has been shown to be similar to A_1 for the desorption-limited second-order desorption and the reaction-limited second-order desorption [213]. The coverage at a temperature of T and a time of t_1 with an initial coverage of 1 is given by

$$\begin{cases} \theta_1(E_d,t_1) = \exp\left[-A_1 e^{-E_d/k_B T} t_1\right], & \text{(4.83a)} \\ \theta_2(E_d,t_1) = \dfrac{1}{A_2 e^{-E_d/k_B T} t_1 + 1}. & \text{(4.83b)} \end{cases}$$

The NRA measurement was started about 300 s after the sample temperature was raised, and the measurement time was less than 2400 s. The sample was accordingly kept at a constant temperature for between 300 s and 2700 s. Therefore, t_1 is in the range between 300 s and 2700 s. Figure 4.8 shows the hydrogen coverage after heated at each temperature for 300 s (solid

lines) and 2700 s (dashed lines) for the first-order reaction calculated with Eq. (4.83a) as a function of E_{d}. Here, the threshold activation energy $E_{\mathrm{d-th}}(t_1, T)$ of desorption is defined by the energy at which the coverage becomes 1/2 after heating at a temperature of T for the time t_1. The transformation of Eqs. (4.83a) and (4.83b) gives $E_{\mathrm{d-th}}(t_1, T)$ as

$$\begin{cases} E_{\mathrm{d-th}}(t_1, T) = k_{\mathrm{B}}T \ln(A_1 t_1) - k_{\mathrm{B}}T \ln(\ln 2). & \text{(4.84a)} \\ E_{\mathrm{d-th}}(t_1, T) = k_{\mathrm{B}}T \ln(A_2 t_1). & \text{(4.84b)} \end{cases}$$

We furthermore define $E_{\mathrm{d-th}}(T)$ as

$$E_{\mathrm{d-th}}(T) = \frac{E_{\mathrm{d-th}}(300\ \mathrm{s}, T) + E_{\mathrm{d-th}}(2700\ \mathrm{s}, T)}{2}. \quad (4.85)$$

Then, the relations of $\theta(E_{\mathrm{d}}, t_1) = 0$ when $E_{\mathrm{d}} < E_{\mathrm{d-th}}$ and $\theta(E_{\mathrm{d}}, t_1) = 1$ when $E_{\mathrm{d}} > E_{\mathrm{d-th}}$ hold within an error of $\sim 2k_{\mathrm{B}}T$. The error of $\sim 2k_{\mathrm{B}}T$ comes from the uncertainty of the coverage rise ($\sim k_{\mathrm{B}}T$) and the uncertainty in t_1 ($\sim k_{\mathrm{B}}T$). It should be noted that the difference in the $E_{\mathrm{d-th}}(t_1, T)$ calculated for the firsr-order and the second-order desorptions is about $0.37k_{\mathrm{B}}T$, which is sufficiently smaller than the error of $\sim 2k_{\mathrm{B}}T$. In a first approximation, hydrogen desorbed at a temperature of T can be regarded to have the activation energy for desorption of $E_{\mathrm{d-th}}(T)$ following the first-order desorption.

In Fig. 4.7 (c), we focus on two successive measurements at temperatures of T_1 and T_2 ($T_2 > T_1$). We let the difference in the area density of hydrogen at T_1 and T_2 be $\Delta\sigma_{12}$, which corresponds to the amount of desorbed hydrogen at temperature between T_1 and T_2. The desorbed hydrogen is regarded to have the activation energy of desorption between $E_{\mathrm{d-th}}(T_1)$ and $E_{\mathrm{d-th}}(T_2)$. Therefore, the averaged density of states in terms of the desorption energy between $E_{\mathrm{d-th}}(T_1)$ and $E_{\mathrm{d-th}}(T_2)$ is given by $\Delta\sigma_{12}/[E_{\mathrm{d-th}}(T_1) - E_{\mathrm{d-th}}(T_2)]$.

Figure 4.9 shows the density of states as a function of the activation energy of desorption (DOS-E_{d}) calculated from Fig. 4.7 (c) with the above procedure. DOS-E_{d} is mainly distributed from 1.1 ± 0.05 eV to 2.4 ± 0.08 eV and shows tails below 1.1 eV and above 2.4 eV. The high activation energy of desorption indicates that hydrogen makes chemical bonds and is included in species such as chemisorbed water and hydroxides.

The density of states of the adsorption energy $E(< 0)$ of water (DOS-E) has been analyzed on a stainless chamber surface by using measured pressure changes [192, 203]. It has been shown that DOS-E forms a constant and an exponential distribution in the measured range between E of -0.93 eV and -0.82 eV and the distribution makes the power-law decay of the pressure in evacuation processes. When there is an activation energy for adsorption E_{a}, E is given as $E = -(E_{\mathrm{d}} - E_{\mathrm{a}})$. E_{a}'s for water on stainless steel surfaces are reported as 0.18 eV $\sim$ 0.32 eV [214]. Based on the values of E_{a}'s, the left edge of the broad distribution of DOS-E_{d} between 1.1 eV $\sim$ 1.2 eV shown in Fig. 4.9 is identical to the adsorption energy of between -0.93 eV and -0.83 eV. The analyzed DOS-E is considered to correspond to the left edge region of DOS-E_{d} shown in Fig. 4.9.

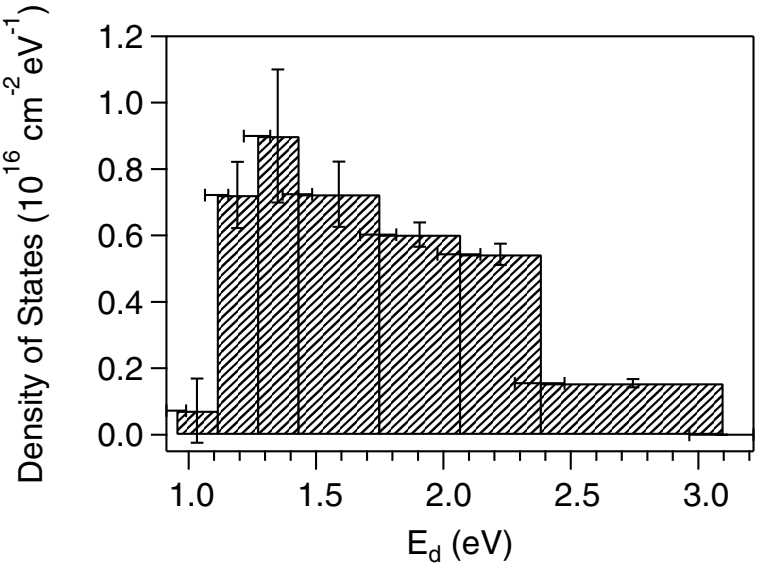

Figure 4.9: The density of state of the activation energy of desorption of the surface hydrogen calculated from Fig. 4.7 (c). Reproduced from a pre-print of [209].

4.3.5 Summary

We have studied the temperature dependence of the depth profile of hydrogen on a type 304 stainless steel surface with NRA. The near-surface region with a depth of 10 nm contains hydrogen of $\sim 1 \times 10^{14}$ cm^{-2}. The deeper region (>30 nm) also contains hydrogen with a constant volume density of $\sim 4 \times 10^{20}$ cm^{-3}. Both surface and bulk hydrogen decreased as the temperature increased, though they remained even at 975 K. The activation energy of desorption of surface hydrogen was discussed to be distributed from 1.1 eV to 2.4 eV.

Chapter 5

Conclusions

The present study investigated the interaction of molecules with single-crystal and inhomogeneous oxide surfaces, and the following conclusions were obtained.

1. Oxygen vacancies were introduced on $SrTiO_3$(001) with electron stimulated desorption, and its electronic structure was investigated by ultraviolet photoemission spectroscopy (UPS). The oxygen vacancy induced an in-gap state at 1.3 eV below the Fermi level, which is ascribed to electron doping from the oxygen vacancy to the surface. At the same time, the band was bent downward, which seems to form a surface conductive layer. Subsequent oxygen exposure vanished the in-gap state and induced upward band-bending to the original position. The densities of the oxygen vacancy and electron induced by the oxygen vacancy were estimated to be 1×10^{14} and 2×10^{14} cm^{-2}, respectively.

2. The effects of hydrogen adsorption on the electronic structure of the oxygen-vacancy-controlled $SrTiO_3$(001) surfaces were investigated by UPS. The in-gap state on the oxygen-defficient (OD) $SrTiO_3$(001) surface was partially removed by hydrogen. On the other hand, the in-gap state was induced by hydrogen adsorption on the nearly-vacancy-free (NVF) $SrTiO_3$(001) surface. The areal densities of the adsorbed hydrogen were measured as $(0.9 \pm 0.7) \times 10^{14}$ and $(3.1 \pm 0.8) \times 10^{14}$ cm^{-2} by nuclear reaction analysis (NRA). From these results, the charged state of hydrogen on the OD and NVF surfaces was estimated as H^- and $H^{0.3+}$, respectively. The stability and the adsorbed site of H^- was discussed.

3. An atomic and molecular hydrogen beam source and a state-selective detection system for scattered molecular hydrogen by resonance-enhanced multi-photon spectroscopy (REMPI) were developed. The molecular hydrogen scattered at the $SrTiO_3$(001) surfaces with and without oxygen vacancies was investigated with the developed system. The ortho-para conversion probabilities in the scattering on the surfaces with and without oxygen vacancies were estimated to be 0.28 ± 0.05 and 0.15 ± 0.05, respectively. The in-gap state due to oxygen vacancies was discussed to possess a localized spin.

4. An analytical formula for calculating the distribution of the adsorption energy of molecules (the adsorption density of states: ADOS) on vacuum chamber surfaces from a measured pressure change was derived. The applicable condition of the formula was rigorously

evaluated. The formula revealed that the general power-law relation of the pressure decay originates from exponential and constant forms of ADOS.

5. The ADOS's for water molecules on a stainless steel vacuum chamber were analyzed with the analytical formula from the evacuation curves. ADOS's showed exponential- and constant-like shapes ranging from -0.9 eV to -0.8 eV. The ADOS shape was found to depend on the amount of the initial water exposure. The reason of the dependence was discussed.

6. The depth profile of hydrogen on a stainless steel surface was measured with NRA at different temperatures. The profiles revealed a peak of 1.3×10^{14} cm^{-2} at the depth of a few nm from the surface and a constant concentration of 4.5×10^{20} cm^{-3} in the depth of 20∼60 nm. From the temperature dependence, the activation energy for desorption of the hydrogen near the surface was evaluated to be distributed from 1.1 to 2.4 eV.

References

[1] K. J. Wu, L. D. Peterson, G. S. Elliott, and S. D. Kevan: J. Chem. Phys. **91** (1989) 7964.

[2] C. T. Campbell: Surf. Sci. **157** (1985) 43.

[3] X. L. Peng, J. R. Peck, L. W. Anderson, C. J. Goebel, and J. E. Lawler: J. Appl. Phys. **88** (2000) 4097.

[4] K. Christmann: Surf. Sci. Rep. **9** (1988) 1.

[5] B. Gergen, H. Nienhaus, W. H. Weinberg, and E. W. McFarland: Science **294** (2001) 2521.

[6] H. Nienhaus, H. S. Bergh, B. Gergen, A. Majumdar, W. H. Weinberg, and E. W. McFarland: Appl. Phys. Lett. **72** (1999) 4046.

[7] H. Nienhaus, H. S. Bergh, B. Gergen, A. Majumdar, W. H. Weinberg, and E. W. McFarland: Phys. Rev. Lett. **82** (1999) 446.

[8] H. Nienhaus: Surf. Sci. Rep. **45** (2002) 1.

[9] S. Andersson, L. Wilzén, and J. Harris: Phys. Rev. Lett. **55** (1985) 2591.

[10] S. Andersson, L. Wilzén, M. Persson, and J. Harris: Phys. Rev. B **40** (1989) 8146.

[11] G. Armand and J. R. Manson: Phys. Rev. B **43** (1991) 14371.

[12] E. Cartier, J. H. Stathis, and D. A. Buchanan: Appl. Phys. Lett. **63** (1993) 1510.

[13] R. J. Gould and E. E. Salpeter: Astrophys. J. **138** (1963) 393.

[14] K. Fukutani and T. Sugimoto: Prog. Surf. Sci. **88** (2013) 279.

[15] R. J. Gould, T. Gold, and E. E. Salpeter: Astrophys. J. **138** (1963) 408.

[16] D. Hollenbach and E. E. Salpeter: Astrophys. J. **163** (1971) 155.

[17] D. Menzel and R. Gomer: J. Chem. Phys. **41** (1964) 3311.

[18] P. R. Antoniewicz: Phys. Rev. B **21** (1980) 3811.

[19] M. Mizuno, H. Kasai, and A. Okiji: Surf. Sci. **310** (1994) 273.

[20] K. Hasegawa, H. Kasai, W. A. Dino, and A. Okiji: Surf. Sci. **438** (1999) 283.

[21] J. A. Misewich, T. F. Heinz, and D. M. Newns: Phys. Rev. Lett. **68** (1992) 3737.

[22] C. Frischkorn and M. Wolf: Chem. Rev. **106** (2006) 4207.

[23] P. J. Feibelman and M. L. Knotek: Phys. Rev. B **18** (1978) 6531.

[24] M. L. Knotek and P. J. Feibeman: Phys. Rev. Lett. **40** (1978) 964.

[25] C. G. Silva, R. Juárez, T. Marino, R. Molinari, and H. García: J. Am. Chem. Soc. **133** (2011) 595.

[26] S. Nakade, Y. Saito, W. Kubo, T. Kitamura, Y. Wada, and S. Yanadida: J. Phys. Chem. B **107** (2003) 8607.

[27] A. Kudo and Y. Miseki: Chem. Soc. Rev. **38** (2009) 253.

[28] K. Pachucki and J. Komasa: Phys. Rev. A **77** (2008) 030501.

[29] E. Ilisca and S. Sugano: Phys. Rev. Lett. **57** (1986) 2590.

[30] E. Ilisca: Phys. Rev. Lett. **66** (1991) 667.

[31] E. Ilisca: Surf. Sci. **242** (1991) 470.

[32] E. Ilisca: J. Phys. I France **1** (1991) 1785.

[33] E. Ilisca, P. Jussieu, and P. Cedex: Prog. Surf. Sci. **41** (1992) 217.

[34] E. Ilisca and S. Paris: Surf. Sci. **363** (1996) 347.

[35] K. Svensson and S. Andersson: Surf. Sci. **392** (1997) L40.

[36] K. Niki, T. Kawauchi, M. Matsumoto, K. Fukutani, and T. Okano: Phys. Rev. B **77** (2008) 201404.

[37] A. L. Linsebigler, G. Lu, and J. T. Yates: Chem. Rev. **95** (1995) 735.

[38] R. C. Alig and S. Bloom: Phys. Rev. Lett. **35** (1975) 1522.

[39] V. E. Henrich: Prog. Surf. Sci. **50** (1995) 77.

[40] C. C. Chang: J. Appl. Phys. **39** (1968) 5570.

[41] M. Gautier, J. P. Duraud, L. P. Van, and M. J. Guittet: Surf. Sci. **250** (1991) 71.

[42] K. Reuter and M. Scheffler: Phys. Rev. B **65** (2001) 35406.

[43] J. K. Rudra and W. B. Fowler: Phys. Rev. B **35** (1987) 8223.

[44] T. Bredow: Surf. Sci. **401** (1998) 82.

[45] V. E. Henrich, G. Dresselhaus, and H. J. Zeiger: Phys. Rev. Lett. **36** (1976) 1335.

[46] D. W. Reagor and V. Y. Butko: Nat. Mater. **4** (2005) 593.

[47] G. Herranz, O. Copie, A. Gentils, E. Tafra, M. Basletić, F. Fortuna, K. Bouzehouane, S. Fusil, E. Jacquet, C. Carrétéro, M. Bibes, A. Hamzić, and A. Barthélémy: J. Appl. Phys. **107** (2010) 103704.

[48] A. Boffa, C. Lin, A. T. Bell, and G. A. Somorjai: J. Catal. **149** (1994) 149.

[49] C. T. Campbell and C. H. F. Peden: Science **309** (2005) 713.

[50] S. H. Oh, R. Black, E. Pomerantseva, J.-h. Lee, and L. F. Nazar: Nat. Chem. **4** (2012) 1004.

[51] K. Kamiya, M. Young Yang, S.-G. Park, B. Magyari-Köpe, Y. Nishi, M. Niwa, and K. Shiraishi: Appl. Phys. Lett. **100** (2012) 073502.

[52] M. Y. Yang, K. Kamiya, B. Magyari-Köpe, M. Niwa, Y. Nishi, and K. Shiraishi: Appl. Phys. Lett. **103** (2013) 093504.

[53] K. Kamiya, M. Y. Yang, T. Nagata, S.-G. Park, B. Magyari-Köpe, T. Chikyow, K. Yamada, M. Niwa, Y. Nishi, and K. Shiraishi: Phys. Rev. B **87** (2013) 155201.

[54] D. Ricci, G. Bano, G. Pacchioni, and F. Illas: Phys. Rev. B **68** (2003) 224105.

[55] J. B. Malherbe, S. Hofmann, and J. M. Sanz: Appl. Surf. Sci. **27** (1986) 355.

[56] V. E. Henrich, G. Dresselhaus, and H. J. Zeiger: Solid Stat. Commun. **24** (1977) 623.

[57] S. Ferrer and G. A. Somorjai: Surf. Sci. **94** (1980) 41.

[58] V. E. Henrich and P. A. Cox: *The surface science of metal oxides* (Cambridge University Press, Cambridge, 1994).

[59] O. Dulub, M. Batzill, S. Solovev, E. Loginova, A. Alchagirov, T. E. Madey, and U. Diebold: Science **317** (2007) 1052.

[60] A. M. Azad, S. A. Akbar, S. G. Mhaisalkar, L. D. Birkefeld, and K. S. Goto: J. Electrochem. Soc. **139** (1992) 3690.

[61] J. Holc, J. Slunečko, and M. Hrovat: Sensors and Actuators B **26** (1995) 99.

[62] R. Ramamoorthy, P. K. Dutta, and S. A. Akbar: J. Mater. Sci. **38** (2003) 4271.

[63] M. Batzill and U. Diebold: Prog. Surf. Sci. **79** (2005) 47.

[64] N. Barsan, D. Koziej, and U. Weimar: Sensors and Actuators B: Chemical **121** (2007) 18.

[65] J. W. Fergus: Sensors and Actuators B: Chemical **123** (2007) 1169.

[66] B. Wang, L. F. Zhu, Y. H. Yang, N. S. Xu, and G. W. Yang: J. Phys. Chem. C **112** (2008) 6643.

[67] T. Hara, T. Ishiguro, N. Wakiya, and K. Shinozaki: Meter. Sci. Eng. **161** (2009) 142.

[68] K. Ozawa and K. Mase: Phys. Rev. B **83** (2011) 125406.

[69] Y. Wang, B. Meyer, X. Yin, M. Kunat, D. Langenberg, F. Traeger, A. Birkner, and C. Wöll: Phys. Rev. Lett. **95** (2005) 266104.

[70] F. Lin, S. Wang, F. Zheng, G. Zhou, J. Wu, B. L. Gu, and W. Duan: Phys. Rev. B **79** (2009) 35311.

[71] M. D'Angelo, R. Yukawa, K. Ozawa, S. Yamamoto, T. Hirahara, S. Hasegawa, M. Silly, F. Sirotti, and I. Matsuda: Phys. Rev. Lett. **108** (2012) 116802.

[72] R. Yukawa, S. Yamamoto, K. Ozawa, M. D'Angelo, M. G. Silly, F. Sirotti, and I. Matsuda: Phys. Rev. B **87** (2013) 115314.

[73] Y. Chen, M. M. Abraham, L. C. Templeton, and W. P. Unruh: Phys. Rev. B **11** (1975) 881.

[74] Y. Chen, V. M. Orera, R. Gonzalez, R. T. Williams, G. P. Williams, G. H. Rosenblatt, and G. J. Pogatshnik: Phys. Rev. B **42** (1990) 1410.

[75] A. Janotti and C. G. Van de Walle: Nat. Mater. **6** (2007) 44.

[76] K. Hayashi, S. Matsuishi, T. Kamiya, M. Hirano, and H. Hosono: Nature **419** (2002) 462.

[77] Y. Iwazaki, T. Suzuki, and S. Tsuneyuki: J. Appl. Phys. **108** (2010) 83705.

[78] Y. Kobayashi, O. J. Hernandez, T. Sakaguchi, T. Yajima, T. Roisnel, Y. Tsujimoto, M. Morita, Y. Noda, Y. Mogami, A. Kitada, M. Ohkura, S. Hosokawa, Z. Li, K. Hayashi, Y. Kusano, J. E. Kim, N. Tsuji, A. Fujiwara, Y. Matsushita, K. Yoshimura, K. Takegoshi, M. Inoue, M. Takano, and H. Kageyama: Nat. Mater. **11** (2012) 507.

[79] M.-H. Du and K. Biswas: Phys. Rev. Lett. **106** (2011) 115502.

[80] F. Filippone, G. Mattioli, P. Alippi, and A. A. Bonapasta: Phys. Rev. B **80** (2009) 245203.

[81] U. Diebold, S.-C. Li, and M. Schmid: Annual review of physical chemistry **61** (2010) 129.

[82] U. Aschauer, Y. He, H. Cheng, S.-C. Li, U. Diebold, and A. Selloni: J. Phys. Chem. C **114** (2010) 1278.

[83] M. Setví, U. Aschauer, P. Scheiber, Y.-F. Li, W. Hou, M. Schmid, A. Selloni, and U. Diebold: Science **341** (2013) 988.

[84] T. Sugimoto, K. Takeyasu, and K. Fukutani: J. Vac. Soc. Jpn. **56** (2013) 322.

[85] M. A. Henderson and S. A. Chambers: Surf. Sci. **449** (2000) 135.

[86] Y. Joseph, W. Ranke, and W. Weiss: J. Phys. Chem. B **4** (2000) 3224.

[87] B. B. Dayton: Trans. 8th Natl. Vac. Symp., 1961, p. 42.

[88] L. A. Dissado: Chem. Phys. Lett. **124** (1986) 206.

[89] K. Shimizu, R. Neuhauser, C. Leatherdale, S. Empedocles, W. Woo, and M. Bawendi: Phys. Rev. B **63** (2001) 205316.

[90] D. J. Huntley: J. Phys.: Condens. Matter **18** (2006) 1359.

[91] J. T. Bendler: J. Stat. Phys. **36** (1984) 625.

[92] R. Du, A. Y. Grosberg, and T. Tanaka: Phys. Rev. Lett. **84** (2000) 1828.

[93] M. Aouassa, L. Favre, A. Ronda, H. Maaref, and I. Berbezier: New J. Phys. **14** (2012) 063038.

[94] J. Rentrop, D. Schuricht, and V. Meden: New J. Phys. **14** (2012) 075001.

[95] G. Horikoshi: J. Vac. Sci. Technol. A **5** (1987) 2501.

[96] K. Kanazawa: J. Vac. Sci. Technol. A **7** (1989) 3361.

[97] M. P. Seah and W. A. Dench: Surf. Interface Anal. **1** (1979) 2.

[98] M. A. Van Hove, W. H. Weinberg, and C.-M. Chan: *Low-Energy Electron Diffraction: Experiment, Theory and Surface Structure Determination* (Springer-Verlag, Berlin, 1986).

[99] K. Fukutani, A. Itoh, M. Wilde, and M. Matsumoto: Phys. Rev. Lett. **88** (2002) 116101.

[100] T. E. Sharp: Atomic Data **169** (1971) 119.

[101] D. J. Kligler and C. K. Rhodes: Phys. Rev. Lett. **40** (1978) 309.

[102] L. Wolniewicz and K. Dressler: J. Chem. Phys. **82** (1985) 3292.

[103] L. Wolniewicz and K. Dressler: J. Chem. Phys. **88** (1988) 3861.

[104] K. Niki, M. Fujiwara, Y. Motoshima, T. Kawauchi, and K. Fukutani: Chem. Phys. Lett. **504** (2011) 136.

[105] W. M. Huo, K.-D. Rinnen, and R. N. Zare: J. Chem. Phys. **95** (1991) 205.

[106] K.-D. D. Rinnen, M. A. Buntine, D. a. V. Kliner, R. N. Zare, and W. M. Huo: J. Chem. Phys. **95** (1991) 214.

[107] *Atomic and Molecular Beam Methods volume 1*, ed. G. Scoles (Oxford University Press, Oxford, 1988).

[108] C. R. Arumainayagam and R. J. Madix: Prog. Surf. Sci. **38** (1991) 1.

[109] K. Teshima: Shinku **30** (1987) 5.

[110] Campargue: J. Phys. Chem. **88** (1984) 4466.

[111] D. M. Dennison: Proc. R. Soc. A **115** (1927) 483.

[112] T. L. Hill: *An Introduction to Statistical thermodynamics* (Dover Publications, New York, 1987) new ed.

[113] R. Moos and K. H. Härdtl: J. Am. Ceram. Soc. **80** (1997) 2549.

[114] A. Rothschild, W. Menesklou, H. L. Tuller, and E. I.-T.: Chem. Mater. **18** (2006) 3651.

[115] A. Fujimori, I. Hase, M. Nakamura, H. Namatame, Y. Fujishima, Y. Tokura, M. Abbate, F. M. F. de Groot, M. T. Czyzyk, and J. C. Fuggle: Phys. Rev. B **46** (1992) 9841.

[116] H. Yamada and G. R. Miller: J. Solid State Chem. **6** (1973) 169.

[117] J. F. Schooley, W. R. Hosler, E. Ambler, J. H. Becker, M. L. Cohen, and C. S. Koonce: Phys. Rev. Lett. **14** (1965) 305.

[118] Y. Kuo and K. J. Klabunde: Nanotechnology **23** (2012) 294001.

[119] S. Kawasaki, K. Akagi, K. Nakatsuji, S. Yamamoto, I. Matsuda, Y. Harada, J. Yoshinobu, F. Komori, R. Takahashi, M. Lippmaa, C. Sakai, H. Niwa, M. Oshima, K. Iwashina, and A. Kudo: J. Phys. Chem. C **116** (2012) 24445.

[120] A. F. Santander-Syro, O. Copie, T. Kondo, F. Fortuna, S. Pailhès, R. Weht, X. G. Qiu, F. Bertran, A. Nicolaou, A. Taleb-Ibrahimi, P. L. Fèvre, G. Herranz, M. Bibes, N. Reyren, Y. Apertet, P. Lecoeur, A. Barthélémy, and M. J. Rozenberg: Nature **469** (2011) 189.

[121] W. Meevasana, P. D. C. King, R. H. He, S.-K. Mo, M. Hashimoto, A. Tamai, P. Songsiriritthigul, F. Baumberger, and Z.-X. Shen: Nat. Mater. **10** (2011) 114.

[122] H. Ohta, Y. Sato, T. Kato, S. Kim, K. Nomura, Y. Ikuhara, and H. Hosono: Nat. commun. **1** (2010) 118.

[123] T. Yajima, Y. Yasuyuki, and H. Y. Hwang: Nat. Mater. **10** (2011) 198.

[124] T. Hikita, T. Hanada, and M. Kubo: Surf. Sci. **287/288** (1993) 377.

[125] V. E. Henrich: Prog. Surf. Sci. **9** (1979) 143.

[126] Y. Liang and D. A. Bonnell: Surf. Sci. **310** (1994) 128.

[127] T. Hikita, T. Hanada, and M. Kubo: J. Vac. Sci. Technol. A **11** (1993) 2649.

[128] M. R. Castell: Surf. Sci. **505** (2002) 1.

[129] T. Kubo and H. Nozoye: Phys. Rev. Lett. **86** (2001) 1801.

[130] T. Kubo and H. Nozoye: Surf. Sci. **542** (2003) 177.

[131] T. Kubo, H. Orita, and H. Nozoye: Phys. Chem. Chem. Phys. **13** (2011) 16516.

[132] T. Matsuda, Y. Yoshida, K. Mitsuhara, and Y. Kido: J. Chem. Phys. **138** (2013) 244705.

[133] K. Odaka and S. Ueda: Vacuum **47** (1996) 689.

[134] R. O. Adams: J. Vac. Sci. Technol. A **1** (1983) 12.

[135] R. P. Frankenthal and D. L. Maim: J. Electrochem. Soc. **123** (1976) 186.

[136] I. Olefjord, B. Brox, and U. Jelvestam: J. Electrochem. Soc. **132** (1985) 2854.

[137] G. Okamoto: Corr. Sci. **13** (1973) 471.

[138] K. Sugimoto and Y. Sawada: Corr. Sci. **17** (1977) 425.

[139] A. Rossi, B. Elsener, G. Hähner, M. Textor, and N. D. Spencer: Surf. Interface Anal. **29** (2000) 460.

[140] S. Azad, M. H. Engelhard, and L.-Q. Wang: J. Phys. Chem. B **109** (2005) 10327.

[141] J. Baniecki, M. Ishii, K. Kurihara, K. Yamanaka, T. Yano, K. Shinozaki, T. Imada, K. Nozaki, and N. Kin: Phys. Rev. B **78** (2008) 195415.

[142] J. E. T. Andersen and P. J. Moller: Thin Solid Films **186** (1990) 137.

[143] R. Shimizu, K. Iwaya, T. Ohsawa, S. Shiraki, T. Hasegawa, T. Hashizume, and T. Hitosugi: Appl. Phys. Lett. **100** (2012) 263106.

[144] V. E. Henrich, G. Dresselhaus, and H. J. Zeiger: Phys. Rev. B **17** (1978) 4908.

[145] V. E. Henrich and R. L. Kurtz: Phys. Rev. B **23** (1981) 6280.

[146] S. Ferrer and G. S. Somorjai: J. Appl. Phys. **52** (1981) 4792.

[147] D. A. Muller, N. Nakagawa, A. Ohtomo, J. L. Grazul, and H. Y. Hwang: Nature **430** (2004) 657.

[148] K. Iwaya, T. Ohsawa, R. Shimizu, T. Hashizume, and T. Hitosugi: Appl. Phys. Exp. **3** (2010) 075701.

[149] R. Ramsier and J. Yates: Surf. Sci. Rep. **12** (1991) 246.

[150] J. T. Yates, M. D. Alvey, M. J. Dresser, M. A. Henderson, M. Kiskinova, R. D. Ramsier, and A. Szabó: Science **255** (1992) 1397.

[151] C. M. Yim, C. L. Pang, and G. Thornton: Phys. Rev. Lett. **104** (2010) 36806.

[152] K. Takeyasu, K. Fukada, M. Matsumoto, and K. Fukutani: J. Phys.: Condens. Matter **25** (2013) 162202.

[153] J. L. M. van Mechelen, D. van der Marel, C. Grimaldi, A. B. Kuzmenko, N. P. Armitage, N. Reyren, H. Hagemann, and I. I. Mazin: Phys. Rev. Lett. **100** (2008) 226403.

[154] Y. Ishida, R. Eguchi, M. Matsunami, K. Horiba, M. Taguchi, and A. Chainani: Phys. Rev. Lett. **100** (2008) 56401.

[155] Q. Fu and T. Wagner: J. Phys. Chem. B **109** (2005) 11697.

[156] S. Wendt, P. T. Sprunger, E. Lira, G. K. H. Madsen, Z. Li, J. O. Hansen, J. Matthiesen, A. Blekinge-Rasmussen, E. Laegsgaard, B. r. Hammer, and F. Besenbacher: Science **320** (2008) 1755.

[157] M. A. Henderson, W. S. Epling, C. L. Perkins, and C. H. F. Peden: J. Phys. Chem. B **103** (1999) 5328.

[158] Y. Aiura, I. Hase, H. Bando, T. Yasue, T. Saitoh, and D. S. Dessau: Surf. Sci. **515** (2002) 61.

[159] F. G. Wakim: J. Chem. Phys. **49** (1968) 3738.

[160] B. Jalan, R. Engel-Herbert, T. E. Mates, and S. Stemmer: Appl. Phys. Lett. **93** (2008) 52907.

[161] J.-H. Ahn, P. C. McIntyre, L. W. Mirkarimi, S. R. Gilbert, J. Amano, and M. Schulberg: Appl. Phys. Lett. **77** (2000) 1378.

[162] Y. Iwazaki, Y. Gohda, and S. Tsuneyuki: APL Materials **2** (2014) 012103.

[163] F. T. Wagner, S. Ferrer, and G. A. Somorjai: Surf. Sci. **101** (1980) 462.

[164] K. Fukutani: Curr. Opin. Solid State Mater. Sci. **6** (2002) 153.

[165] J. F. Zieqler: *Handbook of stopping cross-sections for energetic ions in all elements* (Pergamon Press, New York, 1980).

[166] K. Takeyasu, K. Fukada, S. Ogura, M. Matsumoto, and K. Fukutani: J. Chem. Phys. **140** (2014) 084703.

[167] P. A. Thiel and T. E. Madey: Surf. Sci. Rep. **7** (1987) 211.

[168] J. Tao, Q. Cuan, X.-Q. Gong, and M. Batzill: J. Phys. Chem. C **116** (2012) 20438.

[169] E. Cho, S. Han, H.-S. Ahn, K.-R. Lee, S. Kim, and C. Hwang: Phys. Rev. B **73** (2006) 193202.

[170] R. Astala and P. D. Bristowe: Modelling Simul. Mater. Sci. Eng. **9** (2001) 415.

[171] R. C. Neville, B. Hoeneisen, and C. A. Mead: J. Appl. Phys. **43** (1972) 2124.

[172] D. R. Lide: *CRC handbook of chemistry and physics* (CRC Press, Boca Raton London New York Washington, D.C., 2001) 82nd ed.

[173] F. Lenzmann, J. Krueger, S. Burnside, K. Brooks, M. Gra, D. Gal, S. Ru, and D. Cahen: J. Phys. Chem. B **105** (2001) 6347.

[174] W. A. Harrison: *Electronic structure and the properties of solids* (Dover Publications, New York, 1989).

[175] P. P. Ewald: Ann. Phys. **64** (1921) 253.

[176] J. Prade, U. Schröder, W. Kress, F. W. de Wette, and A. D. Kulkarni: J. Phys.: Condens. Matter **5** (1993) 1.

[177] C. R. A. Catlow and B. E. F. Fender: J. Phys. C **8** (1975) 3267.

[178] R. D. Shannon and C. T. Prewitt: Acta. Cryst. **B25** (1969) 925.

[179] G. G. Libowitz and T. R. P. Gibb Jr.: J. Phys. Chem. **60** (1956) 510.

[180] K. Niki, S. Ogura, M. Matsumoto, T. Okano, and K. Fukutani: Phys. Rev. B **79** (2009) 085408.

[181] T. Sugimoto and K. Fukutani: Nat. Phys. **7** (2011) 307.

[182] N. Sanchez, S. Gallego, J. Cerdá, and M. C. Muñoz: Phys. Rev. B **81** (2010) 115301.

[183] F. H. Van Cauwelaert and W. K. Hall: Trans. Faraday Soc. **66** (1970) 454.

[184] F. H. Van Cauwelaert and W. K. Hall: J. Colloid and Interface Science **38** (1972) 138.

[185] R. J. Elsey: Vacuum **25** (1975) 299.

[186] R. J. Elsey: Vacuum **25** (1975) 347.

[187] P. A. Redhead: J. Vac. Sci. Technol. A **13** (1995) 467.

[188] K. Akaishi: J. Vac. Soc. Jpn. **42** (1999) 620.

[189] K. Akaishi, M. Nakasuga, and Y. Funato: J. Vac. Sci. Technol. A **19** (2001) 365.

[190] T. Ha, S. Chung, and M. Y. Choi: J. Phys.: Condens. Matter **21** (2009) 202101.

[191] W. Hackbusch: *Integral Equations: Theory and Numerical Treatment* (Birkhäuser Verlag, Basel ; Boston, 1995), Vol. B.

[192] K. Takeyasu, T. Sugimoto, and K. Fukutani: J. Phys. Soc. Jpn. **82** (2013) 114602.

[193] L. D. Landau and E. M. Lifshitz: *Statistical Physics* (Pergamon Press, Oxford, U.K., 1980) 3rd ed., Vol. B.

[194] J. I. Steinfeld, J. S. Francisco, and W. L. Hase: *Chemical Kinetics and Dynamics* (Prentice Hall, Englewood Cliffs, N.J., 1989).

[195] N. Bleistein and R. A. Handelsman: *Asymptotic Expansions of Integrals* (Dover Publications, New York, 2010) new ed.

[196] M. Li and H. F. Dylla: J. Vac. Sci. Technol. A **11** (1993) 1702.

[197] D. Hoffman, B. Singh, and J. H. Thomas, III: *Handbook of Vacuum Science and Technology* (Academic Press, San Diego, CA, 1998) 1st ed.

[198] M. Li and H. F. Dylla: J. Vac. Sci. Technol. A **12** (1994) 1772.

[199] D. Avnir, D. Farin, and P. Pfeifer: Nature **308** (1984) 261.

[200] D. Farin, A. Volpert, and D. Avnir: J. Am. Chem. Soc. **107** (1985) 3368.

[201] A. S. Foster and W. A. Hofer: *Scanning Probe Microscopy : Atomic Scale Engineering by Forces And Currents* (Springer, Berlin, 2006).

[202] H. Hochstadt: *Differential Equations: A Modern Approach* (Holt, Rinehart and Winston, New York, 1964).

[203] K. Takeyasu, T. Sugimoto, and K. Fukutani: J. Vac. Soc. Jpn. **56** (2013) 457.

[204] D. Costa, K. Sharkas, M. M. Islam, and P. Marcus: Surf. Sci. **603** (2009) 2484.

[205] R. A. Oriani: Acta Metallurgica **18** (1970) 147.

[206] L. Westerberg and B. Hjörvarsson: Vacuum **47** (1996) 687.

[207] M. W. Ruckman, M. Strongin, W. A. Lanford, and W. C. Turner: J. Vac. Sci. Technol. A **13** (1995) 1994.

[208] T. Yoshimura and Y. Ishikawa: J. Vac. Sci. Technol. A **20** (2002) 1450.

[209] K. Takeyasu, M. Matsumoto, and K. Fukutani: submitted to Vacuum (2014).

[210] Y. Fukai: *The metal-hydrogen system: Basic bulk properties* (Springer-Verlag, Berlin, 1993).

[211] Y. Ishikawa and V. Nemanič: Vacuum **69** (2003) 501.

[212] K. Akaishi, M. Nakasuga, and Y. Funato: J. Vac. Sci. Technol. A **20** (2002) 848.

[213] R. C. Baetzold and G. A. Somorjai: J. Catal. **105** (1976) 94.

[214] Y. Tuzi, T. Tanaka, K. Takeuchi, and Y. Saito: Vacuum **47** (1996) 705.